GLOBAL AND LOCAL CONTRIBUTORS TO THE HISTORICAL AND PROJECTED REGIONAL CLIMATE CHANGE ON THE NORTH SLOPE OF ALASKA

By

Lei Cai, B.S., M.S.

A Dissertation Submitted in Partial Fulfillment of the Requirements

for the Degree of

Doctor of Philosophy

in

Atmospheric Sciences

University of Alaska Fairbanks

May 2018

APPROVED:
Vladimir A. Alexeev, Committee Chair
Christopher D. Arp, Committee Member
Uma S. Bhatt, Committee Member
Anna K. Liljedahl, Committee Member
Uma S. Bhatt, Chair
Department of Atmospheric Sciences
Anupma Prakash, Interim Dean
College of Natural Science & Mathematics
Michael Castellini, *Dean of the Graduate School*

Abstract

This thesis includes four studies that explore and compare the impacts of four contributing factors resulting in regional climate change on the North Slope of Alaska based on a numerical simulation approach. These four contributing factors include global warming due to changes in radiative forcing, sea ice decline, earlier Arctic lake ice-off, and atmospheric circulation change over the Arctic.

A set of dynamically downscaled regional climate products has been developed for the North Slope of Alaska over the period from 1950 up to 2100. A fine grid spacing (10 km) is employed to develop products that resolve detailed mesoscale features in the temperature and precipitation fields on the North Slope of Alaska. Processes resolved include the effects of topography on regional climate and extreme precipitation events. The Representative Concentration Pathway (RCP) 4.5 scenario projects lower rates of precipitation and temperature increase than RCP8.5 compared to the historical product. The increases of precipitation and temperature trends in the RCP8.5 projection are higher in fall and winter compared to the historical product and the RCP4.5 projection.

The impacts of sea ice decline are addressed by conducting sensitivity experiments employing both an atmospheric model and a permafrost model. The sea ice decline impacts are most pronounced in late fall and early winter. The near surface atmospheric warming in late spring and early summer due to sea ice decline are projected to be stronger in the 21st century. Such a warming effect also reduces the total cloud cover on the North Slope of Alaska in summer by destabilizing the atmospheric boundary layer. The sea ice decline warms the atmosphere and the permafrost on the North Slope of Alaska less strongly than the global warming does, while it primarily results in higher seasonal variability of the positive temperature trend that is bigger in late fall and early winter than in other seasons.

The ongoing and projected earlier melt of the Arctic lake ice also contributes to regional climate change on the Northern coast of Alaska, though only on a local and seasonal scale. Heat and moisture released from the opened lake surface primarily propagate downwind of the lakes. The impacts of the earlier lake ice-off on both the atmosphere and the permafrost underneath are comparable to those of the sea ice decline in late spring and early summer, while they are roughly six times weaker than those of sea ice decline in late fall and early winter. The permafrost warming resulted from the earlier lake ice-off is speculated to be stronger with more snowfall expected in the 21st century, while the overall atmospheric warming of global origin is speculated to continue growing.

Two major Arctic summer-time climatic variability patterns, the Arctic Oscillation (AO) and the Arctic Dipole (AD), are evaluated in 12 global climate models in Coupled Model Intercomparison Program Phase 5 (CMIP5). A combined metric ranking approach ranks the models by the Pattern Correlation Coefficients (PCCs) and explained variances calculated from the model-produced summer AO and AD over the historical period. Higher-ranked models more consistently project a positive trend of the summer AO index and a negative trend of summer AD index in their RCP8.5 projections. Such long-term trends of large-scale climate patterns will inhibit the increase in air temperature while favoring the increase in precipitation on the North Slope of Alaska.

In summary, this thesis bridges the gaps by quantifying the relative importance of multiple contributing factors to the regional climate change on the North Slope of Alaska. Global warming is the leading contributing factor, while other factors primarily contribute to the spatial and temporal asymmetries of the regional climate change. The results of this thesis lead to a better understanding of the physical mechanisms behind the climatic impacts to the hydrological and ecological changes of the North Slope of Alaska that have been become more severe and more frequent. They, together with the developed downscaling data products, serve as the climatic background information in such fields of study.

Table of Contents

List of Figures

List of Tables

Acknowledgements

I want to start by thanking my adviser, Vladimir Alexeev, for offering me the chance to pursue my Ph. D at the University of Alaska Fairbanks (UAF), for his effort in this three years helping me conduct climatic research, and for his guidance on the pathway from a student to a scholar. I thank my committee members: Christopher D. Arp, Uma S. Bhatt, and Anna K. Liljedahl for their collaborations, guidance, and helps throughout my time of being a Ph. D student at UAF.

I would like to thank my coauthors and collaborators of the four papers included in the thesis. They are Benjamin Jones, Anne Gädeke, and John Walsh. Those papers would not be possible without the generous helps in both the science part and the writing part. My Ph. D studies are tightly based on the numerical modeling approach. Special thanks are given to Andrew Monaghan, for his help technically on converting CESM output files into WRF intermediate format, from which I have been benefitted since my Master's study at the University of Kansas. Frank Urban has helped me a lot in retrieving and interpreting the permafrost temperature data. Staff members at Arctic Region Supercomputing Center (ARSC) and later the Research Computing Systems (RCS) are very helpful with a great patience to resolve all my technical difficulties I encountered during the numerical modeling processes.

Faculties and staffs in the Department of Atmospheric Sciences and the International Arctic Research Center have offered generous help, shared valuable ideas, and had great conversations. I owe my thanks to Matt Barkdull, Nate Bauer, Peter Bieniek, Richard Collins, Javier Fochesatto, Nicole Mölders, Bill Simpson, Craig Stephenson, and Xiangdong Zhang. I specifically want to thank Barbara Day for her help and advice through my applications twice, respectively in 2011 and 2014. As a Ph. D student here, she has been helping a lot on preparing all the paperwork on every one of my steps approaching the degree. It has been a great time studying and living here in Fairbanks. I thank many students and alumni in the Department of Atmospheric Sciences for the great communications, helps, and friendship. Specifically, they are Till Baumann, Stanley Edwin, Abraham Endalamaw, Rick Lader, Jintai Li, Liran Peng, and Yang Yang.

The studies during my Ph. D is funded by the National Science Foundation (NSF) National Science Foundation ARC-1107481 and ARC-1417300, as well as the Global Change Student Research Grant offered by Cooperative Institute for Alaska Research (CIFAR). I thank Mingchu

Zhang from the School of Natural Resources and Extension, as well as the International Arctic Research Center for the support financially in the last semester of my Ph. D study when out of funding support. I also thank Dmitry Nicolsky for offering me a temporary job next semester to help me get through the crunch time between the defense and the graduation.

Finally, I want to thank my parents and my family for their support and consideration in my 6-year journey of studying abroad. I especially owe my thanks to my wife, Yu Lian. This thesis is impossible if without her great sacrifice that bringing our first daughter, Silvia, to this world and taking care of her all by herself for as long as 18 months and counting.

Chapter 1 Introduction

1.1 Climatic background on the North Slope of Alaska

The North Slope of Alaska includes the Arctic Coastal Plain and part of the Northern Brooks Range foothill area, as the northernmost part of Alaska on the Arctic coast. Among all the climate divisions of Alaska (Bieniek et al., 2012), the North Slope of Alaska is the coldest one with the least precipitation, in which the annual mean temperature ranges from -20 °C to -12 °C while the annual precipitation amount is about 200 mm (Zhang et al., 1996; Stafford et al., 2000). In such a cold environment with a short growing season, the Arctic tundra is the dominant vegetation type on the North Slope of Alaska, underneath which lies the continuous permafrost with a 30-50 cm depth of active layer (Nelson et al., 1997). The seasonal sea ice extent variation off the coast significantly influences the regional climate on the North Slope of Alaska (Wendler et al., 2009). Typically in late March and early April, sea ice covers most of the Arctic Ocean and along the Northern and Western Coast of Alaska. In September however, a large oceanic area in the Beaufort and the Chukchi Seas, not to mention the Bering Strait, has no sea ice cover. Such seasonal variations of sea ice extent makes the North Slope of Alaska dominated by a maritime type climate in summer while by a continental type climate in winter (Hartman and Johnson, 1984).

There are several atmospheric circulation patterns affecting the regional climate on the North Slope of Alaska, directly or indirectly by affecting the sea ice extent. The Arctic Oscillation (AO), or the Northern Annular Mode (NAM), is the dominant mode of atmospheric circulation defined by applying Empirical Orthogonal Function (EOF) analysis on the Sea Level Pressure (SLP) anomaly (Thompson and Wallace, 1998; Wu et al., 2006). The AO is presented as an annular-shaped pattern over the central Arctic, which can also be interpreted as signature of the polar vortex strength at the surface (Thompson and Wallace, 1998). Other than modulating the strength of the jet stream over the mid-latitudes (Deser, 2000), the AO is also an indicator of the zonal sea ice motion in the Arctic Ocean that the cyclonic/anticyclonic anomalous wind drives the sea ice divergence/convergence (Wu et al., 2006). The second most important mode, called the Arctic Dipole (AD), on the other hand, plays a bigger role in the meridional motion of sea ice. The AD can be seen in the second EOF mode of the SLP anomaly poleward of 60°N as a dipole-shaped pattern that has a positive/negative anomaly center over the North America and a negative/positive anomaly center over the Eurasia in its positive/negative phase. The summer AD index has maintained its positive phase since the early 2000s shown from the reanalysis data, which results in the anomalous meridional transpolar wind pattern from the Chukchi Sea to the Greenland Sea, driving the sea ice export through Fram Strait and opening a larger water body offshore the Northern coast of Alaska (Watanabe et al., 2006; Wu et al., 2006; Alexeev et al., 2015). Moreover, the positive AD also favors the sea ice melt in summer by enhancing the oceanic heat advection through the Bering Strait into the Arctic Ocean (Kay et al., 2008; Wang et al., 2009; Kapsch et al., 2013). The positive anomaly center for the summer AD can be a reflection of a stronger, northward-shifted Beaufort Sea High (BSH), enhancing the southerly wind and bringing higher temperature and less precipitation to the North Slope of Alaska (Serreze and Barrett, 2011). The increase of the AD index since the early 2000s could be a consequence of multi-decadal scale present in AD spectrum, but the physical mechanism of AD remains unclear based on the current knowledge. Studying the mechanisms and impacts of AD is beneficial for better understanding the sea ice retreat and the climate change over the whole Arctic in the 21st century.

The Arctic lakes cover more than 70% of the land surface of the Arctic Coastal Plain of Alaska, causing the well known surface albedo decrease when their ice cover melts in summer (Hinkel et al., 2003). Most of the lakes are shallow (lake depth <10 m), and ice-covered for 60%-80% time in a year (Arp et al., 2011). Depending on their lake depths and the maximum ice thicknesses (typically around 2 meters) in winter, these lakes are categorized as the bedfast ice lakes in which the water is frozen to the bottom, and the floating ice lakes in which the ice cover floats above a thaw bulb or talik (Arp et al., 2015). Scientists believe that these lakes came into existence in the early Holocene when the earth's atmosphere was warmer than today (Ritchie et al., 1983; Hopkins and Kidd 1988; Côté and Burn 2002). The formation and drainage of Arctic lakes back then was associated with a deeper active layer and the thermokarst formation in the ice-rich permafrost, resembling what has been recently observed since the 1970s (Burn 1997). Lakes are a dominant landscape type on the North Slope of Alaska and they play an important role in transforming the environment as land cover changes from frozen to melted surfaces, therefore Arctic lakes are worth paying more attention to for their role in the regional climate.

1.2 Vulnerability of the North Slope of Alaska to climate change

Since the 1970s, the North Slope of Alaska has been warming unlike all other parts of the earth. A 2.9 °C annual mean temperature increase has been observed at Barrow in 1972-2007, together with higher wind speed and storm frequency (Wendler et al., 2009). The temperature in Barrow increases more than 300% faster than the global mean temperature does (0.7 °C, from 1972 to 2007, according to IPCC AR4 report). Such pronounced amplified warming has been observed not only on the North Slope of Alaska but also across the high-latitudes, and is called polar amplification. Early studies attribute the cause of polar amplification primarily to the Surface Albedo Feedback (SAF), where a reduced surface albedo from the sea ice decline absorbs more energy, resulting in stronger sea ice decline (Manabe and Stouffer, 1980), although the role of SAF as its leading contributor of the polar amplification has been questioned in a number of studies (e.g., Winton, 2006). Other factors that are likely to cause polar amplification include, but are not limited to, low-frequency climate variabilities, such as the AO and the Pacific Decadal Oscillation (PDO) (Serreze and Francis, 2006), the enhanced meridional heat transport from the low-latitudes (Alexeev et al., 2005), and changes in atmospheric and oceanic heat flux convergence (Yang et al., 2010).

Permafrost underneath the North Slope of Alaska has also been warming. Borehole temperature measurements have recorded a 1 °C permafrost temperature increase on average within 0-15 m depth in the period of 1950-2001 at Barrow, while the active layer (8 cm) temperature rises more than 1 °C (Romanovsky et al., 2002). Such permafrost warming can result in the deepening of permafrost active layer (Zhang et al., 1997), permafrost degradation (Jorgenson et al., 2006), and various hydrological and ecological impacts (Kane et al., 1991; Smith et al., 2005; Post et al., 2009).

The Arctic sea ice has been declining since the 1970s (data from National Snow and Ice Data Center, https://nsidc.org/arcticseaicenews/charctic-interactive-sea-ice-graph/). The sea ice extent is declining by over 4% per decade in September on average (Cavalieri and Parkinson, 2012). The record-breaking sea ice minimum occurred in the September of 2012 that the sea ice area shrunk to as small as 2.4×10^7 km^2. The sea ice cover is also declining in other months, only in lower rates than that in September (Serreze et al., 2007). The opened oceanic water body releases heat and moisture to the low atmosphere and enhances the turbulent heat fluxes, which are maximized in strength in late fall and early winter when the near-surface atmosphere is substantially colder than the opened water surface (Rinke et al., 2006; Francis et al., 2009). The abundance of heat and moisture also favors the cloud formation and precipitation over the North Slope of Alaska (Curtis et al., 1998; Schweiger et al., 2008).

The sea ice decline is associated with or facilitated by the atmospheric circulation change over the high-latitudes. Zhang et al. (2008) discovered that a tri-polar AO/NAO pattern was systematically shifted to a dipole pattern in 2005-2007 in the first EOF mode of monthly SLP anomaly in a 36-months running time window (Running-EOF/PC). In the time windows from 2002 to 2006, a negative anomaly was centered over Northern Eurasia, while a positive anomaly was centered over the Northern Pacific also expanding into the Beaufort Sea (Zhang et al., 2008). Moore (2012) who studied the decadal variation of the BSH, found that a strengthening BSH was moving in North-East direction during 1948-2011. These shifts in the atmospheric circulation and the enhanced BSH echo impacted the summer AD that stayed in a highly positive phase since 2000 (Wu et al., 2012; Alexeev et al., 2015). Both studies concluded that the meridional anomalous wind from East Siberian and Chukchi Seas towards Greenland Sea has been strengthening. Such wind anomaly pattern drives sea ice export from Fram Strait and pushes sea ice away from Alaskan and Siberian coasts, thus opening a larger oceanic water body near Siberia and the North Slope of Alaska.

Field campaigns have observed that the Arctic lake ice cover is becoming thinner and is melting earlier in summer (Zhang and Jeffries, 2000). On the North Slope of Alaska, the observed start and end dates of lake ice melt keep moving 0.6 and 0.34 days earlier each year, respectively (Šmejkalová et al., 2016). Model results show that lakes are influenced more by the warming climate than land along the pan-Arctic coast, projecting up to 2 months longer duration of the ice-free period and 60 cm thinner maximum lake ice thickness across the North American Arctic by the end of the 21st century (Brown and Duguay, 2011). Projected warming temperatures and increasing precipitation (snowfall) due to the sea ice decline can also inhibit the lake ice growth in early winter, potentially leading to an earlier melt the following summer (Alexeev et al., 2016). The decrease of maximum lake ice thickness will transform some bedfast ice lakes into floating ice lakes on the North Slope of Alaska (Arp et al., 2015) with some important consequences for the environment, including changes in surface energy budgets, hydrology and aquatic habitats. The earlier opening of water on the lakes on the North Slope of Alaska is likely to result in more heat and moisture released into the near-surface atmosphere, potentially changing the regional climate of the North Slope of Alaska.

1.3 Merits of the numerical modeling approach

The knowledge gaps of climate mechanisms in the Arctic in general partially originate from insufficient climate observations, in particular on the North Slope of Alaska both spatially and temporally. The observation of climatic variables on the North Slope of Alaska has been severely restricted by the sparsely distributed facilities, some of which are only operational seasonally (Shulski and Wendler, 2007). The accuracy of observations is also difficult to guarantee due to the specifics of the environment (e.g. strong winds), especially for the solid precipitation that is typically underestimated by at least a factor of two (Groisman et al., 1991; Rasmussen et al., 2012; Liljedahl et al., 2017). Lack of data is one of the big limiting factors for studying climate change in the high latitudes and new approaches to develop needed datasets.

Dynamical downscaling is a model-based approach to produce high resolution gridded climatic variables by employing Regional Climate Models (RCMs) driven by other, coarser resolution datasets, originating from for example, the Global Climate Models (GCMs) or reanalysis datasets. For Alaska, a dynamical downscaling dataset forced by ERA-interim reanalysis data has been developed with a 20 km grid spacing using the Weather Research and Forecast (WRF) model (Bieniek et al., 2016). Chukchi–Beaufort High-resolution Atmospheric Reanalysis (CBHAR) is another WRF-based downscaling product that focuses primarily in the Beaufort and the Chukchi Seas, as well as in the Arctic Alaska (Liu et al., 2014; Zhang et al., 2016). These dynamical downscaling products both involved certain data assimilation approaches during the modeling process, primarily serving as the high-resolution alternative of the climate background. Their mesoscale framework also enables them to recapture the climatic extremes over the remote regions in Alaska with no observational data available (Lader et al., 2017). As mentioned, multiple contributing factors are interactively driving the regional climate change on the North Slope of Alaska. Designing sensitivity experiments using numerical simulations is one way to isolate the climate change impacts from each one of the factors. Strey et al. (2010) and Porter et al. (2012) have designed such sensitivity experiments using WRF to explore the impacts of the sea ice retreat in the summer of 2007 to the low atmosphere across the pan-Arctic. This study will utilize a similar approach applied to a smaller domain to focus on the impacts of the declining sea ice on physical environment of the North Slope of Alaska.

1.4 Research questions, objectives, and approaches

This thesis is aimed to explore and compare the relative contributions from multiple contributing factors to the regional climate change on the North Slope of Alaska, as well as their evolution under a warming climate in the 21st century. We present the following research questions:

1. How do global warming, sea ice decline, earlier lake ice-off, and atmospheric circulation changes result in the regional climate change on the North Slope of Alaska respectively?
2. What is the relative importance of each contributing factor to the regional climate change on the North Slope of Alaska?
3. How do the impacts of those contributing factors change with the warming climate?

To address the above research questions, we set up the following research objectives:

1. Develop a set of high-resolution data products by dynamically downscaling ERA-interim reanalysis dataset and multiple Community Earth System Model (CESM) products using the WRF model with Arctic modeling optimizations.
2. Explore how sea ice decline and the earlier lake ice-off impact the lower-atmosphere over the North Slope of Alaska.
3. Explore how the sea ice decline and the earlier lake ice-off impact the permafrost temperature regimes over the North Slope of Alaska.
4. Examine the summer-time atmospheric circulation patterns in present-day climate and in future climate projections, and how it leads to temperature and precipitation anomalies across the pan-Arctic coastal area, especially the North Slope of Alaska.

Firstly, we develop a high-resolution dataset through the dynamical downscaling approach using the WRF model with a polar modeling optimization (Polar WRF). Among all the model-based dataset with a focus on the Arctic Alaska, this set of dynamical downscaling products has the highest spatial (10 km) resolution, the longest temporal coverage (1950-2100), and multiple radiative forcing scenarios for projecting the 21st-century climate. No data assimilation or spectral nudging is applied during the modeling process, in order to preserve as much model dynamics and correlations between variables as possible. On the contrary, we deployed a linear scaling bias-correction to control the biases in major climatic variables. This dataset portrays the overall regional climate change on the North Slope of Alaska as the first part of the thesis, and a high-resolution alternative to the reanalysis datasets and global climate model products.

The contributing factors of the sea ice decline and the earlier lake ice-off to the lower atmosphere are explored by conducting WRF sensitivity experiments, which are designed by prescribing the sea ice/lake ice cover in WRF surface boundary condition while keeping the lateral (atmospheric) boundary condition unchanged. Key variables representing the atmospheric conditions, as well as the surface radiation budgets, are compared from the sensitivity case to the control case, to quantify the isolated contributions from the prescribed surface (sea ice cover or lake ice cover) changes. Specifically for the lake ice-off impacts study, we run WRF in an extremely high spatial resolution and complex physics parameterizations as they are required to involve a substantial number of Arctic lakes, at the cost of the heavy-loaded computations. Moreover, WRF's land surface parameterization scheme resolves only 1-meter depth of soil, which is insufficient to retrieve a reasonable permafrost thermal dynamics. The Geophysical Institute Permafrost Laboratory (GIPL) permafrost model is alternatively employed to explore the sensitivity of the permafrost temperature regimes, forced by the surface air temperatures prescribed under different sea ice/lake ice conditions.

Summer-time atmospheric circulation changes in Arctic are evaluated in 12 global climate models from the Coupled Model Intercomparison Project Phase 5 (CMIP5). A combined metric ranking approach quantitatively compares the performances of the models on retrieving the AO and the AD in summer in their historical simulations. The evolutions of the summer AO and AD in the 21st century, as well as their climatic impacts, are compared between the 12 models, for any dependences of their performances in the historical period, and for any agreement of atmospheric circulation changes in summer in the 21st century.

The thesis is organized as follows. Chapter 2 introduces the development of the dynamical downscaling products, as well as portraying the overall precipitation and temperature projections on the North Slope of Alaska by the end of the 21st century. Chapter 3 discusses the model sensitivity study explores the responses of low atmosphere and permafrost over the underneath the

North Slope of Alaska to the projected sea ice decline. The study in Chapter 4 is also empowered by WRF and GIPL, but with an extremely fine spatial resolution, to resolve major Arctic lakes on the North Slope of Alaska and to explore what their earlier ice-off brings to the low atmosphere and permafrost. Chapter 5 introduces the evaluations of summer atmospheric circulation patterns, impacts, and projections in 12 CMIP5 models. Chapter 6 contains the diagnostic discussion on the combined effects of contributing factors, the general conclusions, and the future works.

References

Alexeev, V. A., P. L. Langen, and J. R. Bates, 2005: Polar amplification of surface warming on an aquaplanet in "ghost forcing" experiments without sea ice feedbacks. *Climate Dynamics,* **24**, 655-666.

Alexeev, V. A., E. S. Euskirchen, J. E. Cherry, and R. C. Busey, 2015: Tundra burning in 2007–Did sea ice retreat matter? *Polar Science*, **9,** 185-195.

Alexeev, V. A., C. D. Arp, B. M. Jones, and L. Cai, 2016: Arctic sea ice decline contributes to thinning lake ice trend in northern Alaska. *Environmental Research Letters*, **11,** 074022.

Alexeev, V. A., J. E. Walsh, V. V. Ivanov, V. A. Semenov, and A. V. Smirnov, 2017: Warming in the Nordic Seas, North Atlantic storms and thinning Arctic sea ice. *Environmental Research Letters*, **12**.

Arp, C. D., B. M. Jones, F. E. Urban, and G. Grosse, 2011: Hydrogeomorphic processes of thermokarst lakes with grounded-ice and floating-ice regimes on the Arctic coastal plain, Alaska. *Hydrological Processes*, **25,** 2422-2438.

Arp, C. D., B. M. Jones, A. K. Liljedahl, K. M. Hinkel, and J. A. Welker, 2015: Depth, ice thickness, and ice-out timing cause divergent hydrologic responses among Arctic lakes. *Water Resources Research,* **51,** 9379-9401.

Bieniek, P. A., U. S. Bhatt, J. E. Walsh, T. S. Rupp, J. Zhang, J. R. Krieger, and R. Lader, 2016: Dynamical Downscaling of ERA-Interim Temperature and Precipitation for Alaska. *Journal of Applied Meteorology and Climatology*, **55,** 635-654.

Bieniek, P. A., and Coauthors, 2012: Climate Divisions for Alaska Based on Objective Methods. *Journal of Applied Meteorology and Climatology*, **51,** 1276-1289.

Brown, L., and C. Duguay, 2011: The fate of lake ice in the North American Arctic. *Cryosphere*, **5,** 869-892.

Burn, C., 1997: Cryostratigraphy, paleogeography, and climate change during the early Holocene warm interval, western Arctic coast, Canada. *Canadian Journal of Earth Sciences*, **34,** 912-925.

Côté, M., and C. Burn, 2002: The oriented lakes of Tuktoyaktuk Peninsula, Western Arctic Coast, Canada: a GIS-based analysis. *Permafrost and Periglacial Processes*, **13,** 61-70.

Cavalieri, D., and C. Parkinson, 2012: Arctic sea ice variability and trends, 1979-2010. *The Cryosphere*, **6,** 881.

Curtis, J., G. Wendler, R. Stone, and E. Dutton, 1998: Precipitation decrease in the western Arctic, with special emphasis on Barrow and Barter Island, Alaska. *international Journal of Climatology*, **18,** 1687-1707.

Deser, C., 2000: On the teleconnectivity of the "Arctic Oscillation". *Geophysical Research Letters*, **27,** 779-782.

Francis, J. A., W. Chan, D. J. Leathers, J. R. Miller, and D. E. Veron, 2009: Winter Northern Hemisphere weather patterns remember summer Arctic sea-ice extent. *Geophysical Research Letters*, **36**.

Groisman, P. Y., V. Koknaeva, T. Belokrylova, and T. Karl, 1991: Overcoming biases of precipitation measurement: A history of the USSR experience. *Bulletin of the American Meteorological Society*, **72,** 1725-1733.

Hartman, C. W., and P. R. Johnson, 1984: Environmental atlas of Alaska.

Hinkel, K. M., W. R. Eisner, J. G. Bockheim, F. E. Nelson, K. M. Peterson, and X. Dai, 2003: Spatial extent, age, and carbon stocks in drained thaw lake basins on the Barrow Peninsula, Alaska. *Arctic, Antarctic, and Alpine Research*, **35,** 291-300.

Hopkins, D., and J. Kidd, 1988: Thaw lake sediments and sedimentary environments. *Proceedings of the 5th International Permafrost Conference*, 790-795.

Jorgenson, M. T., Y. L. Shur, and E. R. Pullman, 2006: Abrupt increase in permafrost degradation in Arctic Alaska. *Geophysical Research Letters*, **33**.

Kane, D. L., L. D. Hinzman, and J. P. Zarling, 1991: Thermal response of the active layer to climatic warming in a permafrost environment. *Cold Regions Science and Technology*, **19,** 111-122.

Kapsch, M.-L., R. G. Graversen, and M. Tjernström, 2013: Springtime atmospheric energy transport and the control of Arctic summer sea-ice extent. *Nature Climate Change*, **3,** 744-748.

Kay, J. E., T. L'Ecuyer, A. Gettelman, G. Stephens, and C. O'Dell, 2008: The contribution of cloud and radiation anomalies to the 2007 Arctic sea ice extent minimum. *Geophysical Research Letters*, **35**.

Lader, R., J. E. Walsh, U. S. Bhatt, and P. A. Bieniek, 2017: Projections of Twenty-First-Century Climate Extremes for Alaska via Dynamical Downscaling and Quantile Mapping. *Journal of Applied Meteorology and Climatology*, **56,** 2393-2409.

Liljedahl, A. K., L. D. Hinzman, D. L. Kane, W. C. Oechel, C. E. Tweedie, and D. Zona, 2017: Tundra water budget and implications of precipitation underestimation. Water Resources Research, 53.

Liu, F., J. R. Krieger, and J. Zhang, 2014: Toward producing the Chukchi–Beaufort High-Resolution Atmospheric Reanalysis (CBHAR) via the WRFDA data assimilation system. *Monthly Weather Review*, **142,** 788-805.

Manabe, S., and R. J. Stouffer, 1980: Sensitivity of a global climate model to an increase of CO2 concentration in the atmosphere. *Journal of Geophysical Research: Oceans*, **85,** 5529-5554.

Moore, G., 2012: Decadal variability and a recent amplification of the summer Beaufort Sea High. *Geophysical Research Letters*, **39**.

Nelson, F., N. Shiklomanov, G. Mueller, K. Hinkel, D. Walker, and J. Bockheim, 1997: Estimating active-layer thickness over a large region: Kuparuk River basin, Alaska, USA. *Arctic and Alpine Research***,** 367-378.

Porter, D. F., J. J. Cassano, and M. C. Serreze, 2012: Local and large-scale atmospheric responses to reduced Arctic sea ice and ocean warming in the WRF model. *Journal of Geophysical Research*, **117**.

Post, E., and Coauthors, 2009: Ecological dynamics across the Arctic associated with recent climate change. *Science*, **325,** 1355-1358.

Rasmussen, R., and Coauthors, 2012: How well are we measuring snow: The NOAA/FAA/NCAR winter precipitation test bed. *Bulletin of the American Meteorological Society*, **93,** 811-829.

Rinke, A., W. Maslowski, K. Dethloff, and J. Clement, 2006: Influence of sea ice on the atmosphere: A study with an Arctic atmospheric regional climate model. *Journal of Geophysical Research: Atmospheres*, **111**.

Ritchie, J. C., L. C. Cwynar, and R. Spear, 1983: Evidence from north-west Canada for an early Holocene Milankovitch thermal maximum. *Nature*, **305,** 126-128.

Romanovsky, V., M. Burgess, S. Smith, K. Yoshikawa, and J. Brown, 2002: Permafrost temperature records: indicators of climate change. *EOS, Transactions American Geophysical Union*, **83,** 589-594.

Schweiger, A. J., R. W. Lindsay, S. Vavrus, and J. A. Francis, 2008: Relationships between Arctic sea ice and clouds during autumn. *Journal of Climate*, **21,** 4799-4810.

Serreze, M. C., and J. A. Francis, 2006: The Arctic Amplification Debate. *Climatic Change*, **76,** 241-264.

Serreze, M. C., and A. P. Barrett, 2011: Characteristics of the Beaufort Sea high. *Journal of Climate*, **24,** 159-182.

Serreze, M. C., M. M. Holland, and J. Stroeve, 2007: Perspectives on the Arctic's shrinking sea-ice cover. *science*, **315,** 1533-1536.

Shulski, M., and G. Wendler, 2007: *The climate of Alaska.* University of Alaska Press.

Šmejkalová, T., M. E. Edwards, and J. Dash, 2016: Arctic lakes show strong decadal trend in earlier spring ice-out. *Scientific Reports*, **6**.

Smith, L. C., Y. Sheng, G. MacDonald, and L. Hinzman, 2005: Disappearing arctic lakes. *Science*, **308,** 1429-1429.

Stafford, J., G. Wendler, and J. Curtis, 2000: Temperature and precipitation of Alaska: 50 year trend analysis. *Theoretical and Applied Climatology*, **67,** 33-44.

Strey, S. T., W. L. Chapman, and J. E. Walsh, 2010: The 2007 sea ice minimum: Impacts on the Northern Hemisphere atmosphere in late autumn and early winter. *Journal of Geophysical Research: Atmospheres*, **115**.

Thompson, D. W., and J. M. Wallace, 1998: The Arctic Oscillation signature in the wintertime geopotential height and temperature fields. *Geophysical research letters*, **25,** 1297-1300.

Wang, J., and Coauthors, 2009: Is the Dipole Anomaly a major driver to record lows in Arctic summer sea ice extent? *Geophysical Research Letters*, **36**.

Watanabe, E., J. Wang, A. Sumi, and H. Hasumi, 2006: Arctic dipole anomaly and its contribution to sea ice export from the Arctic Ocean in the 20th century. *Geophysical research letters*, **33**.

Wendler, G., M. Shulski, and B. Moore, 2009: Changes in the climate of the Alaskan North Slope and the ice concentration of the adjacent Beaufort Sea. *Theoretical and Applied Climatology*, **99,** 67-74.

Winton, M., 2006: Amplified Arctic climate change: What does surface albedo feedback have to do with it? *Geophysical Research Letters*, **33**.

Wu, B., J. Wang, and J. E. Walsh, 2006: Dipole anomaly in the winter Arctic atmosphere and its association with sea ice motion. *Journal of Climate*, **19,** 210-225.

Wu, B., J. E. Overland, and R. D'Arrigo, 2012: Anomalous Arctic surface wind patterns and their impacts on September sea ice minima and trend. *Tellus A*, **64**.

Yang, X. Y., J. C. Fyfe, and G. M. Flato, 2010: The role of poleward energy transport in Arctic temperature evolution. *Geophysical Research Letters*, **37**.

Zhang, J., F. Liu, W. Tao, J. Krieger, M. Shulski, and X. Zhang, 2016: Mesoscale Climatology and Variation of Surface Winds over the Chukchi–Beaufort Coastal Areas. *Journal of Climate*, **29,** 2721-2739.

Zhang, T., and M. Jeffries, 2000: Modeling interdecadal variations of lake-ice thickness and sensitivity to climatic change in northernmost Alaska. *Annals of Glaciology*, **31,** 339-347.

Zhang, T., T. Osterkamp, and K. Stamnes, 1996: Some characteristics of the climate in northern Alaska, USA. *Arctic and Alpine Research***,** 509-518.

——, 1997: Effects of climate on the active layer and permafrost on the North Slope of Alaska, USA. *Permafrost and Periglacial Processes*, **8,** 45-67.

Zhang, X., A. Sorteberg, J. Zhang, R. Gerdes, and J. C. Comiso, 2008: Recent radical shifts of atmospheric circulations and rapid changes in Arctic climate system. *Geophysical Research Letters*, **35**.

Chapter 2 The polar WRF downscaled historical and projected 21st-century climate for the coast and foothills of Arctic Alaska[1]

Abstract

Climate change is most pronounced in the northern high latitude region. Yet, climate observations are unable to fully capture regional-scale dynamics due to the sparse weather station coverage, which limits our ability to make reliable climate-based assessments. A set of simulated data products was therefore developed for the North Slope of Alaska through a dynamical downscaling approach. The polar-optimized Weather Research & Forecast (Polar WRF) model was forced by three sources: The ERA-interim reanalysis data (for 1979-2014), the Community Earth System Model 1.0 (CESM1.0) historical simulation (for 1950-2005), and the CESM1.0 projected (for 2006-2100) simulations in two Representative Concentration Pathways (RCP4.5 and RCP8.5) scenarios. Climatic variables were produced in a 10-km grid spacing and a 3-hour interval. The ERA-interim forced WRF (ERA-WRF) proves the value of dynamical downscaling, which yields more realistic topographical-induced precipitation and air temperature, as well as corrects underestimations in observed precipitation. In summary, dry and cold biases to the north of the Brooks Range are presented in ERA-WRF, while CESM forced WRF (CESM-WRF) holds wet and warm biases in its historical period. A linear scaling method allowed for an adjustment of the biases, while keeping the majority of the variability and extreme values of modeled precipitation and air temperature. CESM-WRF under RCP 4.5 scenario projects smaller increase in precipitation and air temperature than observed in the historical CESM-WRF product, while the CESM-WRF under RCP8.5 scenario shows larger changes. The fine spatial and temporal resolution, long temporal coverage, and multi-scenario projections jointly make the dataset appropriate to address a myriad of physical and biological changes occurring on the North Slope of Alaska.

---

[1] Cai L, Alexeev VA, Arp CD, Jones BM, Liljedahl AK and Gädeke A (2018) The Polar WRF Downscaled Historical and Projected Twenty-First Century Climate for the Coast and Foothills of Arctic Alaska. *Front. Earth Sci.* 5:111. doi: 10.3389/feart.2017.00111

2.1 Introduction

The air temperature is increasing and more so in the northern high latitude regions due to the polar amplification (Alexeev et al., 2005; Serreze and Francis, 2006). Annual mean surface air temperatures from observations and reanalysis datasets have increased more than 2.5 °C poleward of 60° N since the 1970s, which is of over 1 °C more warming than that in the mid-latitudes (30-60° N) (Johannessen et al., 2004). Arctic sea ice cover is declining more than 3×10^5 km per decade (Serreze et al., 2007). The declining sea ice accounts for a positive surface albedo feedback, which acts as a contributing factor, though not the dominating one, to the polar amplification phenomenon (Winton 2006; Serreze and Francis, 2006).

The exact mechanism of polar amplification is still under active discussion, but it is agreed that the rapidly increasing air temperature and the declining sea ice cover since the 1970s have led to substantial environmental changes to the pan-Arctic coastal regions. For example, the permafrost temperature in the western North American Arctic has warmed by 0.5-4 °C since the 1970s (Smith et al., 2010, Romanovsky et al. 2010), resulting in active layer thickening (Grosse et al., 2016) and permafrost degradation (Jorgenson et al., 2006; Lantz and Kokelj, 2008; Liljedahl et al., 2016). Other changes include, but are not limited to, thermokarst lake drainage (Plug et al., 2008; Jones et al., 2011; Jones and Arp, 2015; Lantz and Turner, 2015), thinner lake ice (Arp et al., 2012; Alexeev et al., 2016), longer unfrozen Arctic lake surface (Brown and Duguay, 2010), more lake surface evaporation (Arp et al., 2015), and extended growing season (Hinzman et al., 2005; Tape et al., 2006; Bhatt et al., 2008; Chapin III et al., 2012). Post et al. (2009) pointed out that the amount and types of impacts are still underreported and the understanding of the underlying physical mechanisms are still lacking due to insufficient observations in the Arctic.

Climate monitoring in the Arctic have been restricted by the lack of observational sites that are sparsely distributed, and few of which are observing routinely (Shulski and Wendler, 2007). The observation accuracy is hard to maintain in such a harsh environment, especially for the solid precipitation observation that is usually underestimated by a factor of two or more (Groisman et al., 1991; Rasmussen et al., 2012; Liljedahl et al., 2017). Conventional snowfall measurements are underestimated for the reasons including high wind speeds and trace precipitation events (Black, 1954; Liston and Sturm, 2002; Rasmussen et al., 2012). Despite problems with cold season precipitation measurements, the observed long-term records of air temperature are reliable (Vose et al., 2007).

Numerical simulations complement the limited field observations in Alaska and other Arctic regions. The latest Earth System Models (ESMs) has improved significantly in retrieving climatic variables coupling the atmosphere, land, ocean, and ice models (de Boer et al., 2012; Mortin et al., 2013; Koenigk et al., 2014). Still, the typical one-degree grid spacing prevents ESMs from resolving more detailed weather like Mesoscale Convective Systems (MCS) and topographical-induced precipitation. Dynamical downscaling using Regional Climate Models (RCMs) forced by reanalysis data and/or ESM output is one way to amplify the mesoscale features and to retrieve high-resolution climatic variables regionally (Wilby and Wigley, 1997). The North American Regional Climate Change Assessment Program (NARCCAP) is a dynamical downscaling program with the ensemble of GCM-RCM combinations that serves the high-resolution climate scenario needs for the North America (Mearns et al., 2013). The mesoscale framework in NARCCAP results in more extreme precipitation events compared to the GCMs, and becoming less deviated from observations (Gutowski et al., 2010; Wehner 2013). Coordinated Regional climate Downscaling Experiment (CORDEX) is another project that employed dynamical downscaling over multiple regions of interest around the globe (Europe, South Africa, East Asia, etc.) (Giorgi et al., 2009). CORDEX addresses dynamical downscaling forced by the latest generation of GCMs that are archived in Coupled Model Intercomparison Project Phase 5 (CMIP5) instead of its earlier phase (CMIP3) is selected in NARCCAP (Giorgi et al., 2009; Taylor et al., 2012; Mearns et al., 2013).

Dynamically downscaled ERA-interim reanalysis data already exist for Alaska as a whole, with a grid spacing of 20 km using Weather Research and Forecast (WRF) model (Bieniek et al. 2016). Here, the modeling configuration is tuned to emphasize the general climate divisions of Alaska (e.g. interior Alaska versus coastal regions) and the distribution/frequency of extreme events. Chukchi–Beaufort High-Resolution Atmospheric Reanalysis (CBHAR) is another WRF-based downscaling product that focuses on the Arctic Alaska and the adjacent oceanic area to its north with a 10-km grid spacing and 1-hour output interval (Liu et al., 2014). By involving WRF-Data Assimilation (WRFDA) system that imports satellite data, CBHAR represents a refined wind field in the Chukchi and Beaufort Seas regions (Zhang et al., 2016). Yet, a downscaled dataset centering on the Arctic land of Alaska has, until now, been unavailable. Here our objectives are to produce and present fine temporal (3-hourly) and spatial (10 km) downscaled historical atmospheric data with multi-projections representing the differing scenarios (RCP4.5 and RCP8.5) of climate change in Arctic Alaska from year 1950 up until 2099.

2.2 Methodology

2.2.1 Site Description

Our downscaling products center on the Arctic Coastal Plain of Alaska and the Northern foothills of the Brooks Range (Figure 2.1). We use the term “the North Slope of Alaska” to describe the part of Alaska approximately to the North of 69°N. The Brooks Range, which has quite a few mountain peaks higher than 2000 meters in altitude acts as a barrier, preventing warm and wet air from the Bering Sea reaching the North Slope of Alaska (Shulski and Wendler, 2007). The region has the lowest mean annual air temperatures (< -10°C) and annual precipitation (~150 mm) observed in Alaska, both of which decrease along a gradient from the Brooks Range foothill to the Northern coast of Alaska (Stafford et al., 2000). The polar days in summer and nights in winter reduce the diurnal variation of solar radiation down to a level less than 30% of that in the mid-latitudes (Maykut and Church, 1973). The weakened diurnal cycle excludes solar radiation from being the leading control of the diurnal cycle of air temperature. Instead, it is the cloud cover and low-level wind that primarily drive the diurnal cycle of air temperature during polar days and nights (Dai et al., 1999; Przybylak, 2000).

Multiple observational and model-based studies have found that the Arctic sea ice has been declining since the 1970s. The sea-ice decline favors increased precipitation during the late fall and the early winter (Deser et al., 2010; Porter et al., 2012; Screen et al., 2013). Under the most extreme scenario in the Community Earth System Model (CESM) projection, the continuous Arctic sea ice decline eventually makes an ice-free September in the Arctic Ocean by the end of the 2040s (Wang and Overland, 2012). Projection under less extreme scenarios shows a declining rate of sea ice loss with sea ice minima remaining constant after the year 2070 (Bintanja et al., 2013; Meehl et al., 2013). Such difference in sea ice extent may influence the seasonal cycles of air temperature and precipitation.

2.2.2 Polar weather research & forecast model

WRF is a flexible, state-of-the-art regional atmospheric modeling system (Skamarock et al., 2008). Previous modeling studies by polar MM5 (The Fifth-Generation Penn State/NCAR Mesoscale Model, with polar optimization) have emphasized the necessity of refining the parameters in surface background and physics schemes in terms of the Arctic regions (Cassano et al., 2001). We, therefore, employed the polar WRF (version 3.5.1), an Arctic-optimized WRF model plug-in, which was released by Polar Meteorology Group of the Byrd Polar and Climate Research Center at Ohio State University (Hines et al., 2009; Hines et al., 2011). Polar WRF model includes the upgraded physics schemes and revised land-use parameterizations specifically for both the terrestrial and oceanic Arctic (Hines et al., 2009; Wilson et al., 2011, 2012).

2.2.3 Forcing datasets and model validation to observations

ERA-interim reanalysis and Community Earth System Model version 1.0 (CESM1.0) output are used to force polar WRF in the period of 1979-2014. The historical WRF simulations (from 1950 to 2005) are forced by the CESM 20th century all-forcing simulation output, while the future projections (the year 2006 to 2100) are informed by two scenarios of "Representative Concentration Pathways" (RCP4.5 and RCP8.5). Comparisons are conducted between the downscaled products (ERA-WRF), its forcing (ERA-interim), and the field observations (Global Historical Climatology Network Daily-summaries, GHCN-D). All products are bias-corrected based on the monthly climatology of ERA-interim.

2.2.3.1 ERA-interim

ERA-interim, as the latest generation of reanalysis dataset by European Center for Medium-range Weather Forecast (ECMWF), serves atmospheric, land, and ocean elements in a T255 spectral resolution (roughly 80 km) globally (Dee et al., 2011). ERA-interim is made by models and data assimilation systems that ingest observations every 6-12 hours (Dee et al., 2015). As an upgraded version of ERA-40, ERA-interim is empowered by Four-Dimensional Variational (4D-Var) data assimilation updated from the 3D-Var in ERA-40, making ERA-interim more observational-oriented (Lorenc and Rawlins, 2005; Whitaker et al., 2009). An improved representation of hydrological processes such as evaporation, condensation, and runoff has resulted in a refined accuracy of air temperature and moisture fields in ERA-interim (Dee et al., 2011). Most importantly, ERA-interim outperforms other reanalysis products in producing representative climatic variables over the high-latitudes (Jakobson et al., 2012, Lindsay et al., 2014).

2.2.3.2 Community Earth System Model 1.0

ESM-forced downscaling products are based on the CESM1.0 output. CESM is a group member of CMIP5 assembling the most advanced ESMs projecting the future global climate for the fifth Assessment Report (AR5) by International Panel on Climate Change (IPCC; Vertenstein et al., 2011; Taylor et al., 2012; Collins et al., 2013). One 20th century all-forcing simulation (1950-2005) and two RCP scenarios (RCP4.5 and RCP8.5) for 21st-century projection (2006-2100) respectively forced Polar WRF. We chose the ensemble member of MOAR ("Mother of All Runs"). MOAR, represent the 12th member for the 20th century, the 6th member for RCP4.5, and the 7th member for RCP8.5. MOAR is the only ensemble member that is with a 6-hourly output frequency, which is essential in building WRF boundary conditions. RCP projects a radiative forcing of 4.5 Wm^{-2} for RCP4.5, and 8.5 Wm^{-2} for RCP8.5 by prescribing the greenhouse gases emission increase in the 21st century. The RCP4.5 projects a mild global air temperature increase under stricter greenhouse gas control policies, while The RCP8.5 scenario prescribes uncontrolled greenhouse gas emissions and an extreme global warming (Moss et al., 2010; Riahi et al., 2011; Thomson et al., 2011). RCP8.5 helps to build the maximal global warming trend, while RCP4.5 fits closer to the observed global temperature change in the first decade of the 21st century, which has indicated a "braking" in global warming (Guemas et al., 2013).

2.2.3.3 Observation Data for Validation

North Slope of Alaska observation sites included in the GHCN-D observation data from National Climatic Data Center (NCDC) that are operating in the long-term are few. Five weather stations, Utqiaġvik (formerly Barrow), Wainwright, Deadhorse, Nuiqsut, and Umiat, include daily precipitation and air temperature with less than 10% of missing data since 1980 (Figure 2.1). Here, we compared the GHCN-D monthly climatology of daily precipitation (PRCP), daily maximum temperature (TMAX), and daily minimum temperature (TMIN) to the ERA-interim dataset and ERA-WRF output, respectively. We present monthly climatology comparisons at Nuiqsut and Utqiaġvik and are including other sites in the supplemental material. We bi-linearly interpolated ERA-interim variables and extracted WRF-outputs at the WRF grid point that was nearest to respective observation station. WRF's high resolution enables us to apply nearest neighbor interpolation method without generating unacceptable errors. In ERA-interim and WRF, the temperature record at 00:00 UTC (3 pm local time) in four (ERA-interim, 6-hourly) or eight (WRF, 3-hourly) records each day are defined as the TMAX, while the one at 12:00 UTC (3 am local time) as the TMIN. NCDC GHCN-D data records the maximum and minimum daily air temperature, while ERA-WRF and ERA-interim do not. Therefore, biases may inevitably arise during comparisons.

2.2.4 Model initialization

The North Slope of Alaska is located in the center of the simulation domain, which covers part of the Beaufort Sea and the Chukchi Sea to the north, and Fairbanks to the south, forming a 180×150 gridded area with a 10 km horizontal grid spacing, that is, a 2.67×10^6 km^2 of area (Figure 2.1). The temporal coverages are identical to the forcings, i.e. years 1979-2014 for ERA-WRF, 1950-2005 for the historical CESM-WRF, and 2006-2100 for the projected CESM-WRF. All runs started on July 1^{st} in their first year of forcing. The first six months were the spin-up time and were excluded from the data analysis. We used the CESM output in a WRF intermediate file format downloaded from the Computational & Informational System Lab (CISL) Research Data Archive (ds316.0, no longer available online) to save computational time and expenses. Among the final downscaling products (Figure 2.2), CESM-WRF (historical and projected) offers climatic background based on the coarser-resolution GCM (CESM) output but with mesoscale dynamics and physics involved. On the other hand, the role of ERA-WRF is not only to offer a dynamically downscaled reanalysis dataset but also to validate the configuration of regional climate model (WRF in this case), as the climatic variables in it are directly comparable to observations. It is assumed that WRF simulates in the same manner forced by ERA-interim and CESM when with the same configuration (spatial/temporal resolution, time step of integration, parameterization of physics, etc.). Such workflow is commonly applied to dynamical downscaling projects, including NARCCAP and CORDEX (Giorgi et al., 2009; Mearns et al., 2013).

Parameterization schemes were set to favor high-resolution, long-term runs. Multiple parameterization schemes were employed for various physical processes. For microphysics, WRF single-moment 5-class scheme (WSM5) was chosen (Hong et al., 1998). Rapid Radiation Transfer Model (RRTM) (Mlawer et al., 1997) and Dudhia scheme (Dudhia 1996) were for parameterizing longwave and shortwave radiations, respectively. The Noah land surface scheme (Noilhan and Planton 1989) was responsible for land surface processes, and the Yonsei University scheme (Hong and Dudhia 2003) parameterized planetary boundary layer dynamics. Cumulus clouds were parameterized by the Kain-Fritsch convective scheme (Kain 2004).

Multiple year-long test runs with different combinations of schemes were conducted before determining the combination of parameterization schemes. Double-moment microphysical parameterization schemes resulted to bring higher air temperature and precipitation biases in spring and early summer, which was caused by the overestimation of cloud forming that reduced downward shortwave radiation at surface. We, therefore, turned to WSM5 scheme, a less advanced but more mature microphysical scheme that has shown more suitable for long-term modeling (Hong et al., 1998).

Nudging pulls values of key variables back to the forcing in a certain frequency in the entire simulation process, which helps to prevent model output deviating from the forcing (Glisan et al., 2013). However, while doing so, you also damage the physical correlation between the produced climatic variables, bringing higher uncertainty to the final product (Radu et al., 2008; Liu et al., 2012; Bullock et al., 2014). Data assimilation has the similar effect as it imports external data source into the modeling process (Fujita et al., 2007). We did not include any nudging or data assimilation during the computation in order to keep the full dynamical framework of WRF model intact and to allow the output variables to be physically correlated. Instead, to address any biases we adjusted model outputs by comparing results to observations after all computation was completed.

2.2.5 Bias correction

The WRF simulation in this study inherits the biases from its forcings (i.e. ERA-interim and CESM outputs) as no nudging was involved in the downscaling process. In this case, the linear scaling method corrected the biases by rescaling the Probability Density Functions (PDFs), fitting the modeled monthly climatology to its reference (Lenderink et al., 2007; Teutschbein and Seibert, 2012). We employed a relatively simplistic bias correction approach to retain a majority of the sub-daily/daily variability in precipitation and air temperature while fitting the long-term climatology to the reference.

Two sets of bias-correction formulas resulted from two different PDFs distributions that precipitation and air temperature respectively hold. Climatologically, temperature PDFs generally obey normal distributions, while daily precipitation PDFs generally obey two-parameter gamma distributions (Harmel et al., 2002; Hanson and Vogel, 2008). The formulas for precipitation are represented by:

$$P_{his}^{*}(d) = P_{his}(d)\frac{\mu_m(P_{ref}(d))}{\mu_m(P_{his}(d))} \qquad (1)$$

$$P_{prj}^{*}(d) = P_{prj}(d)\frac{\mu_m(P_{ref}(d))}{\mu_m(P_{his}(d))} \qquad (2)$$

in which $P_{his}^{*}(d)$ and $P_{prj}^{*}(d)$ are daily bias-corrected historical and projected precipitation, respectively, $P_{his}(d)$ and $P_{prj}(d)$ are the originals, and $P_{ref}(d)$ is the daily reference precipitation. d is the notation standing for a certain day (data point), while μ_m stands for the function calculating the monthly climatology.

The formulas for air temperature follow as:

$$T_{his}^{*}(d) = T_{his}(d) + \mu_m(T_{ref}(d)) - \mu_m(T_{his}(d)) \qquad (3)$$

$$T_{prj}^{*}(d) = T_{prj}(d) + \mu_m(T_{ref}(d)) - \mu_m(T_{his}(d)) \qquad (4)$$

where the terms represent the air temperature and are otherwise the same as in the precipitation correction equations. References for linear scaling are ERA-interim monthly precipitation and temperature climatology. We also correct the biases in variables of snow water equivalent; dew point temperature, wind speed, and surface pressure and include them in the released dataset. Details of bias correcting other variables are presented in the supplemental material.

We are working under the assumption that the bias in the means calculated over the base period in the projected fields will stay the same with time. This is a commonly used approach (Teutschbein and Seibert, 2012; Bruyère et al., 2014). Note that we are not applying any targeted techniques to adjust variability in the modeled fields to the observed. We did not use the bias-corrected version of CESM output in the WRF intermediate file format (CISL ds316.1, Bruyère et al., 2014) for downscaling. As mentioned above, we are using raw CESM output in the WRF intermediate format instead, and apply bias correction to WRF fields after the simulation. As a cautionary note, bias correction procedure applied to precipitation will slightly modify the projected trends in the corrected fields.

Variables of model outputs mentioned in this manuscript, both before and after bias correction, are available through IARC data archive (http://data.iarc.uaf.edu/) and PANGAEA (https://doi.pangaea.de/10.1594/PANGAEA.863625). Other variables are also available upon request by contacting Lei Cai (lcai4@alaska.edu) or Vladimir Alexeev (valexeev@alaska.edu).

2.3 Results

2.3.1 ERA-WRF evaluation

Our downscaling products are developed primarily for the North Slope of Alaska, while the area for evaluating them is extended until the South of the Brooks Range for a broader picture of performance. The downscaled ERA-WRF precipitation and air temperature climatology illustrate similar overall spatial distributions as its forcing, ERA-interim reanalysis data (Figure 2.3). However, the higher spatial resolution allows ERA-WRF to represent more detailed topographic features than ERA-interim. Differences include a higher amount of precipitation to the south and lower amount to the north in ERA-WRF compared to ERA-interim (Figure 2.3a-c). The ERA-WRF air temperature in the mountain regions is distributed following the topography, where the colder areas coinciding with mountain peaks in the eastern Brooks Range where the altitude is higher than 1500 m (Figure 2.3d). To the north of the Brooks Range, the ERA-WRF generally produces a drier (60-120 mm/year for precipitation) and a colder (2 to 3 °C lower mean annual air temperature) climatology compared to ERA-interim. At the northernmost site (Utqiaġvik), the annual air temperature bias reaches its maximum (up to 4 °C colder in ERA-WRF compared to ERA-interim), while the precipitation bias reaches +60 mm/year. Warm biases (up to 2 °C) are constrained to the mountain region mean annual air temperature (altitudes from 500 m to 1500 m). A section across the Brooks Range (red dashed line in Figure 2.3a) unveils a detailed view of the enhanced topographic effect to the more detailed terrain in WRF (Figure 2.3e-g). Precipitation and temperature in ERA-interim are monotonically decreasing towards North. ERA-WRF, however, presents double the annual precipitation amount of ERA-interim's (1200 mm/year vs. 600 mm/year) on the south slope of the Brooks Range (Figure 2.3e). ERA-WRF also presents local minima of annual mean temperature on the mountain peaks (Figure 2.3f). An even higher variability of precipitation and temperature following the topography is presented by a 2-km resolution statistically downscaled dataset from Scenarios Network for Alaska and Arctic Planning (SNAP, 2017). However, there is no easy way to directly compare high resolution of SNAP dataset with observations or WRF-generated output. The mismatch between the real and model (or e.g. SNAP) topography and lack of high quality observations are the two main reasons why such comparisons should be done with a great deal of caution.

2.3.2 Comparison to observations

Monthly climatology comparisons to observations at Nuiqsut and Utqiaġvik show that both modeled datasets (ERA-WRF and ERA-interim) present similar seasonal variability in precipitation, TMAX, and TMIN as the NCDC GHCN-D observations (Figure 2.4). However, modeled precipitation (ERA-WRF and ERA-interim products) consistently exceeds observations, while air temperature differences are more complex.

Dry biases occur mainly during October to February when ERA-WRF produces 30 to 50% less precipitation than ERA-interim at Nuiqsut (Figure 2.4a). The ERA-WRF wet bias compared to ERA-interim mostly results from higher April to October precipitation at Utqiaġvik. The wet bias reaches +30% in the months of August and September. For the rest of the year, ERA-WRF and ERA-interim have nearly the same amount of monthly precipitation (Figure 2.4b). ERA-WRF and ERA-interim consistently produce 50 to 150% more precipitation than observations at Nuiqsut and Utqiaġvik. Differences to observations are largest during the colder months (October to March) with 70 to 120 mm more precipitation than observed. As an example, total precipitation climatology (1980-2014) observed October to March was 7.8 and 32.1 mm (Nuiqsuit and, respectively), while ERA-WRF and ERA-interim suggested 110.4 and 70.8 mm, as well as 132 and 84.3 mm for Nuiqsut and Utqiaġvik respectively.

Correlation coefficients of monthly observed precipitation, TMAX, and TMIN are calculated in all five weather stations to both ERA-WRF and ERA-interim after removing the seasonal cycles (Figure 2.5). The results indicate that the modeled time series of precipitation is correlated to observations. Correlation coefficients of both ERA-WRF and ERA-interim precipitation to observations are around 0.5 (> 0.49 for 95% significance level) in most cases. Precipitation from ERA-WRF is more closely correlated to observations than ERA-interim at four out of five stations. Normalized standard deviations (SDs) of ERA-WRF and ERA-interim precipitation are larger than 1 in all cases except for ERA-interim precipitation at Wainwright. Such higher SDs indicate that the daily precipitation in both ERA-WRF and ERA-interim are with higher day-to-day variations than observation is, which typically the result of heavier rainfall events in ERA-WRF and ERA-interim.ERA-WRF simulates cooler TMAX than the observed in all months except for April and May at both Nuiqsut and Utqiaġvik (Figure 2.4c-d). The TMAX difference averages up to 5 °C in summer (July to August) and 8 °C in winter (October to March). For TMIN, ERA-WRF produces a slightly warmer (< 3 °C) monthly TMIN than observation from January to May at Nuiqsut, while TMIN is almost identical for other months (Figure 2.4e). This is in contrast to the ERA-WRF TMIN results at Utqiaġvik that are colder in winter than observations (< 1 °C in January to October and 2 °C in November and December) (Figure 2.4f). The biases of ERA-WRF TMIN to observation at Utqiaġvik are negligible in other months.

Diurnal temperature variations in both ERA-WRF and ERA-interim almost disappear in months from November to February. In these months, differences of TMAX and TMIN (TMAX minus TMIN) in ERA-WRF and ERA-interim are less than 1 °C, while the GHCN-D observations show 5-8 °C diurnal air temperature variation.

Daily TMAX and TMIN in ERA-WRF and ERA-interim are more correlated to observations than daily precipitation. Correlation coefficients for TMAX and TMIN are between 0.7 and 0.8 in all cases, which shows the significance of correlation and is 0.2 to 0.4 higher than the correlation coefficients for precipitation (Figure 2.5). Typically, TMIN in both ERA-WRF and ERA-interim are more correlated to observations than TMAX. In all stations except Wainwright, ERA-WRF produces TMAX and TMIN with higher variabilities than observations (120% on SDs) and ERA-interim. ERA-interim produces TMAX and TMIN that are around 80% of SDs from observations at all five stations.

2.3.3 Statistics on bias correction

The cumulative probability functions of daily precipitation and mean air temperature in ERA-WRF and CESM-WRF historical products are changed after the bias correction (Fig. 6). Compared to the model reference dataset (ERA-interim), the non-bias-adjusted ERA-WRF has more records (days) with no precipitation (< 0.1 mm/day) or with light drizzles (< 1 mm/day). On the contrary, the original CESM-WRF historical product shows a wet bias compared to ERA-interim. CESM-WRF has fewer days with no precipitation or light drizzles compared to ERA-interim, but more heavy precipitation events (>8 mm/day) (Fig. 6a). The daily precipitation biases from ERA-WRF and CESM-WRF are adjusted via a 4.9 % increase for ERA-WRF and a 30% decrease for CESM-WRF on respective long-term means based upon the climatology in ERA-interim. Both of the downscaling products also show decreased variances by 19 % (ERA-WRF) and 47 % (CESM-WRF) after correcting the biases. Showing on the cumulative probability curves, CESM-WRF precipitation closely fits the reference (ERA-interim) after the bias correction, while the biases in ERA-WRF precipitation are not corrected effectively on the drizzle side (<1 mm/day).

Generally, the linear scaling corrects precipitation more than air temperature. For daily air temperature, the cold bias in ERA-WRF and warm bias in CESM-WRF are corrected with a 1.4 °C and a -2.8 °C changes, respectively (Figure 2.6b). The historical CESM-WRF simulates a warm bias in air temperature, also it underestimates seasonal cycle. Applying monthly seasonal bias correction leads to a 37% increase in seasonal variability in CESM-WRF. A similar bias correction applied to ERA-WRF results in a slight decrease (-3.3%) in the seasonal cycle of air temperature.

CESM-WRF received a larger bias-corrections on both daily precipitation and air temperature compared to ERA-WRF. The bias correction on CESM-WRF produces more days with light drizzles and cold air temperatures (temperature < 0 °C) due to its original warm and wet biases. The bias corrections on ERA-WRF addressed mostly its cold and dry biases.

2.3.4 CESM-WRF projection

All estimates presented in this section are averages for the whole domain of the North Slope as defined in section 2.1. All three CESM-WRF products exhibit increasing trends in annual precipitation and air temperature (Figure 2.7a-b). Precipitation from CESM-WRF RCP8.5 has the largest increasing trend (nearly +1 mm/year), resulting in an annual precipitation of nearly 500 mm by the end of the 21st century compared to 400 mm at present. In comparison, the annual precipitation in the historical and the RCP4.5 products increase only 0.62 and 0.36 mm/year, respectively. The RCP8.5 projection has also the largest increasing trend of annual mean temperature. The RCP4.5 projection, on the other hand, presents an increasing trend of precipitation that is smaller than the historical simulation. By the end of 21st century, the North Slope of Alaska experiences a 5 °C warmer annual mean air temperature in RCP8.5 compared to the RCP4.5 scenario (8.5 °C vs. 3.5 °C, respectively). The historical simulation (from 1950 to 2005) shows a 3.1 °C air temperature rise.

In order to compare the annual and the seasonal trends of precipitation, we calculated both the precipitation amounts and trends based on the daily precipitation rate (mm per day). All three products (CESM-WRF historical, RCP4.5, and RCP8.5) produced the most precipitation in summer (JJA, 1.5-2 mm/day on average) and least in winter (DJF, 0.6-0.8 mm/day on average) (Figure 2.7c). Higher annual and seasonal precipitation amounts are found in the 21st-century projections compared to the historical precipitation. The RCP8.5 projection has more precipitation than the RCP4.5. The summer (JJA) is also found with the largest increasing trends of precipitation in the historical (0.004 mm/day per year) and RCP4.5 products. For the RCP8.5, however, the largest increasing trend of daily precipitation rate is in fall (0.005 mm/day per year). In winter, RCP8.5 precipitation also increases rapidly (over 0.002 mm/day per year). Trends in winter precipitation in the historical and the RCP4.5 (0.002 and -0.001 mm/day per year) are substantially smaller than summer (0.004 and 0.003 mm/day per year).

Both the RCP4.5 and the RCP8.5 projections produce increases in air temperature in all four seasons. Increase in winter air temperature are largest (Figure 2.7d). RCP8.5 results in an air temperature increase of 0.15 °C/year during winter, which is more than in any other season (from 0.06 to 0.08 °C/year). Similar, albeit not as large, seasonal trends are found in the RCP4.5 scenario. The larger warming in winter than summer implies a reduced seasonal variation of air temperature in the 21st-century projections.

2.4 Discussion

Dynamical downscaling by the Polar WRF model presents refined climate products in regards to spatial and temporal distributions of precipitation and air temperature for the North Slope of Alaska. The coarse (roughly 80 km) grid spacing of ERA-interim is not sufficient to effectively represent the topographical effects on air temperature and precipitation. Such a coarse resolution underestimates the complexity of topography in Arctic Alaska; for example, the highest peak of the Brooks Range has the elevation of 1836 meters in WRF while the same peak is only 1070 meters in ERA-interim. Such enhancement of topography in WRF is important for our area of interest, the North Slope of Alaska, for which the Brooks Range plays an important role in its regional climate. The Brooks Range in WRF obstructs more of the warm and wet air from reaching the North Slope of Alaska than in ERA-interim. Although such enhancements due to the topographical effect cannot be precisely quantified from the ERA-WRF simulations, it is clear that the more detailed topography in ERA-WRF results in higher precipitation and temperature on the southwest side, while lower ones on the north side, of the Brooks Range compared to ERA-interim (Figure 2.3). The warmer winter temperatures in the mountainous area of the Brooks Range at 500~1500 meters altitude are likely to result from the enhanced vertical resolution in the atmosphere interacting with micro-topography in ERA-WRF that causes stronger modeled inversions in valleys.

Both ERA-WRF and ERA-interim produce more than double the amount of winter precipitation compared to available observations. Conventional snowfall observations are known to have issues with underestimation and accuracy in general (Groisman and Rankova, 2001; Bogdanova et al, 2002; Groisman et al, 2004), making quantitative analysis difficult. Differences between modeled and observed precipitation in this study are comparable (100~400 %) to the assessments done by Liljedahl et al. (2017), which compared conventional snowfall measurements to end-of-winter snow accumulation near Utqiaġvik, Alaska. In summary, our downscaled annual mean precipitation is likely to be more realistic than that derived from ERA-interim or CESM.

Evaluation experiments by the Polar WRF group found a cold bias in winter on the North Slope starting with Polar WRF version 3.1.1 (Hines et al., 2009; Hines et al., 2011). As we found here, the winter cold bias remains in polar WRF version 3.5.1. ERA-WRF produces smaller biases in TMIN (-1 to -3 °C) than in TMAX (-5 to -8 °C) when compared to observation. Hines et al. (2011) discovered that polar WRF overestimates downwelling longwave radiation (cloudier days and nights) while underestimates wind speed from January to March in Barrow in the test simulations, both contributing to the decrease in the wintertime diurnal temperature variation in Arctic Alaska. Tuning of cloud and longwave radiation schemes may help reduce such biases slightly, while a significant improvement on retrieving diurnal cycle of temperature in winter depends on the upgrades of polar WRF itself. Modeled TMIN and TMAX were obtained from values at fixed times each day 3 am and 3 pm) as the model output was presented every 3h. However, the observed values are the actual recorded (sub-hourly) extreme value for each day. We evaluated the effect of this potentially method-induced bias. The applications for which our downscaled products have been developed primarily utilize data in the form of daily/monthly means instead of diurnal extremes, so that the impacts of such deficiencies have been minor.

The historical CESM-WRF generally simulates a wet bias in precipitation and a warm bias in air temperature compared to ERA-interim. Most biases in CESM-WRF resulted from biases in CESM. CESM1.0 historical product evaluation found warm biases on air temperature and wet biases on precipitation compared to ERA-interim over the Northern Alaska and the Beaufort and the Chukchi Seas to the North, and the maximum warm (+5 °C) and wet biases (+100%) are both present in winter, similar to de Boer et al., (2012). CESM-WRF in this study retains at least part of such deficiencies of CESM, having higher precipitation and air temperature biases than ERA-WRF in the historical period. De Boer et al. (2012) also unveiled the deficiency of CESM1.0 in underestimating total cloud fraction all year round over the Arctic Alaska compared to observation. CESM-WRF in this study has improved performance in retrieving cloud cover over CESM due to higher spatial resolution and more complex physics schemes. Walston et al. (2014) found that CESM1.0 underestimates the seasonal cycle of air temperature over the Arctic through warmer winters and colder summers compared to reanalysis data. The similar seasonal variability is muted in our CESM-WRF simulations, which is partially improved by the bias-correction that imports the ERA-interim seasonal cycles.

Downscaled projections forced by RCP4.5 produced a lower increase in annual total precipitation (+0.36 mm per year) than the historical product (+0.62 mm per year). RCP8.5 informed projections show the largest trend (+0.99 mm per year). Almost half of the precipitation increase in RCP8.5 occurs in October through December. The large increase in fall precipitation may be attributed to the rapid sea ice decline in the CESM RCP8.5 product (Alexeev et al., 2016). CESM-WRF historical product presents larger positive trends of precipitation and air temperature than the RCP4.5 projection. We attribute it to the choice of years we set as the historical period (1950-2005), which coincides with the strongest climate change during the whole historical simulation period of CMIP5 models (1850-2005). On the contrary, the RCP4.5 scenario features a stabilization of global warming, so that the global mean temperature increase slows down after 2060, which is reflected on all CMIP5 models (Collins et al., 2013). Since our projected trends are calculated for the period of 2006-2100, such "deceleration" of global warming after 2060 in RCP4.5 scenario lowers the overall increasing trend. Specifically for the Arctic Alaska, the sea ice decline in RCP4.5 scenario also slows down after 2050 to a rate that is lower than our historical period (1950-2005) (Stroeve et al., 2012). Such changes in sea ice also inhibit the increase of precipitation and air temperature, primarily in late fall and early winter (Stroeve et al., 2007).

We did not address comparisons between the projected CESM-WRF and the original low-resolution CESM RCP projections, as such analysis is less informative because the applied bias correction procedure inevitably brings artifacts to climatic variables. While the boundary forcing for WRF can come from different products (ERA-Interim or CESM), the dynamics and physics in the interior of the domain (North Slope of Alaska in this case) are determined entirely by WRF. The downscaling of ERA-interim, CESM historical products, and CESM future projections is done in this study under an identical setting (spatial/temporal resolutions, integrating time step, physics schemes, etc.). Our ERA-WRF evaluation comparing with ERA-interim and observations have demonstrated the role of WRF and its configurations in improving the quality of fields by applying the dynamical downscaling over the North Slope of Alaska. We argue that our CESM-WRF products have more realistic mesoscale features and therefore are superior compared to the original CESM output (historical and projected) including the effects of enhanced topography and more extreme precipitation.

Our downscaling data products present high spatial grid spacing (10 km), long temporal coverage (1950-2100), high-frequency output (every 3h) and are the only multi-scenario climate projections (RCP4.5 and RCP8.5) for the Arctic Alaska. Without any nudging or data assimilation, the ERA-WRF and CESM-WRF products for the historical period have higher biases compared to observations than the datasets developed by Bieniek et al. (2016) and Zhang et al. (2016). Here, we deal with these biases by applying linear scaling bias corrections, which resulted in biases being corrected towards the ERA-interim reanalysis dataset. The historical ERA-WRF and CESM-WRF climate products combined with future warming scenarios (RCP4.5 and 8.5) make our dataset particularly suitable for the regional climate change studies over the North Slope of Alaska.

2.5 Conclusions

This paper introduces a set of dynamical downscaling products forced by both ERA-interim reanalysis data and CESM model output. The model evaluation shows that the dynamical downscaling process resolves more detailed topographical effects on the regional climate of the North Slope of Alaska compared to its forcing datasets. The higher resolution surface topography in WRF (compared to the low-resolution topography in ERA-Interim and CESM) helps reproduce more reasonable climate background in Arctic Alaska that has a complex terrain. The modeled annual mean precipitation is 100~400% higher compared to observations, the reasons of which are highly debatable, including the lack of high quality observed precipitation datasets in the high Arctic. The WRF-modeled precipitation also increases seasonal variability compared to the original forcing products. We view the dynamical downscaling as a valid approach to producing not only more realistic long-term mean products, but also more extreme events that can only be represented in the mesoscale framework. The two downscaled products that project the 21st-century regional climate agree on a trend towards a warmer and wetter North Slope of Alaska. The RCP4.5 simulation exhibits a smaller increasing trend in precipitation and air temperature compared to the RCP8.5 products. The projected increases by RCP4.5 are even lower than that of the historical product. Trends are largest in fall and winter in the RCP8.5 projections. More detailed study on the CESM-modeled sea ice decline impacts may help to explain such differences. The downscaled data products of high-resolution, long temporal coverage and multi-scenario future projections have the potential to refine climate change studies over the North Slope of Alaska and ultimately resulting in more effective impact assessments for the people living in the region due to the finer spatial and temporal scales and improved representation of extreme events.

Acknowledgements

Funding for this research is provided by National Science Foundation (ARC-1107481 and ARC-1417300) and the Arctic Landscape Conservation Cooperative. We thank Andrew Monaghan for converting and sharing CESM data in a WRF intermediate data format. We thank Benjamin Gaglioti for proofreading and helpful comments on polishing the language. Any use of trade, product, or firm names is for descriptive purposes only and does not imply endorsement by the U.S. Government. In terms of authors' contribution, Lei Cai develops the dataset, does data analysis, and drafts the manuscript. Vladimir Alexeev, Christopher Arp, Benjamin Jones, and Anna Liljedahl set the design of the work, give critical ideas and revision comments on data analysis and manuscript writing. Anne Gädeke helps on dataset development and data analysis, and gives critical revision comments.

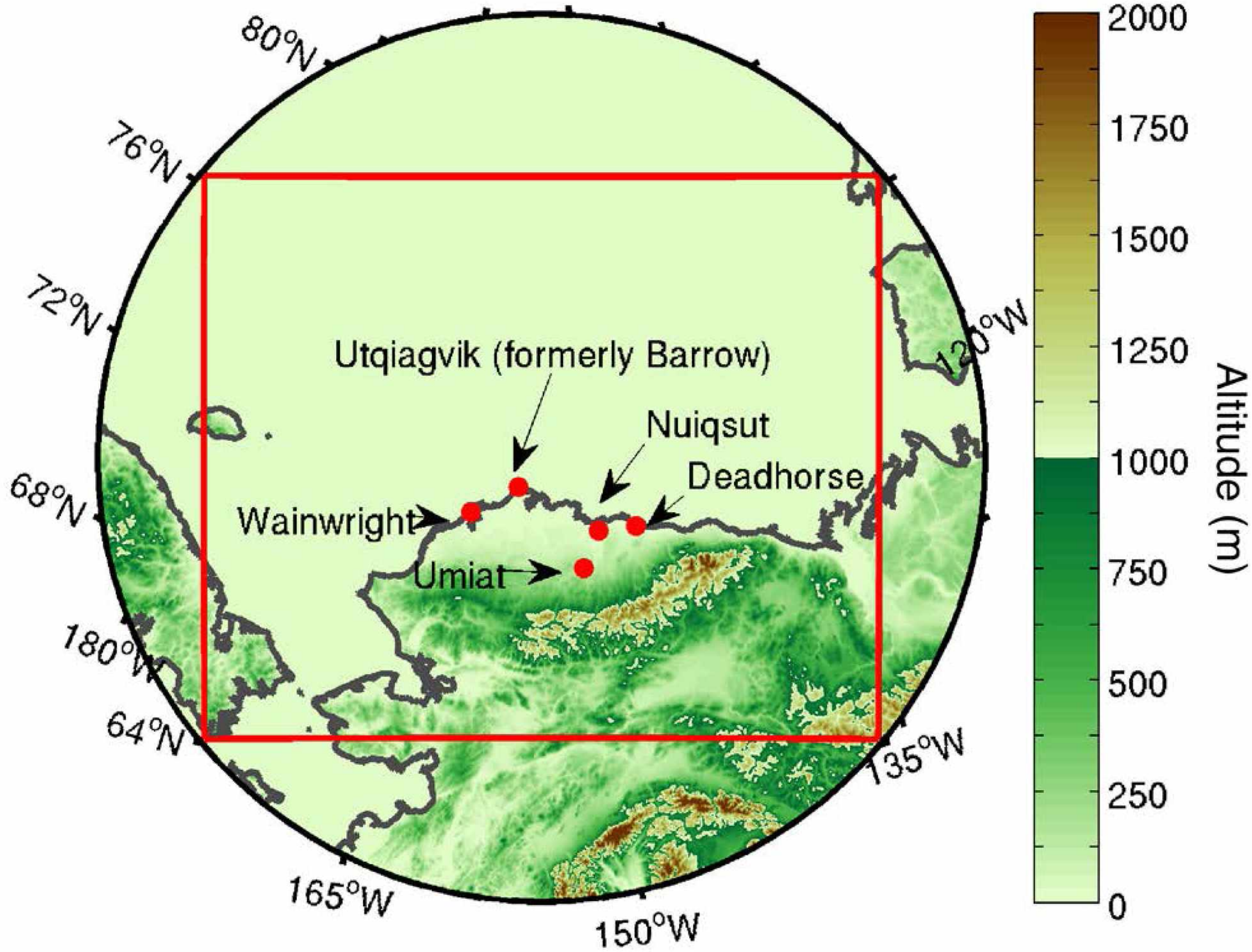

Figure 2.1. The WRF simulation domain (red box) with terrain heights (m). This downscaling product is specifically focused on the region of Arctic Coastal Plain and a small part of northern foothills of the Brooks Range with the domain enclosed by the grey line.

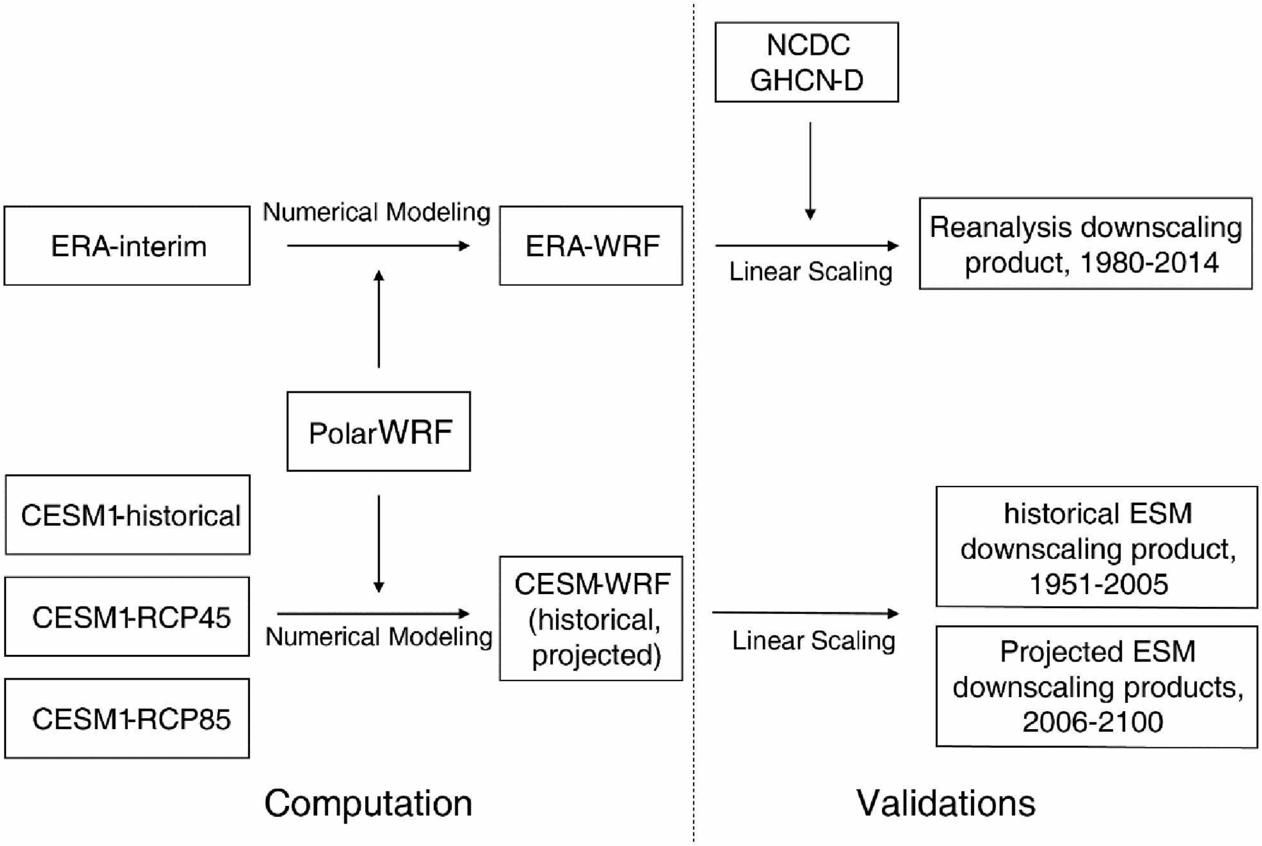

Figure 2.2. The flowchart indicating the development process of the downscaling products.

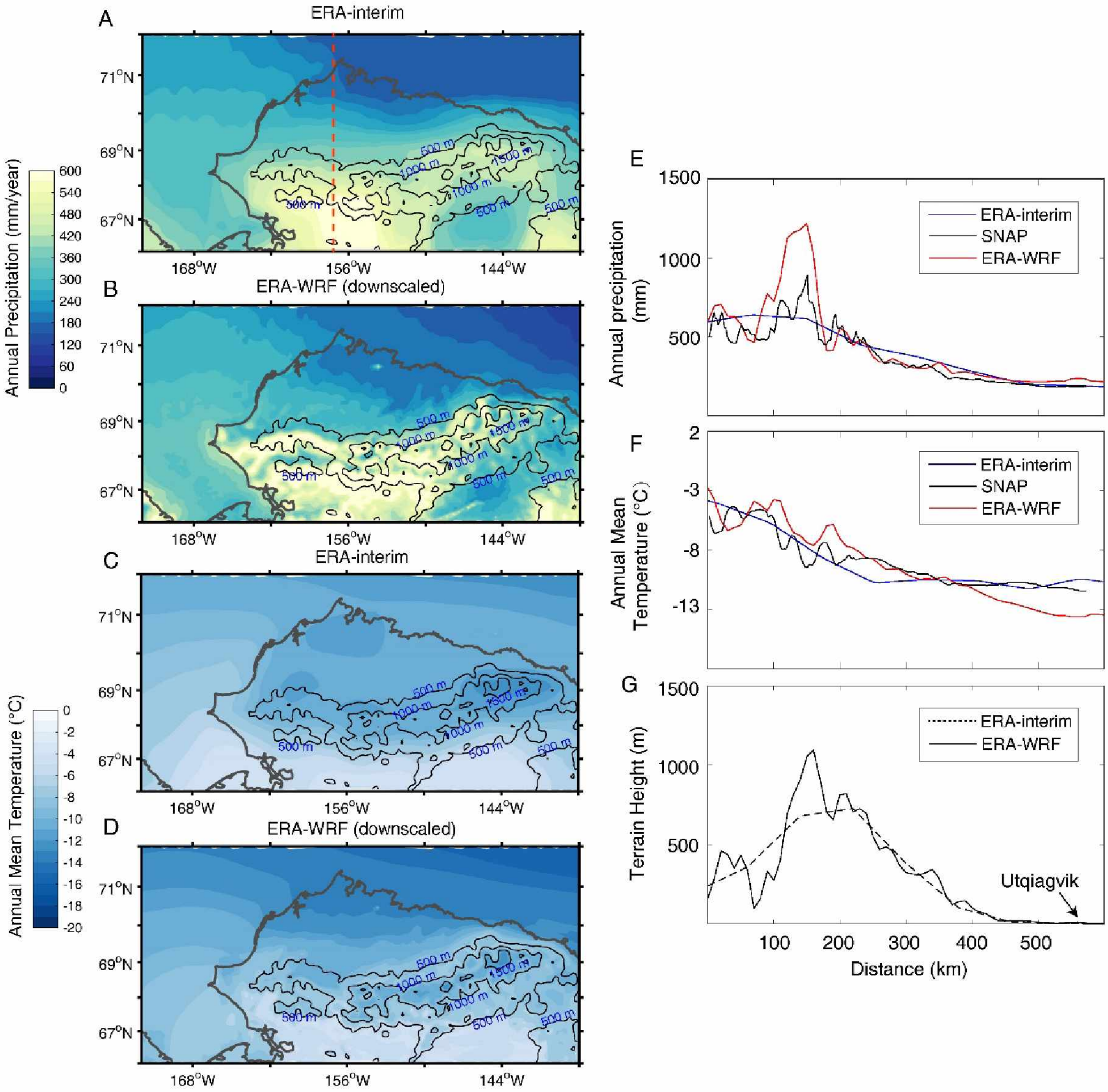

Figure 2.3. Original (ERA-interim) and downscaled (ERA-WRF) climatology 1980-2015 and elevation contour lines (black lines). Coarse resolution ERA-interim annual precipitation (a) and air temperature (c) compared to downscaled results from the ERA-WRF approach (b, d). Elevation contour lines in all figures are made from terrain height data in WRF. The annual precipitation (e) and mean temperature (f) distributions on the cross section (red dashed line in a) from ERA-interim (blue solid lines), SNAP (black solid lines), and ERA-WRF (red solid lines) show how a more detailed topography affects the precipitation and temperature distributions.

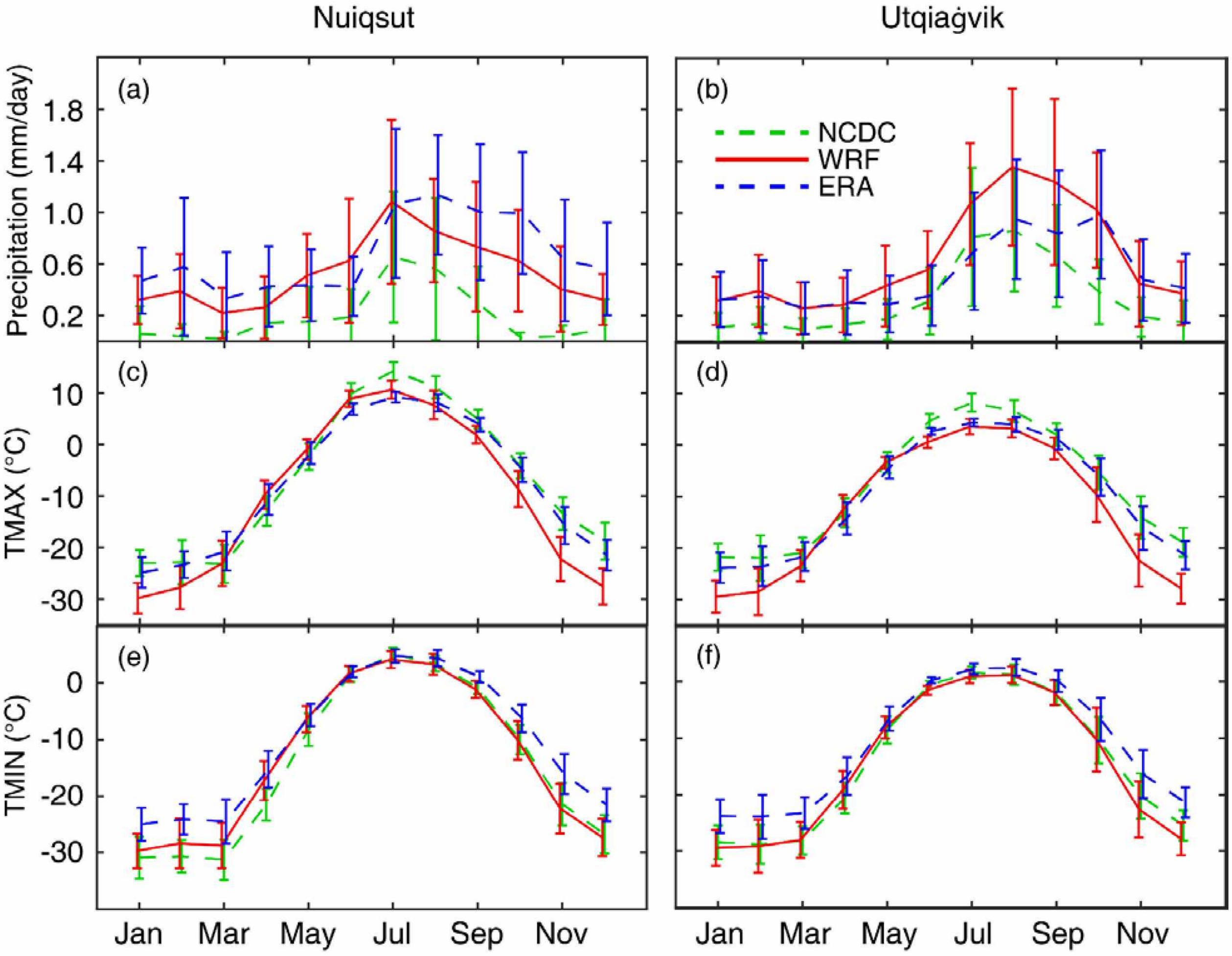

Figure 2.4. Monthly climatology comparisons between the NCDC GHCN-D observations (green dashed lines), downscaled ERA-WRF output (red solid lines), and ERA-interim reanalysis data (blue dashed lines) of average precipitation (mm/day), maximum and minimum air temperature (TMAX and TMIN, °C) for each month at the coastal towns of Nuiqsut (a, c, e) and Barrow (b, d, f). Average annual precipitation for these two stations is larger in the ERA-interim (215.4 mm) and the downscaled ERA-WRF (212.5 mm) than conventional observations (94.8 mm).

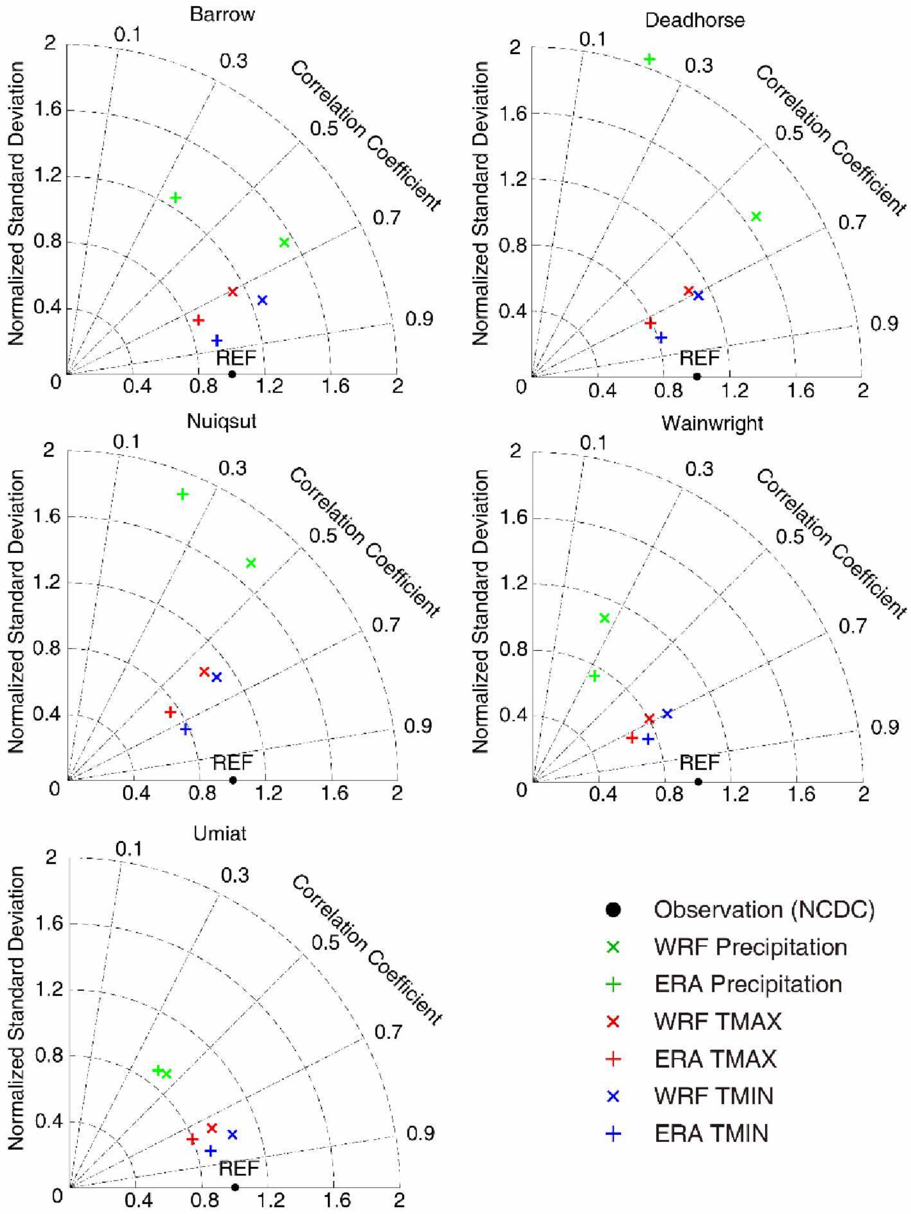

Figure 2.5. Taylor diagram with correlation coefficients and normalized standard deviations of daily precipitation (green), daily maximum temperature (TMAX, red), and daily minimum temperature (TMIN, blue) in ERA-WRF (WRF) and ERA-interim (ERA), compared to NCDC GHCN-D observations (black reference dot). The annual cycles of each variable have been removed before calculating the correlation coefficients and standard deviations.

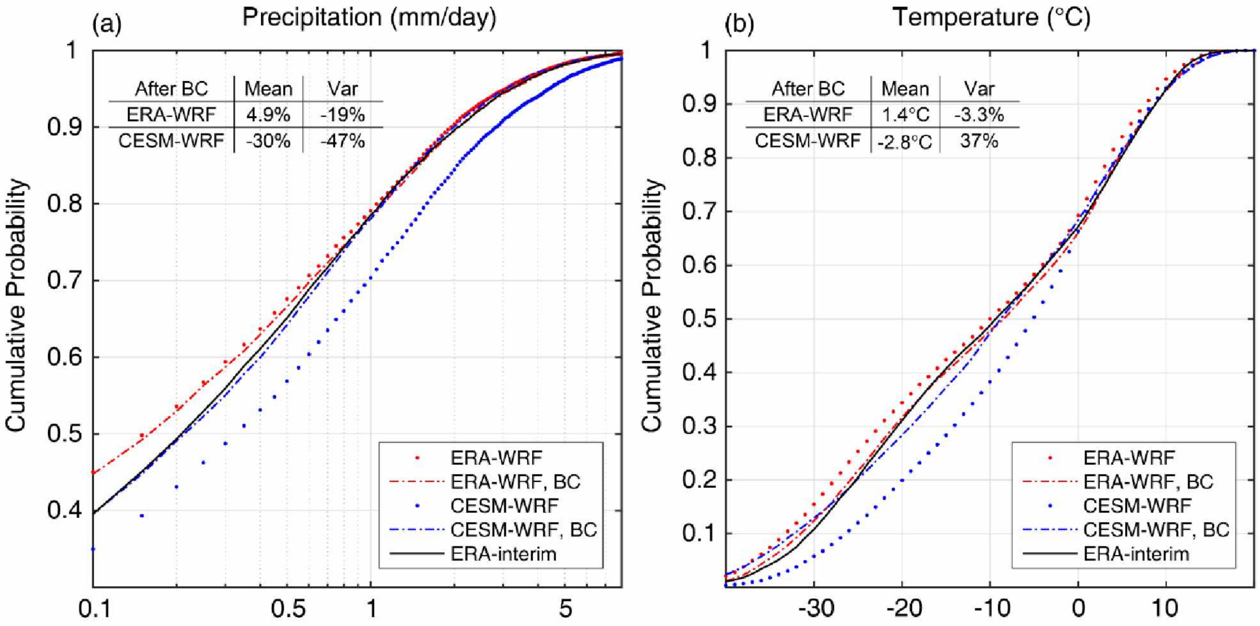

Figure 2.6. The comparisons of cumulative probabilities of (a) daily precipitation (mm/day) and (b) air temperature (°C) over coastal and foothill domain from the downscaled ERA-WRF (red dots), bias-corrected downscaled ERA-WRF (red dash-dot lines), downscaled CESM-WRF historical product (blue dots), and bias-corrected downscaled CESM-WRF historical product (blue dash-dot lines) to the reference of the original ERA-interim (black solid lines). The mean value and variance changes after bias corrections are in percentage, except for mean air temperature that shows absolute changes in °C. Linear scaling corrects biases more effectively in precipitation than in air temperature, and more in CESM-WRF compared to ERA-WRF.

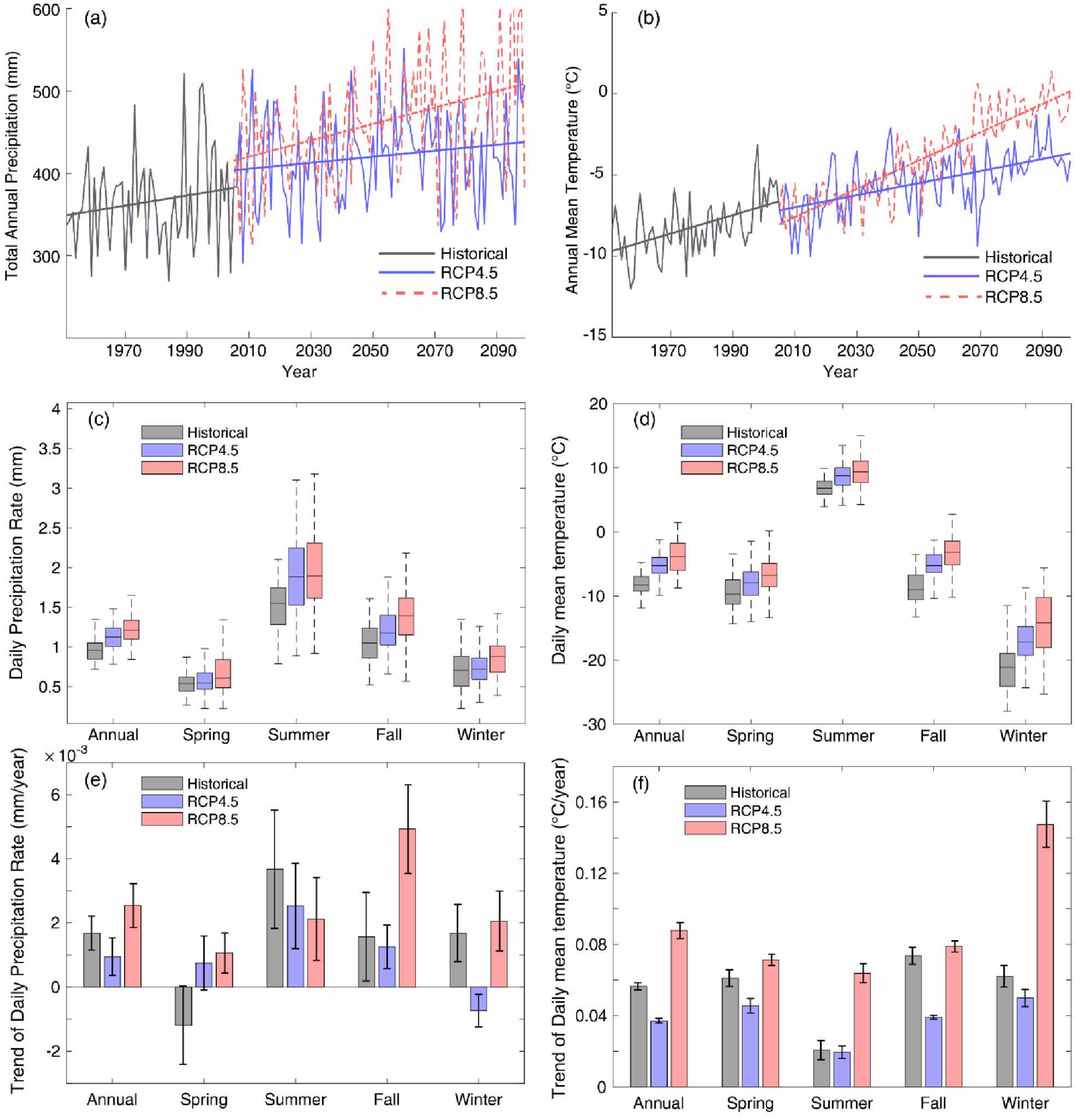

Figure 2.7. The time series of (a) total annual precipitation and (b) annual mean temperature in the in the historical (grey), RCP4.5 (blue), and RCP8.5 (red) downscaling products; The box plots of the annual and seasonal (c) daily precipitation rate (mm) and (d) daily mean temperature (°C) in the three downscaling products; The annual and seasonal trends of (e) daily precipitation rate (mm/year) and (f) daily mean temperature (°C/year) in the three downscaling products.

References

Alexeev, V. A., P. L. Langen, and J. R. Bates, 2005: Polar amplification of surface warming on an aquaplanet in "ghost forcing" experiments without sea ice feedbacks. *Climate Dynamics*, **24,** 655-666.

Alexeev, V. A., C. D. Arp, B. M. Jones, and L. Cai, 2016: Arctic sea ice decline contributes to thinning lake ice trend in northern Alaska. *Environmental Research Letters*, **11,** 074022.

Arp, C. D., B. M. Jones, Z. Lu, and M. S. Whitman, 2012: Shifting balance of thermokarst lake ice regimes across the Arctic Coastal Plain of northern Alaska. *Geophysical Research Letters*, **39**.

Arp, C. D., B. M. Jones, A. K. Liljedahl, K. M. Hinkel, and J. A. Welker. 2015: Depth, ice thickness, and ice-out timing cause divergent hydrologic responses among Arctic lakes. *Water Resource Research,* **51**, 9379-9401.

Bhatt, U. S., and Coauthors, 2008: The atmospheric response to realistic reduced summer Arctic sea ice anomalies. *Arctic sea ice decline: Observations, projections, mechanisms, and implications*, 91-110.

Bieniek, P. A., U. S. Bhatt, J. E. Walsh, T. S. Rupp, J. Zhang, J. R. Krieger, and R. Lader, 2016: Dynamical Downscaling of ERA-Interim Temperature and Precipitation for Alaska. *Journal of Applied Meteorology and Climatology*, **55,** 635-654.

Bintanja, R., and E. Van der Linden, 2013: The changing seasonal climate in the Arctic. *Scientific reports*, **3**.

Black, R. F., 1954: Precipitation at Barrow, Alaska, greater than recorded. *Eos, Transactions American Geophysical Union*, **35,** 203-207.

Bogdanova, E., V. Golubev, B. Ilyin, and I. Dragomilova, 2002: A new model for bias correction of precipitation measurements, and its application to polar regions of Russia. *Russian Meteorol. Hydrol*, **10,** 68-94.

Brown, L. C., and C. R. Duguay, 2010: The response and role of ice cover in lake-climate interactions. *Progress in Physical Geography*, **34,** 671-704.

Bruyère, C. L., J. M. Done, G. J. Holland, and S. Fredrick, 2014: Bias corrections of global models for regional climate simulations of high-impact weather. *Climate Dynamics*, **43,** 1847-1856.

Bullock Jr, O. R., K. Alapaty, J. A. Herwehe, M. S. Mallard, T. L. Otte, R. C. Gilliam, and C. G. Nolte, 2014: An observation-based investigation of nudging in WRF for downscaling surface climate information to 12-km grid spacing. *Journal of Applied Meteorology and Climatology*, **53,** 20-33.

Cassano, J. J., J. E. Box, D. H. Bromwich, L. Li, and K. Steffen, 2001: Evaluation of Polar MM5 simulations of Greenland's atmospheric circulation. *Journal of Geophysical Research: Atmospheres (1984–2012)*, **106,** 33867-33889.

Chapin III, F. S., R. L. Jefferies, J. F. Reynolds, G. R. Shaver, J. Svoboda, and E. W. Chu, 2012: *Arctic ecosystems in a changing climate: an ecophysiological perspective.* Academic Press.

Collins, M., and Coauthors, 2013: Climate change 2013: the physical science basis. Contribution of Working Group I to the Fifth Assessment Report of the Intergovernmental Panel on Climate Change. *Long-term Clim. Chang. Proj. Commitments Irreversibility, Cambridge Univ. Press. Cambridge, UK, New York.*

Dai, A., K. E. Trenberth, and T. R. Karl, 1999: Effects of clouds, soil moisture, precipitation, and water vapor on diurnal temperature range. *Journal of Climate*, **12,** 2451-2473.

de Boer, G., W. Chapman, J. E. Kay, B. Medeiros, M. D. Shupe, S. Vavrus, and J. Walsh, 2012: A Characterization of the Present-Day Arctic Atmosphere in CCSM4. *Journal of Climate*, **25,** 2676-2695.

Dee, D. P., and Coauthors, 2011: The ERA-Interim reanalysis: configuration and performance of the data assimilation system. *Quarterly Journal of the Royal Meteorological Society*, **137,** 553-597.

Dee, D., J. Fasullo, D. Shea, J. Walsh, and N. Staff, 2015: The climate data guide: atmospheric reanalysis: overview & comparison tables.

Deser, C., R. Tomas, M. Alexander, and D. Lawrence, 2010: The seasonal atmospheric response to projected Arctic sea ice loss in the late twenty-first century. *Journal of Climate*, **23,** 333-351.

Dudhia, J., 1996: A multi-layer soil temperature model for MM5. *Preprints, The Sixth PSU/NCAR mesoscale model users' workshop*, 22-24.

Fujita, T., D. J. Stensrud, and D. C. Dowell, 2007: Surface data assimilation using an ensemble Kalman filter approach with initial condition and model physics uncertainties. *Monthly weather review*, **135,** 1846-1868.

Glisan, J. M., W. J. Gutowski Jr, J. J. Cassano, and M. E. Higgins, 2013: Effects of spectral nudging in WRF on Arctic temperature and precipitation simulations. *Journal of Climate*, **26,** 3985-3999.

Groisman, P. Y., V. Koknaeva, T. Belokrylova, and T. Karl, 1991: Overcoming biases of precipitation measurement: A history of the USSR experience. *Bulletin of the American Meteorological Society*, **72,** 1725-1733.

Groisman, P. Y., and E. Y. Rankova, 2001: Precipitation trends over the Russian permafrost-free zone: removing the artifacts of pre-processing. *International Journal of Climatology*, **21,** 657-678.

Groisman, P. Y., R. W. Knight, T. R. Karl, D. R. Easterling, B. Sun, and J. H. Lawrimore, 2004: Contemporary Changes of the Hydrological Cycle over the Contiguous United States: Trends Derived from In Situ Observations. *Journal of Hydrometeorology*, **5,** 64-85.

Grosse, G., S. Goetz, A. D. McGuire, V. Romanovsky, E. , and E. Schuur, A. G. , 2016: Changing permafrost in a warming world and feedbacks to the Earth system. *Environmental Research Letters*, **11,** 040201.

Giorgi, F., C. Jones, and G. R. Asrar, 2009: Addressing climate information needs at the regional level: the CORDEX framework. *World Meteorological Organization (WMO) Bulletin*, **58,** 175.

Guemas, V., F. J. Doblas-Reyes, I. Andreu-Burillo, and M. Asif, 2013: Retrospective prediction of the global warming slowdown in the past decade. *Nature Climate Change*, **3,** 649-653.

Gutowski., W. J., and Coauthors, 2010: Regional Extreme Monthly Precipitation Simulated by NARCCAP RCMs. *Journal of Hydrometeorology*, **11,** 1373-1379.

Hanson, L. S., and R. Vogel, 2008: The probability distribution of daily rainfall in the United States. *Proc. World Environmental and Water Resources Congress*, 1-10.

Harmel, R., C. Richardson, C. Hanson, and G. Johnson, 2002: Evaluating the adequacy of simulating maximum and minimum daily air temperature with the normal distribution. *Journal of applied meteorology*, **41,** 744-753.

Hines, K. M., D. H. Bromwich, M. Barlage, and A. G. Slater, 2009: Arctic land simulations with Polar WRF. *Preprints, 10th Conf Polar Meteorology and Oceanography*, 17-21.

Hines, K. M., D. H. Bromwich, L.-S. Bai, M. Barlage, and A. G. Slater, 2011: Development and Testing of Polar WRF. Part III: Arctic Land*. *Journal of Climate*, **24,** 26-48.

Hinzman, L. D., and Coauthors, 2005: Evidence and Implications of Recent Climate Change in Northern Alaska and Other Arctic Regions. *Climatic Change*, **72,** 251-298.

Hong, S.-Y., and J. Dudhia, 2003: 17.3 Testing of a new nonlocal boundary layer vertical diffusion scheme in numerical weather prediction applications.

Hong, S.-Y., H.-M. H. Juang, and Q. Zhao, 1998: Implementation of prognostic cloud scheme for a regional spectral model. *Monthly weather review*, **126,** 2621-2639.

Jakobson, E., T. Vihma, T. Palo, L. Jakobson, H. Keernik, and J. Jaagus, 2012: Validation of atmospheric reanalyses over the central Arctic Ocean. *Geophysical Research Letters*, **39**.

Johannessen, O. M., and Coauthors, 2004: Arctic climate change: Observed and modelled temperature and sea-ice variability. *Tellus A*, **56,** 328-341.

Jones, B. M., and C. D. Arp, 2015: Observing a catastrophic thermokarst lake drainage in northern Alaska. *Permafrost and Periglacial Processes*.

Jones, B. M., G. Grosse, C. Arp, M. Jones, K. Walter Anthony, and V. Romanovsky, 2011: Modern thermokarst lake dynamics in the continuous permafrost zone, northern Seward Peninsula, Alaska. *Journal of Geophysical Research: Biogeosciences*, **116**.

Jorgenson, M. T., Y. L. Shur, and E. R. Pullman, 2006: Abrupt increase in permafrost degradation in Arctic Alaska. *Geophysical Research Letters*, **33**.

Kain, J. S., 2004: The Kain-Fritsch convective parameterization: an update. *Journal of Applied Meteorology*, **43,** 170-181.

Koenigk, T., A. Devasthale, and K.-G. Karlsson, 2014: Summer Arctic sea ice albedo in CMIP5 models. *Atmospheric Chemistry and Physics*, **14,** 1987-1998.

Lantz, T., and K. Turner, 2015: Changes in lake area in response to thermokarst processes and climate in Old Crow Flats, Yukon. *Journal of Geophysical Research: Biogeosciences*, **120,** 513-524.

Lantz, T. C., and S. V. Kokelj, 2008: Increasing rates of retrogressive thaw slump activity in the Mackenzie Delta region, NWT, Canada. *Geophysical Research Letters*, **35**.

Lenderink, G., A. Buishand, and W. v. Deursen, 2007: Estimates of future discharges of the river Rhine using two scenario methodologies: direct versus delta approach. *Hydrology and Earth System Sciences*, **11,** 1145-1159.

Liljedahl, A. K., L. D. Hinzman, D. L. Kane, W. C. Oechel, C. E. Tweedie, and D. Zona, 2017: Tundra water budget and implications of precipitation underestimation. Water Resources Research, doi: 10.1002/2016WR020001.

Liljedahl, A. K., and Coauthors, 2016: Pan-Arctic ice-wedge degradation in warming permafrost and its influence on tundra hydrology. Nature Geoscience, doi:10.1038/ngeo2674.

Lindsay, R., M. Wensnahan, A. Schweiger, and J. Zhang, 2014: Evaluation of seven different atmospheric reanalysis products in the Arctic. *Journal of Climate*, **27,** 2588-2606.

Liston, G. E., and M. Sturm, 2002: Winter precipitation patterns in arctic Alaska determined from a blowing-snow model and snow-depth observations. *Journal of Hydrometeorology*, **3,** 646-659.

Liu, F., J. R. Krieger, and J. Zhang, 2014: Toward producing the Chukchi–Beaufort High-Resolution Atmospheric Reanalysis (CBHAR) via the WRFDA data assimilation system. *Monthly Weather Review*, **142,** 788-805.

Liu, P., A. Tsimpidi, Y. Hu, B. Stone, A. Russell, and A. Nenes, 2012: Differences between downscaling with spectral and grid nudging using WRF. *Atmospheric Chemistry and Physics*, **12,** 3601-3610.

Lorenc, A. C., and F. Rawlins, 2005: Why does 4D-Var beat 3D-Var? *Quarterly Journal of the Royal Meteorological Society*, **131,** 3247-3257.

Maykut, G. A., and P. E. Church, 1973: Radiation Climate of Barrow Alaska, 1962–66. Journal of Applied Meteorology, **12**, 620-628.

Mearns, L. O., and Coauthors, 2013: Climate change projections of the North American Regional Climate Change Assessment Program (NARCCAP). *Climatic Change*, **120,** 965-975.

Meehl, G. A., and Coauthors, 2013: Climate change projections in CESM1 (CAM5) compared to CCSM4. *Journal of Climate*, **26,** 6287-6308.

Mlawer, E. J., S. J. Taubman, P. D. Brown, M. J. Iacono, and S. A. Clough, 1997: Radiative transfer for inhomogeneous atmospheres: RRTM, a validated correlated-k model for the longwave. *Journal of Geophysical Research: Atmospheres (1984–2012)*, **102,** 16663-16682.

Mortin, J., R. G. Graversen, and G. Svensson, 2013: Evaluation of pan-Arctic melt-freeze onset in CMIP5 climate models and reanalyses using surface observations. *Climate Dynamics*, **42,** 2239-2257.

Moss, R. H., and Coauthors, 2010: The next generation of scenarios for climate change research and assessment. *Nature*, **463,** 747-756.

Noilhan, J., and S. Planton, 1989: A simple parameterization of land surface processes for meteorological models. *Monthly Weather Review*, **117,** 536-549.

Plug, L., C. Walls, and B. Scott, 2008: Tundra lake changes from 1978 to 2001 on the Tuktoyaktuk Peninsula, western Canadian Arctic. *Geophysical Research Letters*, **35**.

Porter, D. F., J. J. Cassano, and M. C. Serreze, 2012: Local and large-scale atmospheric responses to reduced Arctic sea ice and ocean warming in the WRF model. *Journal of Geophysical Research*, **117**.

Post, E., and Coauthors, 2009: Ecological dynamics across the Arctic associated with recent climate change. *Science*, **325,** 1355-1358.

Przybylak, R., 2000: Diurnal temperature range in the Arctic and its relation to hemispheric and Arctic circulation patterns. *International Journal of Climatology*, **20,** 231-253.

Radu, R., M. Déqué, and S. Somot, 2008: Spectral nudging in a spectral regional climate model. *Tellus A*, **60,** 898-910.

Rasmussen, R., and Coauthors, 2012: How well are we measuring snow: The NOAA/FAA/NCAR winter precipitation test bed. *Bulletin of the American Meteorological Society*, **93,** 811-829.

Riahi, K., and Coauthors, 2011: RCP 8.5—A scenario of comparatively high greenhouse gas emissions. *Climatic Change*, **109,** 33-57.

Romanovsky, V. E., S. L. Smith, and H. H. Christiansen, 2010: Permafrost thermal state in the polar Northern Hemisphere during the international polar year 2007–2009: a synthesis. *Permafrost and Periglacial Processes*, **21,** 106-116.

Screen, J. A., I. Simmonds, C. Deser, and R. Tomas, 2013: The Atmospheric Response to Three Decades of Observed Arctic Sea Ice Loss. *Journal of Climate*, **26,** 1230-1248.

Serreze, M. C., and J. A. Francis, 2006: The Arctic Amplification Debate. *Climatic Change*, **76,** 241-264.

Serreze, M. C., M. M. Holland, and J. Stroeve, 2007: Perspectives on the Arctic's shrinking sea-ice cover. *Science*, **315,** 1533-1536.

Shulski, M., and G. Wendler, 2007: *The climate of Alaska.* University of Alaska Press.

Skamarock, W. C., and Coauthors, 2008: A description of the advanced research WRF version 3.

Smith, S., and Coauthors, 2010: Thermal state of permafrost in North America: a contribution to the international polar year. *Permafrost and Periglacial Processes*, **21,** 117-135.

SNAP, 2017: *Scenarios Network for Alaska Planning, University of Alaska.* Retrieved 18 November 2017 from http://snap.uaf.edu.

Stroeve, J. C., M. M. Holland, W. Meier, T. Scambos, and M. Serreze, 2007: Arctic sea ice decline: Faster than forecast. *Geophysical research letters*, **34**.

Stroeve, J. C., V. Kattsov, A. Barrett, M. Serreze, T. Pavlova, M. Holland, and W. N. Meier, 2012: Trends in Arctic sea ice extent from CMIP5, CMIP3 and observations. *Geophysical Research Letters*, **39**.

Stafford, J., G. Wendler, and J. Curtis, 2000: Temperature and precipitation of Alaska: 50-year trend analysis. *Theoretical and Applied Climatology*, **67,** 33-44.

Tape, K., M. Sturm, and C. Racine, 2006: The evidence for shrub expansion in northern Alaska and the Pan-Arctic. *Global Change Biology*, **12,** 686-702.

Taylor, K. E., R. J. Stouffer, and G. A. Meehl, 2012: An overview of CMIP5 and the experiment design. *Bulletin of the American Meteorological Society*, **93,** 485-498.

Teutschbein, C., and J. Seibert, 2012: Bias correction of regional climate model simulations for hydrological climate-change impact studies: Review and evaluation of different methods. *Journal of Hydrology*, **456-457,** 12-29.

Thomson, A. M., and Coauthors, 2011: RCP4. 5: a pathway for stabilization of radiative forcing by 2100. *Climatic Change*, **109,** 77-94.

Vertenstein, M., T. Craig, A. Middleton, D. Feddema, and C. Fischer, 2011: CESM1. 0.4 User's Guide. NCAR. URL http://www.cesm.ucar.edu/models/cesm1.0/cesm.

Vose, R., M. Menne, I. Durre, and B. Gleason, 2007: GHCN daily: A global dataset for climate extremes research. *AGU Spring Meeting Abstracts*, 08.

Walston, J., G. Gibson, and J. Walsh, 2014: Performance assessment of the Community Climate System Model over the Bering Sea. *International Journal of Climatology*, **34,** 3953-3966.

Wang, M., and J. E. Overland, 2012: A sea ice free summer Arctic within 30 years: An update from CMIP5 models. *Geophysical Research Letters*, **39**.

Wehner, M. F., 2013: Very extreme seasonal precipitation in the NARCCAP ensemble: model performance and projections. *Climate Dynamics*, **40,** 59-80.

Whitaker, J. S., G. P. Compo, and J.-N. Thépaut, 2009: A comparison of variational and ensemble-based data assimilation systems for reanalysis of sparse observations. *Monthly Weather Review*, **137,** 1991-1999.

Wilby, R. L., and T. Wigley, 1997: Downscaling general circulation model output: a review of methods and limitations. Progress in physical geography, **21**, 530-548.

Wilson, A. B., D. H. Bromwich, and K. M. Hines, 2011: Evaluation of Polar WRF forecasts on the Arctic System Reanalysis domain: Surface and upper air analysis. *Journal of Geophysical Research*, **116**.

Wilson, A. B., D. H. Bromwich, and K. M. Hines, 2012: Evaluation of Polar WRF forecasts on the Arctic System Reanalysis Domain: 2. Atmospheric hydrologic cycle. *Journal of Geophysical Research*, **117**.

Winton, M., 2006: Amplified Arctic climate change: What does surface albedo feedback have to do with it? *Geophysical Research Letters*, **33**.

Zhang, J., F. Liu, W. Tao, J. Krieger, M. Shulski, and X. Zhang, 2016: Mesoscale Climatology and Variation of Surface Winds over the Chukchi–Beaufort Coastal Areas. *Journal of Climate*, **29,** 2721-2739.

Appendix A

A.1 More details on ERA-WRF evaluation

Monthly mean precipitation, maximum temperature (TMAX), and minimum temperature (TMIN) in the observation (NCDC GHCN-D), the reanalysis dataset (ERA-interim), and the model output (ERA-WRF) in Table A-1 gives the completed version of ERA-WRF output evaluation at stations. As the result, Deadhorse, Wainwright, and Umiat, the three sites that aren't mentioned in the paper, all hold the similar dry biases monthly compared to ERA-interim on precipitation like Nuiqsut, which are opposite to Utqiaġvik's wet bias. They also have doubled precipitation annually compared to NCDC GHCN-D data as observed precipitation amounts in winter are close to zero. Among these three sites, Umiat has the driest bias annually (37.5 mm), as it is located in the North foothill of the Brooks Range, affecting the most by the enhanced topographic blocking of ERA-WRF's topography. Wainwright is located on the northwest coast of Alaska, in which the precipitation is affected least by the Brooks Range topography. Wainwright, therefore, has the least dry bias annually (4.8 mm), with almost the same amount of ERA-WRF modeled precipitation to ERA-interim precipitation. Deadhorse is close to Nuiqsut so that the precipitation bias at Deadhorse is similar to that at Nuiqsut.

For TMAX and TMIN, TMAX at Deadhorse and Wainwright also show cold biases from July to March compared to both ERA-interim and the observation. The most biases are in December to January, up to 10 °C colder than observation data and 6 °C colder than ERA-interim data. Umiat presents a slight warm bias (< 3 °C) in the months of January to June compared to ERA-interim does, while close magnitudes of cold biases are in July to December.

TMIN biases hold the similar features to TMAX biases. Deadhorse and Wainwright exhibit the similar cold biases to ERA-interim and warm biases to observation as Nuiqsut does. Umiat, on the other hand, produces a slight warm bias (< 3 °C) from January to June, just like what is in TMAX bias comparison. In summary, for the stations that are not included in the paper, Deadhorse illustrates biases very similar to Nuiqsut, due to their small distance to each other. Wainwright shows similar temperature biases to Deadhorse and Nuiqsut, but ERA-WRF precipitation in Wainwright is less biased compared to ERA-interim, as Wainwright is less affected by the enhanced Brooks Range topography in WRF. On the other hand, precipitation and temperature biases in Umiat differ from all other sites compared in this study, as it is in the northern foothill of the Brooks Range, in which has the most precipitation and temperature changes after they are downscaled by WRF model.

A.2 Additional bias correction information

In the published version of downscaling products, variables of snow water equivalent, dew point temperature, wind speeds (zonal and meridional), surface air pressure, downward shortwave/longwave radiation fluxes at surface are also included, and some of them are bias corrected. Among these variables, snow water equivalent is bias corrected using linear scaling formulas for precipitation, since it's basically another form of precipitation, and its daily time series also obeys the two-parameter gamma distribution. Dewpoint temperature, wind speeds, and surface pressure are bias-corrected using the formulas for temperature, as their time series obey the normal distribution. WRF's high-resolution grid spacing, as well as its microphysics and cumulus parameterizations, intend to resolve different cloud cover variations from ERA-interim's. In this way, the downward radiation fluxes are not bias corrected, as bias correction to radiation fluxes would only bring more uncertainties to the final products than useful climatic variables. To request other variables which are not in the list above or other special needs, please contact Lei Cai (lcai4@alaska.edu) or Vladimir Alexeev (valexeev@alaska.edu) for more information and help.

Table A-1. The monthly climatology comparisons at five stations of Utqiaġvik, Deadhorse, Nuiqsut, Umiat, and Wainwright on variables of daily precipitation, daily maximum temperature (TMAX) and daily minimum temperature (TMIN) in ERA-WRF output (WRF), NCDC GHCN-D data (NCDC), and ERA-interim reanalysis (ERA).

Precpitation(mm/day)

Month	Utqiaġvik			Deadhorse			Nuiqsut			Umiat			Wainwright		
	WRF	NCDC	ERA	WRF	NCDC	ERA	WRF	NCDC	ERA	WRF	NCDC	ERA	WRF	NCDC	ERA
Jan	0.32	0.11	0.32	0.41	0.04	0.51	0.33	0.06	0.48	0.33	0.31	0.33	0.46	0.02	0.53
Feb	0.39	0.14	0.35	0.43	0.02	0.5	0.41	0.05	0.6	0.31	0.29	0.36	0.46	0.06	0.57
Mar	0.26	0.09	0.26	0.22	0.01	0.31	0.23	0.01	0.38	0.29	0.19	0.32	0.23	0.02	0.25
Apr	0.28	0.14	0.3	0.27	0.1	0.45	0.27	0.14	0.44	0.25	0.19	0.31	0.38	0.1	0.48
May	0.43	0.18	0.29	0.5	0.16	0.48	0.5	0.15	0.45	0.31	0.07	0.36	0.63	0.14	0.49
Jun	0.56	0.32	0.35	0.55	0.38	0.5	0.59	0.2	0.43	0.85	0.57	1.08	0.65	0.44	0.58
Jul	1.07	0.82	0.7	1.14	0.76	1.51	1.12	0.66	1.1	0.95	0.63	1.49	1.33	0.88	1.14
Aug	1.36	0.85	0.94	0.94	0.69	1.35	0.84	0.56	1.11	1.4	0.87	1.76	1.34	0.87	1.52
Sep	1.24	0.66	0.83	0.79	0.42	1.12	0.74	0.28	1.02	1.02	0.28	1.13	1.15	0.56	1.05
Oct	1.02	0.39	0.98	0.86	0.17	1.02	0.64	0.03	1.01	0.67	0.59	0.73	1.01	0.21	1.1
Nov	0.45	0.19	0.4	0.5	0.06	0.67	0.43	0.04	0.64	0.26	0.26	0.034	0.7	0.09	0.66
Dec	0.37	0.15	0.41	0.34	0.06	0.5	0.32	0.1	0.57	0.34	0.25	0.32	0.45	0.04	0.6

TMAX (° C)

Month	Utqiaġvik			Deadhorse			Nuiqsut			Umiat			Wainwright		
	WRF	NCDC	ERA	WRF	NCDC	ERA	WRF	NCDC	ERA	WRF	NCDC	ERA	WRF	NCDC	ERA
Jan	-29.4	-21.7	-23.8	-28.1	-22.8	-24.3	-29.4	-22.7	-24.5	-28.2	-26.2	-28.1	-28.9	-20.3	-24.8
Feb	-28.5	-21.7	-23.5	-26.2	-22.2	-22.9	-27.4	-22.4	-23.1	-26.7	-24.2	-26.8	-27	-20.6	-24.0
Mar	-23.4	-20.8	-21.6	-23	-22.8	-20.5	-23.4	-22.7	-21.0	-20.1	-21	-21.4	-22.5	-20.5	-21.7
Apr	-12.5	-12.7	-14.2	-9.7	-12.2	-10.1	-10.1	-12.4	-11.1	-9.6	-10.9	-11.1	-11	-12.2	-12.6
May	-3.4	-3.1	-4.3	-1.5	-2.6	-1.0	-1.1	-2	-1.8	3.5	1.8	0.5	-2.4	-2.3	-2.8
Jun	0.6	5	2.7	6.8	8	8.1	8.9	10.3	6.8	12.3	15.5	11.4	4.8	7.9	5.7
Jul	3.6	8.3	4.4	8.7	12.3	10.1	10.6	14.2	9.1	1.2	18.7	15.1	7.9	11.2	8.6
Aug	3.2	6.5	4	6.8	9.7	8.6	7.6	10.9	8.1	9.6	13.4	11.1	5.7	9.2	7.6
Sep	0.6	2	1.1	2	4.3	4.3	1.8	4.8	3.8	1.7	4.7	3.7	1.3	4	3.7
Oct	-9.6	-5.3	-6.1	-7.6	-4.4	-4.8	-8.6	-4.1	-4.9	-12.1	-8.5	-9.0	-7.5	-3.3	-4.0
Nov	-22.3	-14	-16.1	-21.2	-13.8	-15.9	-22.3	-13.4	-15.9	-24.3	-21.2	-20.6	-20	-11.8	-14.5
Dec	-27.8	-18.8	-21.3	-26.3	-19	-21.12	-27.7	-19	-21.6	-27.8	-24.8	-25.5	-26.5	-17.2	-20.9

TMIN (°C)

Month	Utqiaġvik			Deadhorse			Nuiqsut			Umiat			Wainwright		
	WRF	NCDC	ERA	WRF	NCDC	ERA	WRF	NCDC	ERA	WRF	NCDC	ERA	WRF	NCDC	ERA
Jan	-29.5	-28.5	-23.9	-28.2	-30.1	-24.5	-29.4	-30.6	-24.8	-28.4	-34	-28.4	-29	-27.8	-25.0
Feb	-29.2	-28.7	-23.9	-27	-29.8	-23.9	-28.1	-30.4	-24.0	-28	-33.8	-28.9	-27.5	-28	-24.8
Mar	-28.1	-28	-23.3	-28.3	-30.5	-25.1	-29.2	-30.8	-25.0	-26.2	-32.2	-27.8	-27.7	-28.2	-25.2
Apr	-19.1	-20.1	-16.7	-16.8	-20.4	-15.6	-17.6	-20.9	-15.7	-18	-23.2	-18.5	-17.5	-20	-16.6
May	-8.1	-8.2	-6.6	-6.6	-8.3	-5.8	-6.5	-7.9	-5.8	-4.1	-8	-6.1	-6.9	-7.5	-6.0
Jun	-1.5	-0.4	0.24	0.8	1	2.7	1.6	1.7	1.9	4.5	3.22	4.3	0.5	0.6	1.8
Jul	0.9	1.6	2.2	3	4.1	5.4	4.1	4.9	4.6	7	5.7	7.9	3.4	3.5	4.9
Aug	1.2	1.2	2.4	2.7	2.8	4.4	3.2	3.3	4.3	4.3	2.4	5.1	2.7	3.1	4.5
Sep	-1.9	-1.9	0	-0.9	-1	0.8	-1.2	-0.9	1	-2.7	-3.7	-1.1	-0.93	-0.5	1.3
Oct	-10.2	-10.3	-6.7	-9.1	-10.1	-6.3	-10.1	-9.9	-6.2	-14.8	-16.8	-11.6	-8.5	-8.2	-5.3
Nov	-22.6	-20.2	-16.3	-21.3	-21.3	-16.3	-22.3	-21.4	-16.2	-24.7	-28.5	-21.3	-20.2	-18.4	-14.8
Dec	-27.9	-25.5	-21.4	-26.4	-26.3	-21.2	-27.7	-27	-21.8	-27.8	-32.6	-25.7	-26.7	-24.3	-21.2

Chapter 3. Modeling the impacts of projected sea ice decline on the low atmosphere and near-surface permafrost on the North Slope of Alaska[2]

Abstract

This model-based study assesses the response of the lower atmosphere and near-surface permafrost on the North Slope of Alaska to projections in sea ice decline. The Weather Research & Forecast model, with polar optimization (Polar WRF), was configured for the North Slope of Alaska and the adjacent Arctic Ocean and run for two decade-long control periods, the 1970s and the 2040s. Community Earth System (CESM) model output was used to drive the Polar WRF model. By swapping the sea ice coverage in the control cases, two polar WRF sensitivity experiments were designed to quantify the changes in the low atmosphere and near-surface permafrost in response to projected declines in sea ice extent. The strongest impacts of sea ice decline occur primarily during the late fall and early winter. These include, increases in surface air temperature, surface humidity, total cloud cover, and precipitation amount. Future impacts of sea ice decline are projected to become weaker over time in the late fall and early winter, while becoming more prominent in late spring and early summer. Projected sea ice decline also inhibits low-level cloud formation in summer as a result of destabilization of the boundary layer. Sensitivity experiments by polar WRF and Geophysical Institute Permafrost Lab (GIPL) model, respectively, suggest that sea ice decline explains approximately 20 % of both the atmospheric and permafrost warmings on a mean annual basis compared to the overall projected warming under the RCP4.5 scenario.

3.1 Introduction

Arctic sea ice extent (SIE) is declining (ref). SIE in September has been shrinking at more than 4% per decade rate since 1979 in the Arctic (Cavalieri and Parkinson, 2012). A record-breaking low SIE was observed in the September of 2012 for an area of 2.4 million km^2 (Parkinson

---

[2] Cai, L., V. A. Alexeev, C. D. Arp, B. M. Jones, V. E. Romanovsky 2018: Modeling study of impacts of projected sea ice decline on the local climate of the North Slope of Alaska, *International Journal of Climatology,* submitted.

and Comiso, 2013). Declines in SIE were also observed in all other months, though at lower rates than in September (data from National Snow and Ice Data Center, http://www.nsidc.org). As projected by global climate models in the most extreme radiative forcing scenario, the Arctic Ocean will become ice-free in September by the end of 2060s (Serreze et al., 2005; Stroeve et al., 2012; Collins et al., 2013). The larger open-water extent caused by declining sea ice lowers the surface albedo of the ocean and releases heat to the atmosphere, the effects of which are most pronounced in late fall and early winter (Barry et al., 1993; Alexander et al., 2004; Screen and Simmonds, 2010). The abundance of heat and moisture in the near-surface atmosphere favors low-level cloud formation (Francis and Hunter, 2007; Kay et al., 2009; Walsh et al., 2009; Liu et al., 2012), and in turn more precipitation in the form of snowfall (Higgins and Cassano, 2009; Liu et al., 2012; Handorf et al., 2015).

Arctic tundra and thousands of arctic lakes jointly compose the land cover on the North Slope of Alaska, with continuous permafrost underneath (Zhang et al., 1997; Smith et al., 2007; Kittel et al., 2010; Grosse et al. 2013), all of which are sensitive to regional climate change and sea ice decline (Cohen 1994; Serreze et al., 2009; Bhatt et al., 2014; Wendler et al., 2014). Observed, rapid sea ice retreat in the summer of 2007 may also relate to the large Anaktuvuk River tundra fire on the North Slope of Alaska (Jones et al., 2009; Hu et al., 2010), facilitated by other factors e.g., large-scale atmospheric circulation in forming precipitation/temperature regimes (Alexeev et al, 2015). In winter, reduced SIE enhances snowfall that inhibits arctic lake ice cover from thickening (Alexeev et al. 2016), resulting in enhanced sub-lake permafrost thaw (Arp et al., 2016). Sea ice decline is also projected to warm near-surface permafrost (Lawrence et al., 2008).

Observed evidence of sea ice decline impacts are embedded in overall climate change impacts occur in the Arctic. This prompted the question about the proportion of climate change solely driven by sea ice decline compared to global-scale greenhouse gas forcing. Global Climate Models (GCMs) have been commonly utilized to study impacts of sea ice decline (Lawrence et al., 2008; Higgins and Cassano, 2009; Stroeve et al., 2012; Screen et al., 2013). Besides tracking the heat and moisture fluxes released from the open ocean, GCMs can also simulate atmospheric circulation changes due to sea ice decline. To the east of Greenland, Sea Level Pressure (SLP) response to the reduced sea ice resembles the negative North Atlantic Oscillation (NAO) pattern, presented in the Community Climate Model (CCM 3.6, Alexander et al., 2004), and Community Climate System Model version 3 (CCSM3) (Deser et al., 2010). With regard to the 2007 SIE, a reinforced Arctic Dipole (AD) anomaly was modeled as the atmospheric circulation response by the ECHAM5 model (Blüthgen et al., 2012).

Regional Climate Models (RCMs) have certain advantages in studying responses to sea ice decline not only due to their fine spatial resolutions, but also due to their modeling framework. The synoptic background in the atmosphere in RCMs is controlled by the lateral boundary condition, if the model domain is small enough, while the near-surface characteristics are determined to a large extent by the surface boundary condition. Such separation between impacts of the boundary conditions in RCMs can be used to assess the atmospheric sensitivity to changing one type of boundary condition while keeping the other fixed (e.g. the absence of- or modified sea ice cover). The Weather Research and Forecast (WRF) model, a commonly used RCM, has been employed in a number of studies for such sensitivity experiments by keeping the atmospheric background unchanged while replacing the surface boundary conditions with 2007 sea ice cover, thus allowing for the tracking of the atmospheric response to such a low sea ice extent (Strey et al., 2010; Porter et al., 2012).

In this paper, we explore how sea ice decline impacts the lower atmosphere and temperature regime of near-surface permafrost on the North Slope of Alaska by conducting sensitivity experiments. We hypothesize that sea ice decline impacts both the atmosphere and the permafrost on seasonal time-scales. The sensitivity experiments design consists of developing two control climates (past: 1970-1980 and future: 2040-2050) and then swapping the sea ice between the two decades. The lateral boundary forcing is held constant in sensitivity runs for both decades in order to quantify the response to the same sea ice decline under different atmospheric backgrounds. We then import the atmospheric temperature response to sea ice into a permafrost model to assess the impact of sea ice decline on permafrost temperature regimes.

3.2 Tools and Experimental design

3.2.1 Tools for modeling regional climate and permafrost thermal regime

We employ the Polar Weather Research & Forecast (Polar WRF; version 3.5.1) model, a flexible, state-of-the-art regional atmospheric modeling system in this study (Skamarock et al., 2008). Compared with the version of WRF that was used in previous studies (Strey et al., 2010; Porter et al., 2012), the newer version of WRF (3.5.1 vs. 3.0.1 and 3.2.0) includes updates for high-latitude modeling with snow/ice cover at surface. More details about the updates are documented here: http://www2.mmm.ucar.edu/wrf/users/wrfv3.5/updates-3.5.1.html. An add-on called Polar WRF, which is optimized for polar processes, has been maintained by the Polar Meteorology Group of the Byrd Polar and Climate Research Center at Ohio State University for major versions of WRF (3.x.1). Polar WRF optimizes physics schemes and land surface parameters for both the land and ocean in polar regions (Hines et al., 2009; Hines et al., 2011; Wilson et al., 2011 and 2012). More importantly to our study, polar WRF specifies sea ice albedo to imitate more realistic behavior of sea ice in the Arctic Ocean by parameterizing gaps and leads (Hines et al., 2015). The optimizations above helps reproduce more reasonable sea-air energy exchange, as the prerequisite for more accurate temperature and humidity regimes (Cassano et al., 2011).

The Community Earth System Model (CESM, version 1.0) is a member of the Coupled Model Intercomparison Project Phase 5 (CMIP5) that assembles the latest generation of earth system models to project climate change and its impacts in multiple radiative forcing scenarios (Taylor et al., 2012). We utilize CESM output under the default configuration to drive Polar WRF, in which the Community Atmosphere Model 4 (CAM4) simulates the atmospheric component (http://www.cesm.ucar.edu/models/cesm1.0/config_conventions_cesm.html). The CESM output in the 21st century is projected using the Representative Concentration Pathway 4.5 (RCP4.5) scenario. CESM output is obtained in the WRF intermediate file format from NCAR & UCAR Research Data Archive (ds 316.0, Bruyere et al., 2015). Concatenating the SIE from the historical product and the RCP4.5 projection shows that the CESM-modeled SIE declines most rapidly in the period spanning from the 1970s to the 2040s, in both September and March (Figure 3.1a). Sea ice decline is negligible before the 1970s, while it slows down after the 2040s. Within this 70-year period, SIE declines at a generally uniform rate of approximately 4.5×10^5 km^2/decade in September, while 2×10^5 km^2/decade in March (Figure 3.1b).

Soil in WRF (parameterized by Noah Land Surface scheme) is represented by only a 1-meter deep layer, which is not enough for a proper representation of permafrost on the North Slope of Alaska. Therefore, we alternatively employed the Geophysical Institute Permafrost Laboratory model (GIPL, version 2.0). Compared to its earlier version that only analytically analyzes the mean annual ground temperature and active layer thickness (GIPL1.0, Sazonova and Romanovsky, 2003), GIPL2.0 numerically resolves heat exchanges between soil layers with phase changes (Marchenko et al., 2008). In this study, we employ the one-dimensional version of GIPL2.0, forced by the spatially averaged air temperature on the North Slope of Alaska, as exploring the detailed spatial distribution of permafrost response is out of our scope. Such simplification suffices for the purpose of the paper — to estimate the order of magnitude contribution of declining SIE on permafrost warming.

3.2.2 Initialization of Polar WRF sensitivity experiment

The idea of conducting WRF sensitivity experiments is to compare the near-surface atmospheric responses to prescribed sea ice extent, while keeping the atmospheric background unchanged. As mentioned, the CESM-modeled SIE shrinks most rapidly and uniformly from the 1970s to the 2040s, therefore we select the first and the last 11 years of this period for the Polar WRF runs. The 11-year length of WRF simulation cases is a compromise between the high computational cost and the need to average out (to an extent) inter-annual SIE variability.

The simulation domain has 119×99 grid points with a 20 km grid spacing, covering most of the Chukchi Sea and the Beaufort Sea, centered on the North Slope of Alaska (Figure 3.2). Vertically, there are 31 atmospheric layers and 4 soil layers, and the model output variables consist of 3-hourly data. The combination of parameterization schemes has been proven to perform well in long-term simulations over Arctic Alaska (Cai et al., 2018). Polar WRF single-moment, 5-class scheme parameterizes microphysical processes (Hong et al., 1998), and Kain-Fritsch scheme is for convective processes in the simulation (Kain, 2004). The Rapid Radiation Transfer Model (Mlawer et al., 1997) and Dudhia scheme (Dudhia, 1996) are responsible for longwave and shortwave radiation parameterizations, respectively. The Noah land surface scheme (Noilhan and Planton, 1989) parameterizes land surface processes, and the Yonsei University scheme (Hong and Dudhia, 2003) parameterizes planetary boundary layer dynamics.

Two control cases (1970s_HS and 2040s_LS) were run for the periods of 1970-1980 and 2040-2050, respectively. Simulations start on July 1st of the first year (1970 and 2040). The first six months (July 1st to December 31st of 1970 and 2040) work as the spin-up period, and are excluded from any further analyses. We do not perform any nudging or bias corrections of the output fields in this study in order to keep model fields dynamically consistent. Also, this is a sensitivity study, therefore base (or control) climates do not have to be adjusted precisely to the observed, because we analyze only the anomalies. We refer the term “1970s” for the period of 1971-1980, and “2040s” for 2041-2050 for the sake of simplicity. The SIEs differ substantially within the simulation domain between these two periods, especially in summer and fall (Figure 3.3). The annual maximum SIE that occurs in March is about 1×10^5 km^2 smaller in 2040s_HS than in 1970s_HS, implying that some oceanic regions that are seasonally covered by sea ice in the 1970s become ice-free all year around in the 2040s. Correspondingly, the Sea Surface Temperature (SST) is 0-1.8 °C warmer in 2040s_LS than that in 1970s_HS within the study domain.

The surface boundary condition for sensitivity cases are prescribed by swapping the SIE fields between the control cases. We run the 1970s with the 2040s sea ice coverage (1970s_LS), and the 2040s with the 1970s sea ice coverage (2040s_HS) (Table 3.1). The SST is adjusted following the swapped sea ice extents in order to avoid unrealistic physics in the surface conditions that otherwise makes simulations crash. If a grid point has both sea ice coverage and SST higher than 271.35 K, the SST is adjusted to 271.35 K (the maximum SST for the existence of sea ice in Polar WRF). Expectedly, only the 2040s_HS needed such an adjustment. Keeping SST almost unchanged minimizes the impact on the low-level atmosphere not associated with modifications of sea ice presence, thus better isolating the effects of sea ice decline (Screen et al., 2013). It may also, however, impose overly-cold water bodies that may result in cooling of the lower atmosphere. More details of this SST adjustment are discussed later.

3.2.3 Initialization of GIPL sensitivity experiment

Five GIPL experiment cases are divided into three categories: no warming, sea ice warming, and RCP warming (Table 3.1). The surface air temperature is averaged for all grid points on the North Slope of Alaska to construct the 1D time-dependent GIPL forcing. All cases are 130 years long, among which the RCP warming cases are forced by daily air temperature in CESM RCP products from 1971 to 2100. The no warming forcing is made by duplicating and concatenating the 1970s CESM historical daily temperature climatology for 130 times for a 130-year long daily air temperature forcing. The sea ice warming forcing is made by adding the averaged WRF-modeled air temperature response to sea ice decline to the no warming forcing.

The calculation of the averaged WRF-modeled air temperature response to SIE decline is accomplished by averaging responses to sea ice in the cold and warm climates (sum of the differences 1970s_LS - 1970_HS and 2040s_LS - 2040s_HS divided by 2). This averaging is done in order to minimize the impact of asymmetry in air temperature response to sea ice decline in cold and warm climates, the details of which are discussed later in the text.

The 130-year long forcing for RCP warming cases are made by concatenating air temperature time series in the CESM historical (1971-2005) and RCP (2006-2100) products. Like the forcing of RCP4.5 warming case that has the same radiative forcing scenario as the polar WRF forcing has, the forcings of RCP2.6 and RCP8.5 warming cases are similarly made from the CESM daily air temperature in RCP2.6 and RCP8.5 scenarios, to assess the upper/lower limits of permafrost warming by the end of 21st century. The permafrost warming at depths of 0-50 meters due to sea ice decline is calculated by subtracting permafrost temperature in the no warming case from permafrost temperature in the sea ice warming case. Subtracting the permafrost temperatures in the no warming case from permafrost temperature in RCP (2.6, 4.5 or 8.5) warming cases gives the overall permafrost warming according to a scenario, which would include the combined effect of both the sea ice decline and the radiative forcing (global warming). In the period 1971-2050, the sea ice and the RCP4.5 warming cases are affected by the same extent sea ice decline.

3.3 Results

3.3.1 Control case evaluation

The control case evaluation was conducted for the station/grid point of Barrow, Alaska. This involved monthly-averaged 2-meter air temperature, 2-meter humidity, total cloud cover, and precipitation in the WRF 1970s_HS case, CESM output in the 1970s, and measured observations. For the period of 1971-1980, air temperature and precipitation are the only two observed climatic variables at the Barrow Airport weather station although it has been operational since 1901. Therefore, observed humidity data is chosen in the period of 1981-1990 instead at Barrow Observatory (BRW) by the Earth System Research Laboratory (ESRL, https://www.esrl.noaa.gov/). The observed total cloud cover is obtained from Atmospheric Radiation Measurement (ARM, http://www.arm.gov) program at Barrow in 2001-2010. Involving humidity and total cloud cover observations in mismatched periods is a compromise because of data unavailability. It hardly invalidates model evaluation in this case though, as the purpose is only to qualitatively compare the seasonal cycles to check the reasonability of WRF model dynamics, instead of precisely quantifying biases from modeled to observed variables. Similar comparisons are documented in the supplemental material for Barter Island and Kotzebue, the only two other stations in Arctic Alaska where precipitation and temperature observations are available in the 1970s.

Results indicate that the modeled (WRF and CESM) temperatures deviate less than one standard deviation from the observations from June to January, while having +2 to +7 °C biases in other months (Figure 3.4a). The modeled 2-meter humidity data deviate in a similar manner as air temperature, having negligible biases from June to January and noticeable dry biases (< 0.5 g/kg) for all other months (Figure 3.4b). CESM-modeled total cloud cover has higher seasonal variability and 0.15 to 0.5 lower magnitude than the WRF-modeled cloud cover and the observations (Figure 3.4c). Both the CESM- and WRF- modeled precipitation are 100%~400% higher than observations, with the highest percentage-wise biases occurring during colder months (November to February) (Figure 3.4d). Such dramatic biases in precipitation result at least partially from the challenges associated with observing precipitation in the Arctic, which is addressed later in the discussion section.

3.3.2 Atmospheric responses to sea ice decline

The impacts of sea ice decline are derived from subtracting variables in the high sea ice case from the ones in the low sea ice case (Figure 3.5). The differences between the 2040s_LS and the 1970s_HS cases include overall changes due to both sea ice decline and global warming (in RCP4.5 scenario). The total changes in precipitation and temperature in observations from Barrow are derived from the linear trends in 1970-2016.

The impacts of sea ice decline are more pronounced from October to December than in other months, and more pronounced in the 1970s than in the 2040s. The 1970s temperature responses are up to 4 °C higher from October to December, being 1 °C higher than those in the 2040s. Total cloud cover and precipitation responses are also weaker in the 2040s than in the 1970s. The only exception is the humidity response that is slightly (0.06-0.1 g/kg) stronger in the 2040s than in the 1970s. Some inconsistencies also occur in the responses of summer-time air temperature and total cloud cover. Temperatures in June and July respond with and 0.3 °C cooling in the 1970s and about the same magnitude but with an associated warming in the 2040s. Total cloud cover slightly (<0.01) increases in the 1970s due to sea ice decline, with a similar extent of decrease in the 2040s.

The difference between the two control cases (2040s_LS and 1970s_HS) shows up to 8 °C warming in November and December and 2-3 °C warming in other months in the 2040s, being 2-4 °C higher than the sea ice decline response in all months. The seasonal cycle of the humidity difference has a bimodal shape with two peaks in July (1.2 g/kg) and November (0.6 g/kg). The seasonal precipitation cycle difference resembles that of humidity, with up to 18 mm/month in July and August, and 6 mm/month in December and January. Compared to the impacts of sea ice decline, these increases in humidity and precipitation continually grow stronger in magnitude with time and they are at a maximum in the summer, when sea ice decline responses are minor. The total cloud cover differences do not exhibit any evident seasonal cycle. The observed temperature and precipitation increases from 1970 to 2016 show seasonal cycles similar to the differences between 2040s and 1970s (Figure 3.5 a-d).

The most pronounced response of multi-layer cloud water content (more than 4×10^{-3} g/kg) and specific humidity (0.3 g/kg) also happens in October to December in the layer closest to the surface (0-250 meters) (Figure 3.6). The monthly responses at 0-250 m are in accordance with responses of total cloud cover and 2 m humidity, as the impacts of sea ice decline originate from the surface. The magnitudes of responses expectedly decrease sharply with height, being close to zero above 1.5 km.

3.3.3 Exploration of the summer response inconsistency

The responses of air temperature and total cloud fraction to sea ice decline in summer are similar in magnitudes (0.3 °C in temperature and 0.01 in total cloud fraction) but opposite in direction (decreases in the 1970s and increases in the 2040s). A similar inconsistency is also evident in the cloud water content responses, showing a $2\text{-}3\times10^{-3}$ g/kg decrease in July and August in the 2040s and a similar increase in the 1970s.

To explore the physical mechanism behind the inconsistency of summer temperature and cloud responses, we compare the CESM SST and SIE in June of the 1970 and 2040 study periods (Figure 3.7). The CESM-modeled SST and SIE are identical to those in WRF except for a coarser spatial resolution as WRF regards them only as the boundary condition. As the result, the sea surface off the coast of Arctic Alaska is covered by sea ice in the 1970s in June, while it is ice-free in the 2040s. SST increases accordingly by 1-2.5 °C, which is 120-300% as much as the RCP4.5 global mean SST increase by CMIP5 models (0.8 °C increase from the 1970s to the 2040s, Collins et al., 2013). Designing sensitivity cases by keeping SST unchanged after removing sea ice cover neglects such SST increases (in 1970_LS case). The overly-cold sea surface temperature reverses the orientation of turbulent heat fluxes, mistakenly causing a cold temperature response in summer.

On the other hand, it proves the reasonability of the warm temperature response in the summer of 2040s as the result of both sea ice decline and SST increase (Figure 3.5a).

The low SIE in the 2040s shifts the vertical profile of summer-time air temperature on the North Slope of Alaska by disrupting inversion layers, while no such shift is found in the 1970s (Figure 3.8). A less stable atmosphere inhibits low-level cloud formation in the months of July of the 2040s, so that the cloud fraction is reduced by 0-6 % in lower 500 meters of the land surface in the 2040s_LS case, while enhanced (< 2%) in the 1970s_LS case. In August, this reduction in cloud fraction is sustained, but weaker by the 2040s, and the inversions almost entirely disappear in the 2040_HS case (Figure 3.8b).

3.3.4 Response to sea ice decline in the subsurface

The responses of annual mean surface energy balance to a lower SIE (1970_LS-1970_HS, and 2040_LS-2040_HS) unveil the mechanism of permafrost warming due to sea ice decline (Figure 3.9). The warmed near-surface atmosphere due to sea ice decline transfers more heat downward to the land surface as the form of sensible heat flux. The amounts of increase are respectively 1.07 W/m2 in the 1970s and 0.50 W/m2 in the 2040s. The weaker responses of sensible heat flux coincide with the weaker surface air temperature response presented in figure 3.3. Such shifts in the sensible heat flux bring 0.34 W/m2 (in the 1970s) and 0.10 W/m2 (in the 2040s) higher ground heat flux, both of which are tested significant, as the energy source of permafrost warming. The magnitudes of increases in the ground heat flux are within the range of assessment by Nicolsky and Romanovsky (2017). Due to the deficiency of Noah land surface model in WRF (more details in the discussion section), we employ the GIPL model forced by the surface air temperature to retrieve a more reasonable permafrost temperature regime impacted by both the radiative forcing and sea ice decline.

Comparing permafrost temperature from the RCP4.5 warming case to the no warming case in the 2040s (grey area in Figure 3.10c), to the GIPL-modeled very near-surface permafrost warming (<1 m) is most pronounced in November and December when most of the atmospheric response occurs (Figure 3.10a). The same warming in other months is less than 4 °C for the same layer. In deeper layers (1-5 m), the magnitude of permafrost warming are above 5 °C from November to May. The warming pattern shows that the enhanced ground heat transfers to depth over time. In the months of June to September when snow is not covering the surface, permafrost warming weakens to a negligible level. The sea ice decline induced warming case presents a similar pattern of permafrost warming as in the RCP4.5 warming case, but only with around 20 % in magnitude (Figure 3.10b). The highest extent of warming is between 2-2.5 °C, occurring in November and December within the 0-1 m (active layer and very near-surface permafrost) depths.

The additional soil heat content in the warming cases (sea ice, RCP) shows that the RCP (2.6, 4.5, or 8.5) warming cases accumulate substantially more energy in the permafrost than the sea ice warming case (Figure 3.10c). The sea ice warming case shows a much smoother curve of extra soil heat content over time than that of the RCP warming case, as there is not as much variability of air temperature in its forcing. The extra soil heat content in the RCP4.5 warming case generally keeps increasing at the rate of 30 MJ/m^2 per decade, while the sea ice warming case accumulates heat in permafrost at a much lower rate (5 MJ/m^2 per decade) after the initial warming. By the end of the 2040s, the RCP4.5 warming case has accumulated nearly 300 MJ/m^2 of soil heat content, while the sea ice warming case only 60 MJ/m^2. This comparison suggests that sea ice decline is responsible for around 20% of the total permafrost warming in the period 1970-2050, a close percentage of contribution to that of the permafrost temperature increases (Figure 3.10a-b). By extending the soil heat accumulation curve to the end of the 21st century, roughly 400 MJ/m^2 of extra heat content in RCP 4.5 case if projected, with uncertainty (delimited by the RCP2.6 and RCP8.5 warming cases) ranging from 300 to 480 MJ/m^2. The sea ice warming case only accumulates about 90 MJ/m^2 soil heat content by the end of 21st century.

3.4 Discussion

Compared with observations and CESM output, Polar WRF performs reasonably well in the control simulations, though with some biases. Many of the biases have already been addressed in the literature. The positive temperature bias in spring and summer has been shown to result from overestimation of heat conductivity for the "Tundra" land cover type, which correspondingly causes positive humidity bias from the enhanced evaporation at higher temperatures (Hines et al., 2009 and 2011). The CAM4-produced negative bias in total cloud cover results from underestimating low-level clouds during colder months over the Arctic Alaska (de Boer et al., 2012). Cloud cover was one of the variables that polar WRF improved substantially compared to its forcing. Biases in surface air temperature, humidity, and precipitation have been reduced in polar WRF simulations as well, with varying degree of success. Challenges associated with observations of precipitation, e.g. under-catchment of precipitation are likely to be responsible for at least part of the positive precipitation bias in WRF and CESM (Groisman and Rankova, 2001; Bogdanova et al, 2002; Groisman et al, 2004). Accurate observations of solid precipitation have always been challenging, the causes of which include blowing snow, trace precipitation events, snow accumulating on gauge margins, etc. (Sevruk and Hamon 1984; Goodison et al., 1998; Liljedahl et al., 2017). Solid precipitation is under-measured by at least 50%-100% in cold regions worldwide, depending on the choices of precipitation gauges and wind shields (Serreze et al., 2003).

Sea ice decline impacts originate from the extra heat and moisture released from the open sea surface to the low atmosphere, requiring near-surface atmosphere to be colder than sea surface as a prerequisite. Such temperature regimes typically occur in late fall and early winter when surface air temperature drops below SST, which is accompanied by unfrozen oceanic water off the Northern Coast of Alaska (Lawrence et al., 2008; Screen and Simmonds 2010). In contrast, sea surface temperatures tend to stay cooler than the lower atmosphere in late summer and early fall, orienting the turbulent heat flux downwelling from atmosphere to sea surface (Steele et al., 2010; Alexeev et al., 2015). Such orientation of energy fluxes explain why the most pronounced impacts of sea ice decline happen in late fall and early winter, rather than September with the minimum SIE in a given year.

The idea behind the design of the sensitivity experiments that included swapping SIEs was to estimate the robustness of the response to an identical anomaly in sea ice decline in the two control climates. Changes in the atmospheric background are responsible for the slightly differing responses between the two decades in the past and the future. The higher atmospheric temperature in the 2040s reduces the air-sea temperature gradient, leading to weaker 2 m air temperature response during the cold season than that in the 1970s. At the same time, higher atmospheric temperatures favor more evaporation from the liquid sea surface, making 2 m humidity response stronger in the 2040s.

The WRF-modeled annual mean ground heat flux on the annual mean basis (4-5 W/m2) is higher than observations. Such bias results from the Noah land surface model that calculates the fluxes of outgoing longwave, sensible heat, latent heat, and ground heat at the surface from its computed temperature and moisture (Niu et al., 2011). The overly thin soil depth (1 meter) and overly high soil heat conductivity make Noah land surface model in WRF overestimate the soil temperature, as well as the ground heat flux (Hines et al., 2011). The Noah land surface model computes the absorbed shortwave radiation at surface as the residue of the four fluxes above in the surface energy balance equation (Niu et al., 2011), which transfers the bias in the ground heat flux to the net radiation flux, making the net radiation flux also biased from the observed climatology (Maykut and Church, 1973). This deficiency validates our employment of GIPL model that uses the surface air temperature as the forcing.

We constructed GIPL forcing of the sea ice warming case by taking the average of WRF-modeled air temperature responses to sea ice decline under two atmospheric backgrounds of the 1970s and the 2040s. Although this approach averages out the discussed above asymmetric temperature responses in the summer, choosing one atmospheric response over the other would not significantly affect our results, as the magnitude of air temperature response to sea ice decline in summer is only about 15% as much of that in winter. Furthermore, there is no snow covering the ground as an insulation layer, which contributes to permafrost thermal regimes (Stieglitz et al., 2003).

Compared to overall regional climate change, both atmospheric and sub-surficial, sea ice decline plays a more important role in modulating the seasonal cycle rather than being the dominant contributing factor on the North Slope of Alaska. In the winter, the relative contribution of temperature increases due to sea ice decline never reaches 50% of that associated with the atmospheric warming, while it contributes 25% to that associated with permafrost warming (Figure 3.11). In the summer, the corresponding contributions drop to less than 10% for the atmosphere and to less than 15% for the permafrost.

Satellite and drifting buoy observations in the Chukchi Sea recorded an abrupt SST increase in the summer of 2007 associated with the sea ice minimum (Steele et al., 2010), resembling what CESM RCP4.5 projection simulates in the 2040s compared to in the 1970s (Figure 3.7). Steele et al. (2010) demonstrated that 80% of such SST increase results from the enhanced heat flux absorbed by the ocean because more solar energy can reach the sea surface due to the sharp decline in sea ice extent. According to future projections, as sea ice decline continues, the melting of sea ice off the coast of the Northern Alaska starts earlier in the spring when the low atmosphere above is still colder than the SST, thus making the extensive release of heat and moisture possible, just as in the late fall and early winter. We speculate that in the future the warming effect due to sea ice decline on the North Slope of Alaska can become stronger over time in late spring or very early summer. This could be an impact of sea ice decline that might have been overlooked thus far. Many studies have previously focused on the impacts of sea ice decline in fall and winter (Strey et al., 2010; Screen and Simmonds 2010; Porter et al., 2012) and/or did not assess regional-scale impacts (e.g. the North Slope of Alaska) due to the pan-Arctic scope of their studies (Deser et al., 2010; Screen et al., 2013).

Sea ice retreat in 2007 was also associated with the abnormally low total cloud cover and more sunny days in the summer in the Pacific sector of the Arctic Ocean (Kay et al., 2008; Schweiger et al., 2008a). Kay et al. (2008) attribute such reduction in cloudiness to the atmospheric circulation anomaly, while suggesting that no observational evidence sustains a physical linkage between the sea ice minimum in 2007 and reduced cloudiness (Kay et al., 2009). Documented by the ERA-40 reanalysis dataset (Uppala et al., 2005), an abnormally low sea ice cover in the fall (September to November) is typically associated with a reduction of low cloud fraction for the period spanning 1980-2001 (Schweiger et al., 2008b). Schweiger et al. (2008b) concluded that the extinction of inversion layers and the enhanced instability is the key to such reduced cloudiness. Our model (and the underlying physical parameterizations) simulates such a phenomenon showing that sea ice decline results in the reduction of low-level cloudiness in summer over the North Slope of Alaska by destabilization of the low atmosphere. However, we speculate that such thermodynamically-driven reduction in cloudiness due to sea ice decline is weaker in magnitude than the changes caused by atmospheric circulation (dynamically-driven).

3.5 Conclusions

This study employs both an atmospheric and a permafrost model to isolate the impacts of sea ice decline on the lower atmosphere and permafrost. The impacts of sea ice decline are most important during the late fall and early winter. Delayed freeze-up during the cold season results in a strong air-sea temperature gradient at the surface of unfrozen water that leads to extra heat and moisture released to the low atmosphere, resulting in higher air temperature and humidity, as well as cloudier sky conditions and enhanced precipitation. Nevertheless, global warming plays a leading role in causing climate change on the North Slope of Alaska, while sea ice decline plays an important role in modifying the regional seasonal cycle. The total atmospheric warming induced by sea ice decline accounts for up to 45% in the winter and less than 10% in summer.

More open ocean leads to permafrost warming during winter and spring. The warmer lower atmosphere increases the (downward) sensible heat flux at the surface, thus resulting in the higher net ground heat flux and accumulation of more heat in the subsurface. Similar to atmospheric warming, approximately 20 % of the total permafrost warming is contributed by sea ice decline on a mean annual basis. Global climate change also drives permafrost warming on the North Slope of Alaska, while sea ice decline helps to enhance such warming seasonally by transferring additional heat down to the permafrost during winter and spring.

As sea ice decline continues and accelerates, the late fall and early winter responses in the atmosphere are speculated to become weaker except for near-surface humidity, as a warmer atmosphere reduces the air-sea temperature gradient while enhancing surface evaporation. Warming due to sea ice decline in late spring and early summer, however, is expected to become more prominent, as the sea ice cover off the coast of Arctic Alaska is projected to melt earlier in late spring so that the air temperature is still substantially colder than the SST. Such warming weakens or disrupts inversion layers above the North Slope of Alaska in the summer, resulting in a more unstable atmospheric boundary layer and stronger vertical mixing that inhibits low-level cloud formation. The reduced cloudiness increases the downward transmission of solar energy to the surface, potentially triggering other significant mechanisms, including ice-albedo feedbacks, and result in shifts of important events for ecosystems on the North Slope, such as longer duration of the ice-free periods for the Arctic lakes.

Acknowledgements

This research is funded by National Science Foundation ARC-1107481 and ARC-1417300. We thank Andrew Monaghan for the help on sharing CESM forcing data in the WRF intermediate format. We thank Uma S. Bhatt and Anna Liljedahl for their valuable comments and suggestions as Lei Cai's graduate committee members. Any use of trade, product, or firm names is for descriptive purposes only and does not imply endorsement by the U.S. Government. In terms of authors' contribution, Lei Cai sets the scope of work, conducts the numerical computation, does data analysis, and drafts the manuscript. Vladimir Alexeev, Christopher Arp, and Benjamin Jones set the design of the work, give critical ideas and revision comments on data analysis and manuscript writing. Vladimir Romanovsky contributes on the permafrost modeling part of work, and on revising the science and language of the whole manuscript.

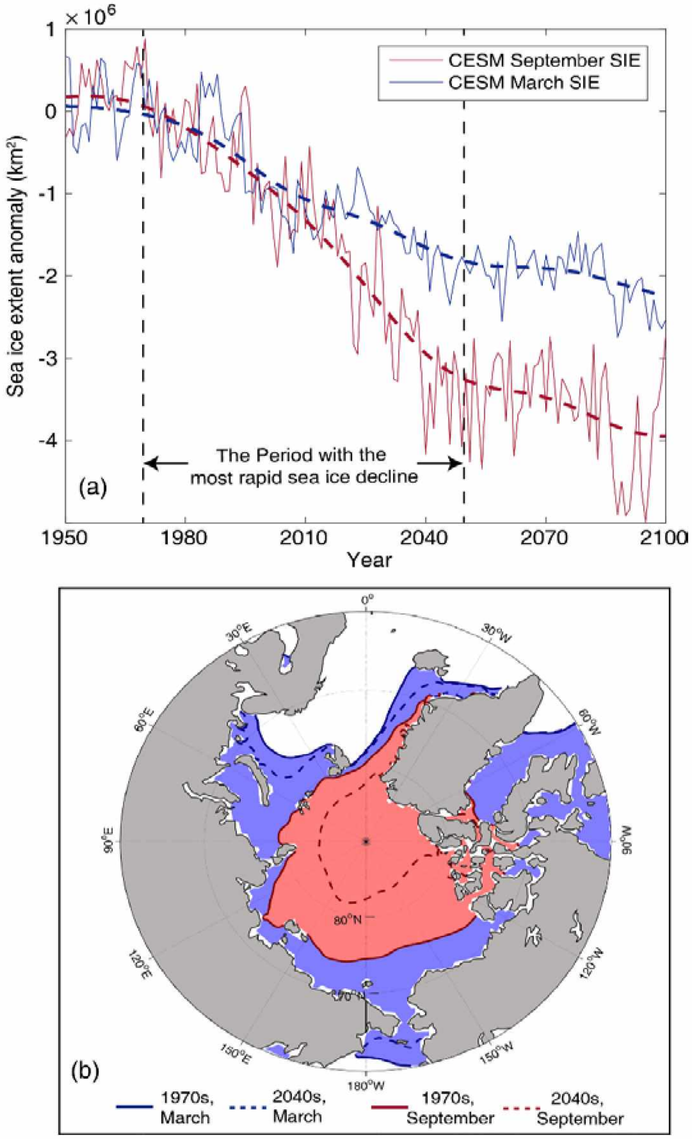

Figure 3.1. (a) CESM Northern Hemisphere sea ice extent anomaly in September (red) and March (blue) from 1950 to 2100. The time series is obtained by concatenating the CESM historical product and the RCP4.5 projection. The anomalies are calculated from the monthly sea ice extent climatology in 1960-1990. The period between 1970 and 2050 is the fastest sea ice decline. (b) CESM sea ice extent in the 1970s (blue solid line for March, and red solid line for September) and the 2040s (blue dashed line for March and red dashed line for September).

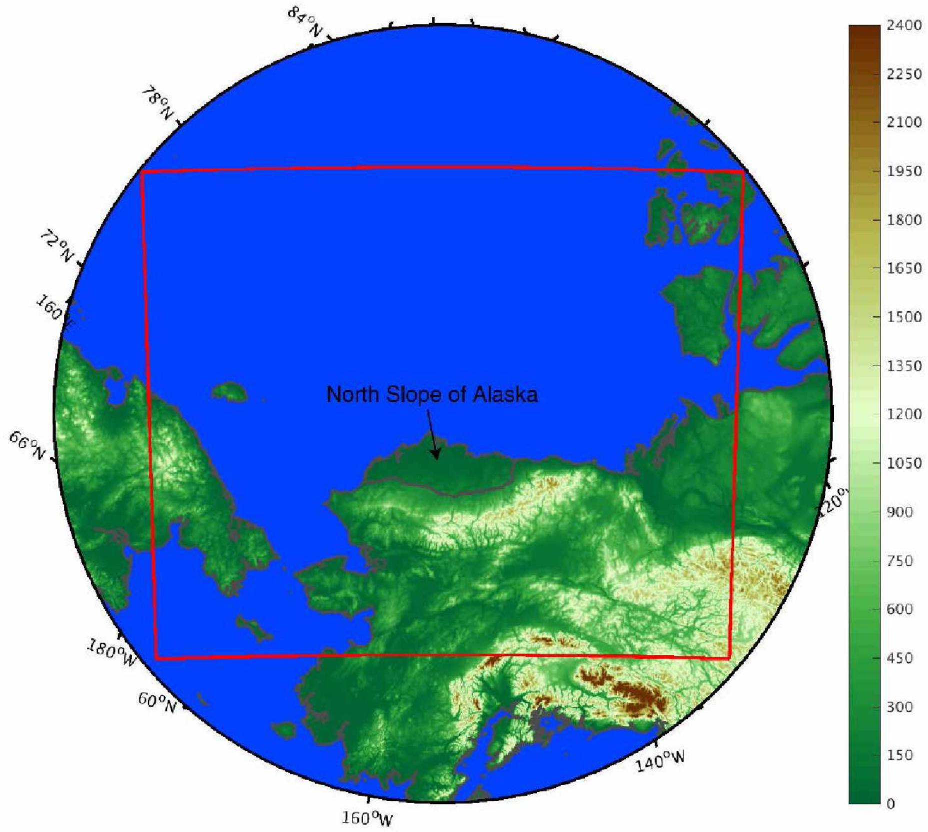

Figure 3.2. The simulation domain (red box) with topography (m) and the boundary of the North Slope of Alaska in this study.

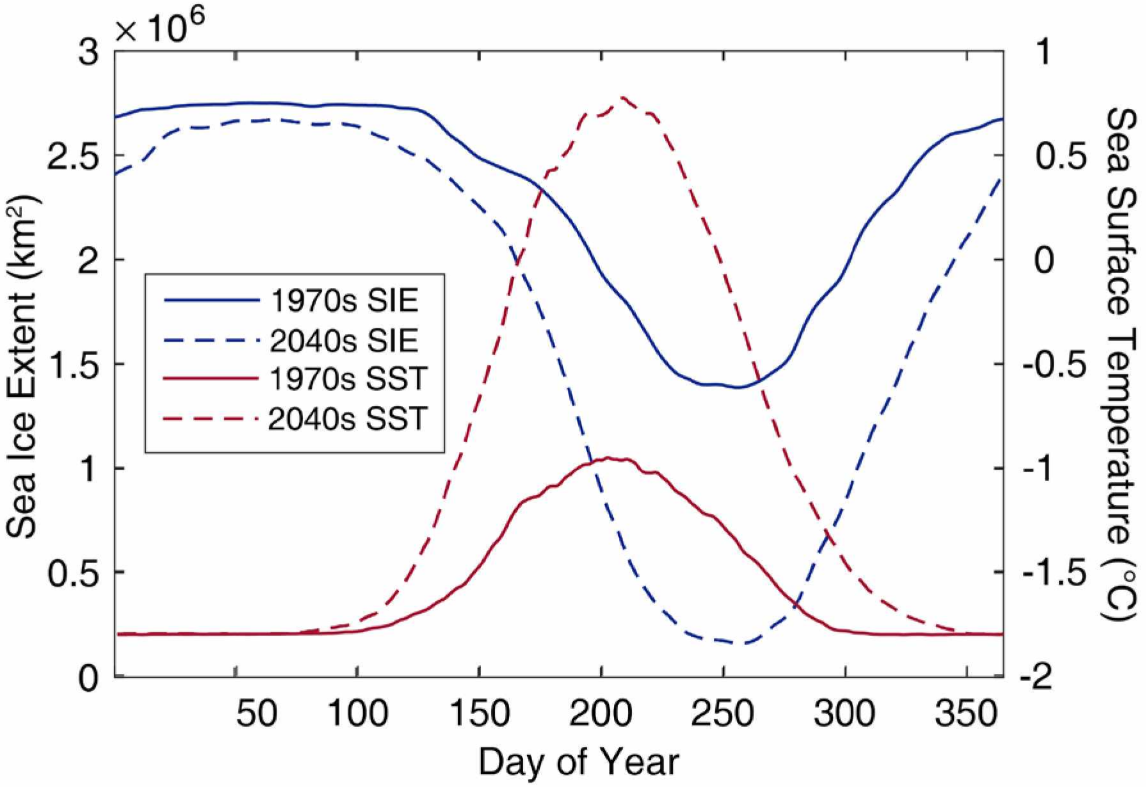

Figure 3.3. The comparison of daily mean Sea Ice Extent (SIE, km^2) and Sea Surface Temperature (SST, °C) in WRF low-level boundary conditions in control cases. The 1970s has higher sea ice extent and lower sea surface temperature compared to the 2040s has.

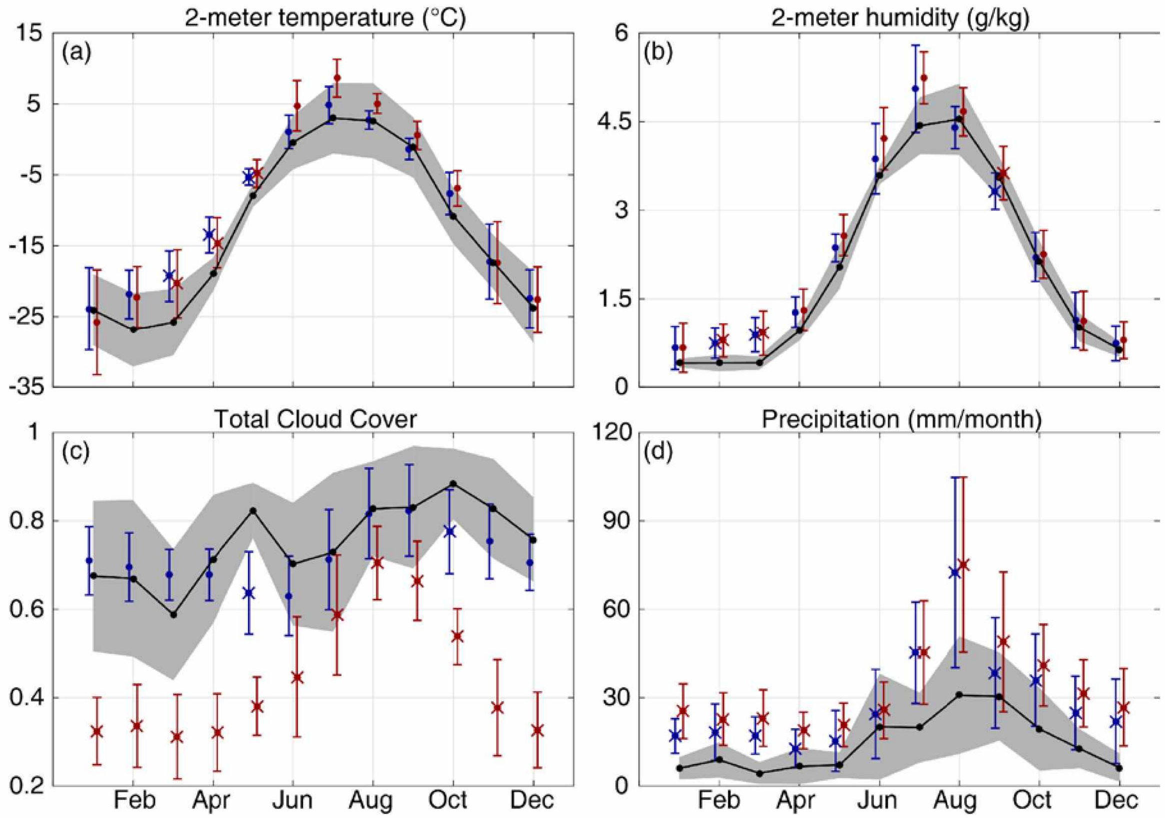

Figure 3.4. The comparisons between WRF model output in 1970s_HS case (blue dots with error bars), CESM historical output in 1971-1980 (red dots with error bars), and observations (black lines with dots) at Barrow for the variables for (a) 2-meter temperature (°C), (b) 2-meter humidity (g/kg), (c) total cloud cover, and (d) precipitation (mm/month). Limited by the observational data availability, only temperature and precipitation observations taken at Barrow airport are taken in the same period of modeled data. Total cloud cover observation by ARM project in 2001-2010 at Barrow, and 2-meter humidity observation is taken at Barrow observatory in 1981-1990. The grey area delimits one standard deviation of observations. X marks on top of CESM and WRF monthly climatology indicate the significance of difference (95% confidence level) from observations.

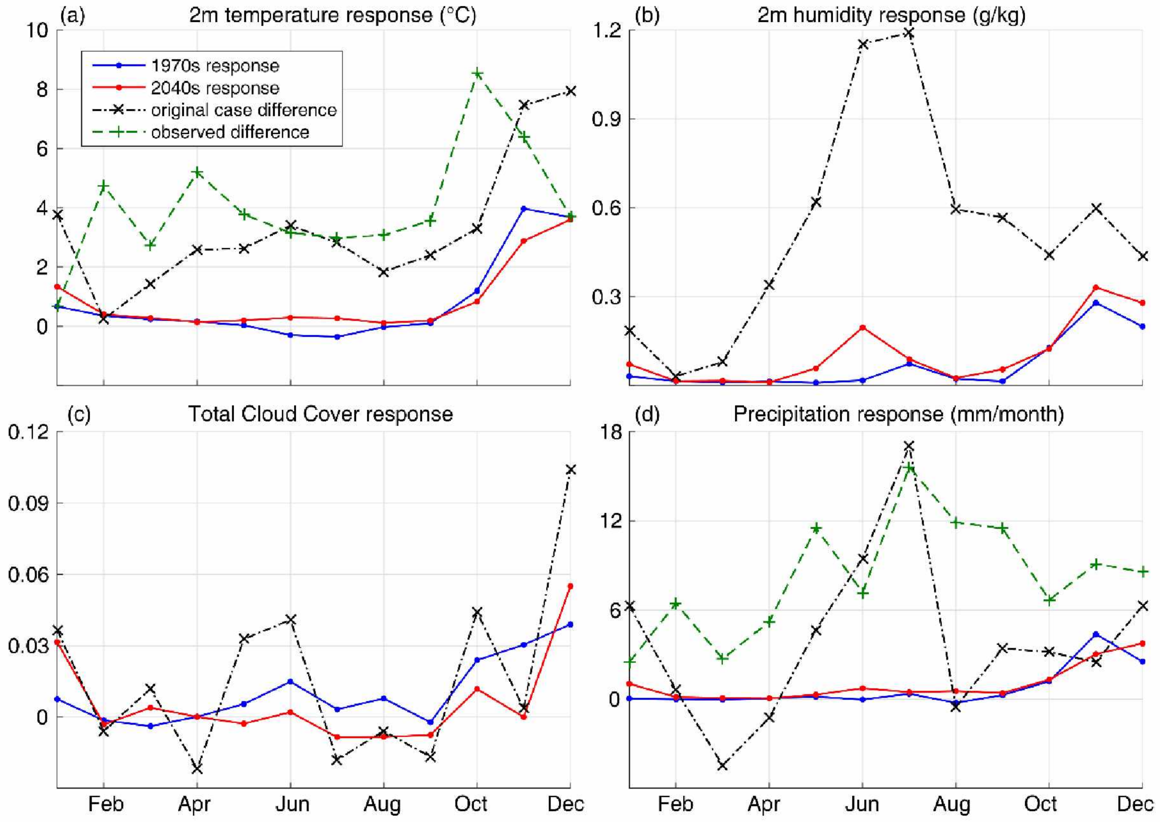

Figure 3.5. The monthly responses (high sea ice case minus low sea ice case) on the North Slope of Alaska of (a) 2 meter temperature (°C), (b) 2 meter humidity (g/kg), (c) total cloud cover, and (d) precipitation (mm/month) with the 1970s (blue lines and dots) and the 2040s (red lines and dots) atmospheric background, and with the difference between two control cases (black dashed-dot lines with X marks, 2040s_LS minus 1970s_HS). For temperature and precipitation responses, observed monthly total changes (green dashed lines with "+" marks) from 1970 to 2016 in Barrow are overlaid to give the reference of observed monthly climate change at Barrow.

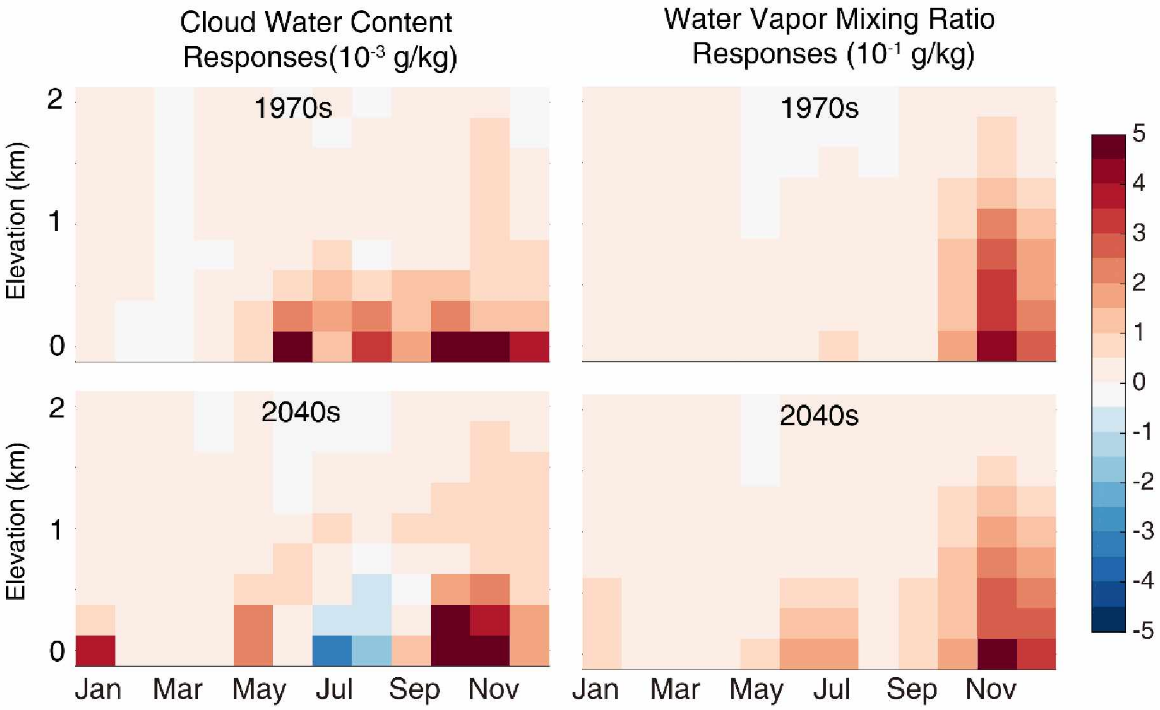

Figure 3.6. Vertical Monthly response profiles from 0-2 km on the North Slope of Alaska of (a) cloud water content (10^{-3} g/kg) in the 1970s, (b) water vapor mixing ratio (10^{-1} g/kg) in the 1970s, (c) cloud water content (10^{-3} g/kg) in the 2040s, and (d) water vapor mixing ratio (10^{-1} g/kg) in the 2040s.

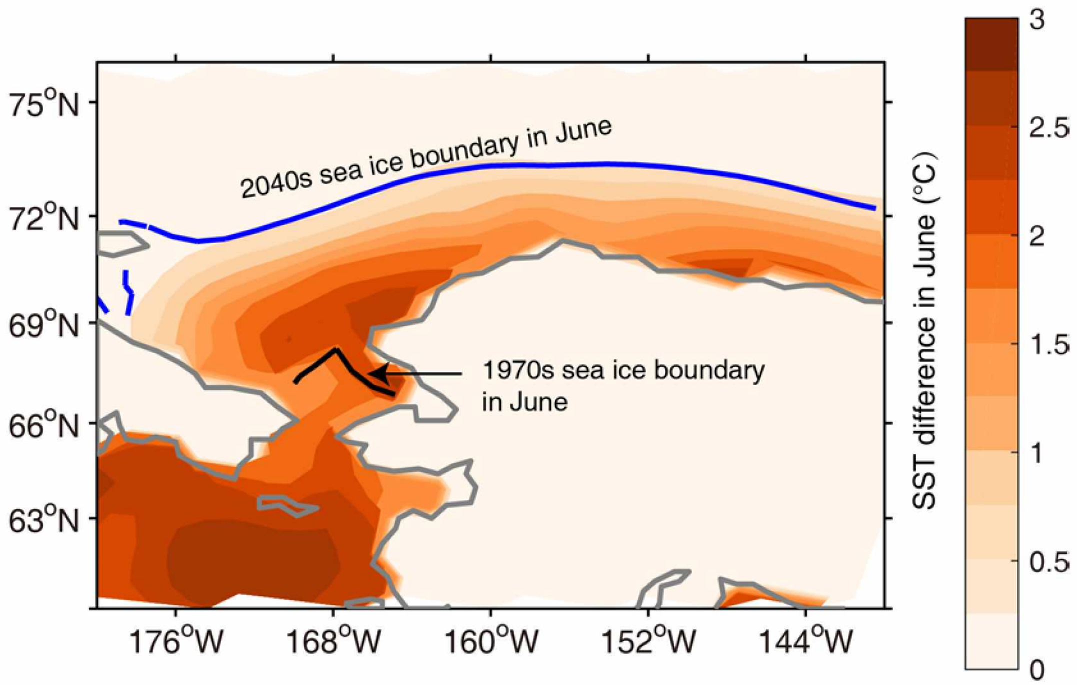

Figure 3.7. SST difference in June from the 2040s in the CESM RCP4.5 product to the 1970s in the historical product with the boundaries of 1970s sea ice extent (black line, historical product) and 2040s sea ice extent (blue line, RCP4.5 projection) in June.

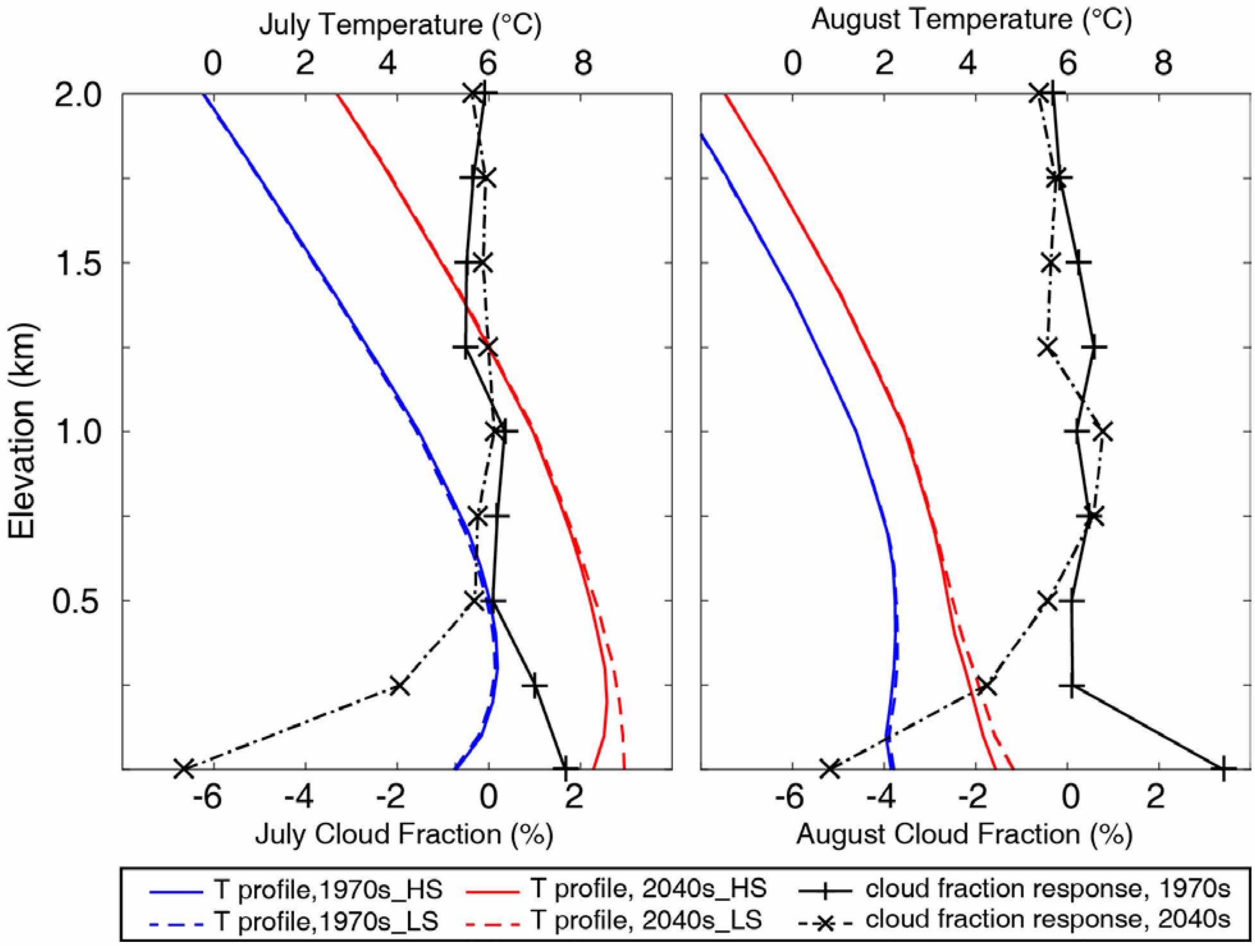

Figure 3.8. (a) Vertical temperature profiles (0-2 km) on the North Slope of Alaska in the 1970s_HS case (blue solid line), 1970s_LS case (blue dashed line), 2040_HS case (red solid line) and 2040_LS case (red dashed line), overlaid with cloud fraction responses in the 1970s (black solid line with "+" marks) and in the 2040s (black dash-dotted line with "X" marks) in (a) July and (b) August, when the most cloud fraction and cloud water content response disagreements are simulated in this study.

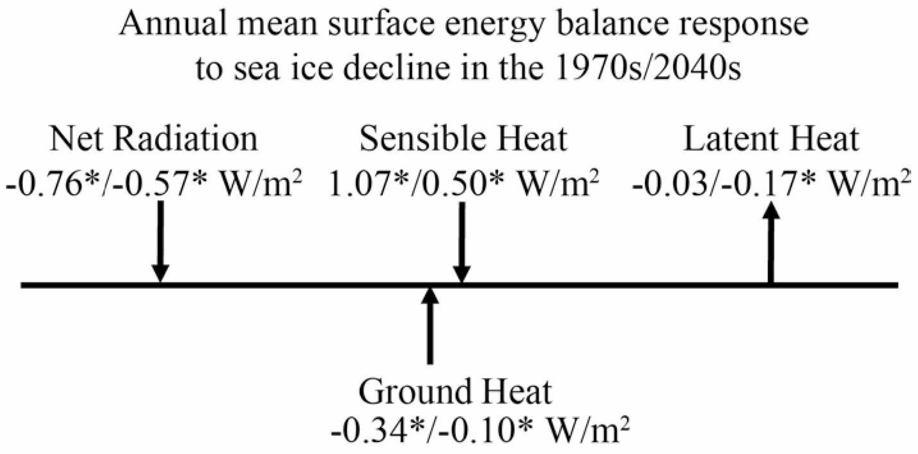

Figure 3.9. The annual mean surface energy balance response to a lower sea ice cover in the 1970s and 2040s. Number with an asteroid indicates that the response is significant, which is tested by the paired Student's t-test at the confidence level of 95%.

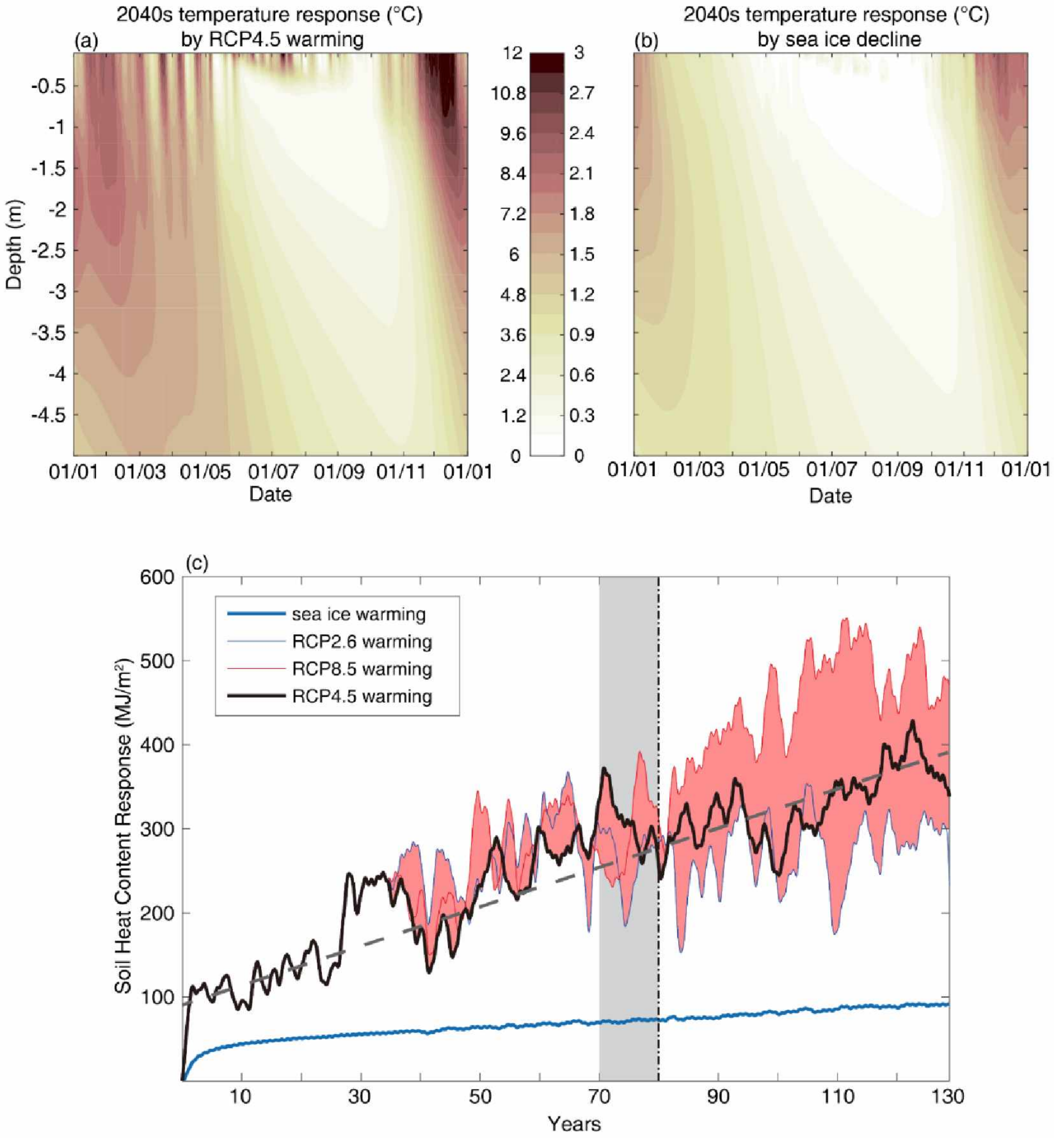

Figure 3.10. The GIPL modeled permafrost temperature responses (temperature differences between warming case and no warming case) in the 2040s (shaded grey in subfigure c) by (a) RCP45 warming case and (b) sea ice warming case, in the depths of 0-5 meters. (c) The soil heat content responses from sea ice warming (bolded dark blue line), as well as RCP4.5 warming (bolded black line), ranged by RCP2.6 warming (light blue line) and RCP8.5 warming (red line).

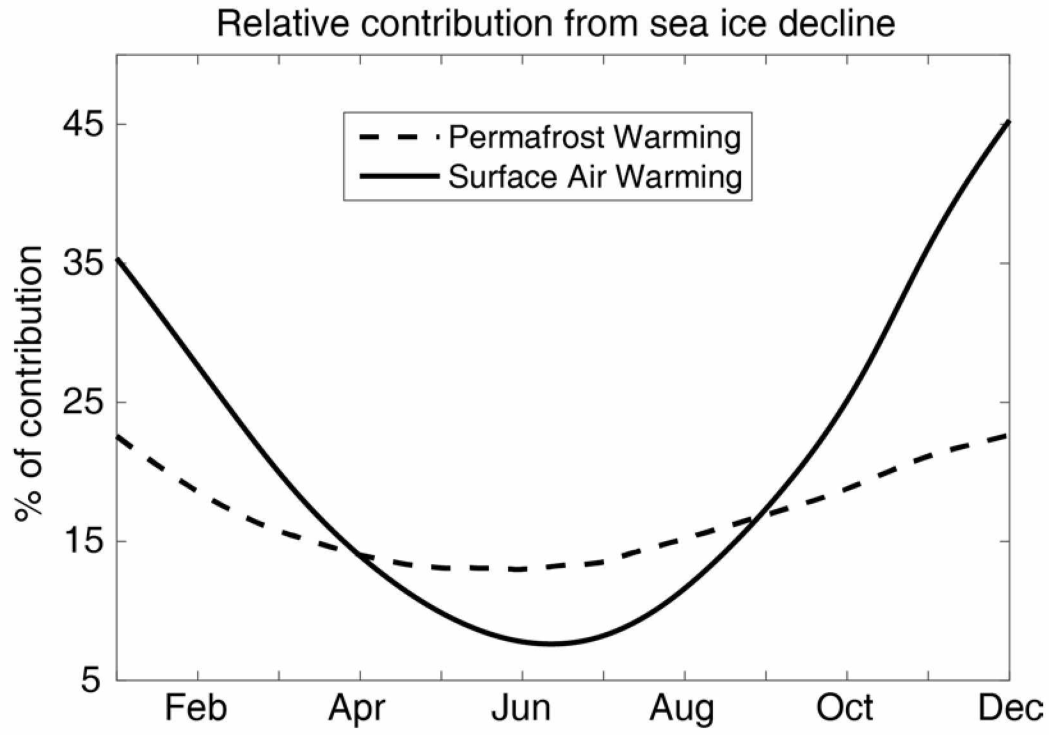

Figure 3.11. Schematic plot representing the seasonal cycle of relative contribution (%) from sea ice decline to the overall warming trends of near surface atmosphere and permafrost on the North Slope of Alaska.

Table 3.1. The list of WRF and GIPL modeling cases. In naming WRF cases, "HS" is the acronym for "high sea ice", and "LS" for "low sea ice".

WRF Cases		
Case Name	Atmospheric Boundary Condition	Sea Ice Boundary Condition
1970_HS (control)	CESM historical, 1970-1980	CESM historical, 1970-1980
1970_LS (sensitivity)	CESM historical, 1970-1980	CESM RCP4.5, 2040-2050
2040_LS (control)	CESM RCP4.5, 2040-2050	CESM RCP4.5, 2040-2050
2040_HS (sensitivity)	CESM RCP4.5, 2040-2050	CESM historical, 1970-1980

GIPL Cases		
Case Name	Daily Temperature Forcing	Monthly Snow Depth
No Warming	CESM 1970s climatology, cycled	CESM 1970s climatology, cycled
Sea Ice Warming	CESM 1970s climatology + WRF temperature response averaged, cycled	CESM 1970s climatology, cycled
RCP4.5 Warming	CESM historical/RCP4.5	CESM historical/RCP4.5
RCP2.6 Warming	CESM historical/RCP2.6	CESM historical/RCP2.6
RCP8.5 Warming	CESM historical/RCP8.5	CESM historical/RCP8.5

References

Alexander, M. A., U. S. Bhatt, J. E. Walsh, M. S. Timlin, J. S. Miller, and J. D. Scott, 2004: The atmospheric response to realistic Arctic sea ice anomalies in an AGCM during winter. *Journal of Climate*, **17,** 890-905.

Alexeev, V. A., E. S. Euskirchen, J. E. Cherry, and R. C. Busey, 2015: Tundra burning in 2007–Did sea ice retreat matter? *Polar Science*, **9,** 185-195.

Alexeev, V. A., C. D. Arp, B. M. Jones, and L. Cai, 2016: Arctic sea ice decline contributes to thinning lake ice trend in northern Alaska. *Environmental Research Letters*, **11,** 074022.

Arp, C. D., B. M. Jones, G. Grosse, A. C. Bondurant, V. E. Romanovsky, K. M. Hinkel, and A. D. Parsekian, 2016: Threshold sensitivity of shallow Arctic lakes and sublake permafrost to changing winter climate. *Geophysical Research Letters,* **43**, 6358-6365.

Barry, R., M. Serreze, J. Maslanik, and R. Preller, 1993: The Arctic sea ice-climate system: Observations and modeling. *Reviews of Geophysics*, **31,** 397-422.

Bhatt, U. S., and Coauthors, 2008: The atmospheric response to realistic reduced summer Arctic sea ice anomalies. *Arctic sea ice decline: Observations, projections, mechanisms, and implications***,** 91-110.

Bhatt, U. S., and Coauthors, 2014: Implications of Arctic Sea Ice Decline for the Earth System. *Annual Review of Environment and Resources*, **39,** 57-89.

Blüthgen, J., R. Gerdes, and M. Werner, 2012: Atmospheric response to the extreme Arctic sea ice conditions in 2007. *Geophysical Research Letters*, **39**.

Bogdanova, E., V. Golubev, B. Ilyin, and I. Dragomilova, 2002: A new model for bias correction of precipitation measurements, and its application to polar regions of Russia. *Russian Meteorol. Hydrol*, **10,** 68-94.

Bruyere, C. L., A. J. Monaghan, D. F. Steinhoff, and D. Yates, 2015: Bias-Corrected CMIP5 CESM Data in WRF/MPAS Intermediate File Format. *TN-515+STR, NCAR***,** 27.

Cai, L., V. A. Alexeev, C. D. Arp, B. M. Jones, A. K. Liljedahl, and A. Gädeke, 2018: The Polar WRF Downscaled Historical and Projected Twenty-First Century Climate for the Coast and Foothills of Arctic Alaska. *Frontiers in Earth Science*, **5**.

Cassano, J. J., M. E. Higgins, and M. W. Seefeldt, 2011: Performance of the Weather Research and Forecasting Model for Month-Long Pan-Arctic Simulations. *Monthly Weather Review*, **139,** 3469-3488.

Cavalieri, D., and C. Parkinson, 2012: Arctic sea ice variability and trends, 1979-2010. *The Cryosphere*, **6,** 881.

Cohen, J., 1994: Snow cover and climate. *Weather*, **49,** 150-156.

Collins, M., and Coauthors, 2013: Climate change 2013: the physical science basis. Contribution of Working Group I to the Fifth Assessment Report of the Intergovernmental Panel on Climate Change. *Long-term Clim. Chang. Proj. Commitments Irreversibility, Cambridge Univ. Press. Cambridge, UK, New York.*

de Boer, G., W. Chapman, J. E. Kay, B. Medeiros, M. D. Shupe, S. Vavrus, and J. Walsh, 2012: A Characterization of the Present-Day Arctic Atmosphere in CCSM4. *Journal of Climate*, **25,** 2676-2695.

Deser, C., R. Tomas, M. Alexander, and D. Lawrence, 2010: The seasonal atmospheric response to projected Arctic sea ice loss in the late twenty-first century. *Journal of Climate*, **23,** 333-351.

Dudhia, J., 1996: A multi-layer soil temperature model for MM5. *Preprints, The Sixth PSU/NCAR mesoscale model users' workshop*, 22-24.

Francis, J. A., and E. Hunter, 2007: Changes in the fabric of the Arctic's greenhouse blanket. *Environmental Research Letters*, **2,** 045011.

Goodison, B. E., P. Louie, and D. Yang, 1998: *WMO solid precipitation measurement intercomparison.* World Meteorological Organization Geneva.

Groisman, P. Y., and E. Y. Rankova, 2001: Precipitation trends over the Russian permafrost-free zone: removing the artifacts of pre-processing. *International Journal of Climatology*, **21,** 657-678.

Groisman, P. Y., R. W. Knight, T. R. Karl, D. R. Easterling, B. Sun, and J. H. Lawrimore, 2004: Contemporary Changes of the Hydrological Cycle over the Contiguous United States: Trends Derived from In Situ Observations. *Journal of Hydrometeorology*, **5,** 64-85.

Handorf, D., R. Jaiser, K. Dethloff, A. Rinke, and J. Cohen, 2015: Impacts of Arctic sea ice and continental snow cover changes on atmospheric winter teleconnections. *Geophysical Research Letters*, **42,** 2367-2377.

Higgins, M. E., and J. J. Cassano, 2009: Impacts of reduced sea ice on winter Arctic atmospheric circulation, precipitation, and temperature. *Journal of Geophysical Research: Atmospheres*, **114**.

Hines, K. M., D. H. Bromwich, M. Barlage, and A. G. Slater, 2009: Arctic land simulations with Polar WRF. *Preprints, 10th Conf Polar Meteorology and Oceanography*, 17-21.

Hines, K. M., D. H. Bromwich, L.-S. Bai, M. Barlage, and A. G. Slater, 2011: Development and Testing of Polar WRF. Part III: Arctic Land*. *Journal of Climate*, **24,** 26-48.

Hines, K. M., D. H. Bromwich, L. Bai, C. M. Bitz, J. G. Powers, and K. W. Manning, 2015: Sea Ice Enhancements to Polar WRF*. *Monthly Weather Review*.

Hong, S.-Y., and J. Dudhia, 2003: 17.3 Testing of a new nonlocal boundary layer vertical diffusion scheme in numerical weather prediction applications.

Hong, S.-Y., H.-M. H. Juang, and Q. Zhao, 1998: Implementation of prognostic cloud scheme for a regional spectral model. *Monthly weather review*, **126,** 2621-2639.

Hu, F. S., P. E. Higuera, J. E. Walsh, W. L. Chapman, P. A. Duffy, L. B. Brubaker, and M. L. Chipman, 2010: Tundra burning in Alaska: Linkages to climatic change and sea ice retreat. *Journal of Geophysical Research*, **115**.

Jones, B. M., C. A. Kolden, R. Jandt, J. T. Abatzoglou, F. Urban, and C. D. Arp, 2009: Fire behavior, weather, and burn severity of the 2007 Anaktuvuk River tundra fire, North Slope, Alaska. *Arctic, Antarctic, and Alpine Research*, **41,** 309-316.

Kain, J. S., 2004: The Kain-Fritsch convective parameterization: an update. *Journal of Applied Meteorology*, **43,** 170-181.

Kay, J. E., and A. Gettelman, 2009: Cloud influence on and response to seasonal Arctic sea ice loss. *Journal of Geophysical Research: Atmospheres*, **114**.

Kay, J. E., T. L'Ecuyer, A. Gettelman, G. Stephens, and C. O'Dell, 2008: The contribution of cloud and radiation anomalies to the 2007 Arctic sea ice extent minimum. *Geophysical Research Letters*, **35**.

Kittel, T. G. F., B. B. Baker, J. V. Higgins, and J. C. Haney, 2010: Climate vulnerability of ecosystems and landscapes on Alaska's North Slope. *Regional Environmental Change*, **11,** 249-264.

Lawrence, D. M., A. G. Slater, R. A. Tomas, M. M. Holland, and C. Deser, 2008: Accelerated Arctic land warming and permafrost degradation during rapid sea ice loss. *Geophysical Research Letters*, **35**.

Liljedahl, A. K., L. D. Hinzman, D. L. Kane, W. C. Oechel, C. E. Tweedie, and D. Zona, 2017: Tundra water budget and implications of precipitation underestimation. Water Resources Research, 53.

Liu, J., J. A. Curry, H. Wang, M. Song, and R. M. Horton, 2012: Impact of declining Arctic sea ice on winter snowfall. *Proceedings of the National Academy of Sciences*, **109,** 4074-4079.

Marchenko, S., V. Romanovsky, and G. Tipenko, 2008: Numerical modeling of spatial permafrost dynamics in Alaska. *Proceedings of the ninth international conference on permafrost*, Institute of Northern Engineering, University of Alaska Fairbanks, 1125-1130.

Maykut, G. A., and P. E. Church, 1973: Radiation Climate of Barrow Alaska, 1962–66. *Journal of Applied Meteorology*, **12,** 620-628.

Mlawer, E. J., S. J. Taubman, P. D. Brown, M. J. Iacono, and S. A. Clough, 1997: Radiative transfer for inhomogeneous atmospheres: RRTM, a validated correlated-k model for the longwave. *Journal of Geophysical Research: Atmospheres (1984–2012)*, **102,** 16663-16682.

Nicolsky, D., and V. E. Romanovsky, 2017: Modeling long-term permafrost degradation. Abstract GC53D-0929 presented at 2017 Fall Meeting, AGU, New Orleans, Louisiana, 11-15 Dec.

Niu, G.-Y., and Coauthors, 2011: The community Noah land surface model with multiparameterization options (Noah-MP): 1. Model description and evaluation with local-scale measurements. *Journal of Geophysical Research: Atmospheres*, **116**.

Noilhan, J., and S. Planton, 1989: A simple parameterization of land surface processes for meteorological models. *Monthly Weather Review*, **117,** 536-549.

Parkinson, C. L., and J. C. Comiso, 2013: On the 2012 record low Arctic sea ice cover: Combined impact of preconditioning and an August storm. *Geophysical Research Letters*, **40,** 1356-1361.

Porter, D. F., J. J. Cassano, and M. C. Serreze, 2012: Local and large-scale atmospheric responses to reduced Arctic sea ice and ocean warming in the WRF model. *Journal of Geophysical Research*, **117**.

Sazonova, T., and V. Romanovsky, 2003: A model for regional-scale estimation of temporal and spatial variability of active layer thickness and mean annual ground temperatures. *Permafrost and Periglacial Processes*, **14,** 125-139.

Schweiger, A., J. Zhang, R. Lindsay, and M. Steele, 2008a: Did unusually sunny skies help drive the record sea ice minimum of 2007? *Geophysical Research Letters*, **35**.

Schweiger, A. J., R. W. Lindsay, S. Vavrus, and J. A. Francis, 2008b: Relationships between Arctic sea ice and clouds during autumn. *Journal of Climate*, **21,** 4799-4810.

Screen, J. A., and I. Simmonds, 2010: Increasing fall-winter energy loss from the Arctic Ocean and its role in Arctic temperature amplification. *Geophysical Research Letters*, **37**.

Screen, J. A., I. Simmonds, C. Deser, and R. Tomas, 2013: The Atmospheric Response to Three Decades of Observed Arctic Sea Ice Loss. *Journal of Climate*, **26,** 1230-1248.

Serreze, M., A. Barrett, J. Stroeve, D. Kindig, and M. Holland, 2009: The emergence of surface-based Arctic amplification. *The Cryosphere*, **3,** 11-19.

Serreze, M. C., M. P. Clark, and D. H. Bromwich, 2003: Monitoring precipitation over the Arctic terrestrial drainage system: Data requirements, shortcomings, and applications of atmospheric reanalysis. *Journal of Hydrometeorology*, **4,** 387-407.

Serreze, M. C., M. M. Holland, and J. Stroeve, 2007: Perspectives on the Arctic's shrinking sea-ice cover. *science*, **315,** 1533-1536.

Sevruk, B., and W. Hamon, 1984: International comparison of national precipitation gauges with a reference pit gauge. *Instruments and Observing Methods Report*.

Skamarock, W. C., and Coauthors, 2008: A description of the advanced research WRF version 3.

Smith, L. C., Y. Sheng, and G. M. MacDonald, 2007: A first pan-Arctic assessment of the influence of glaciation, permafrost, topography and peatlands on northern hemisphere lake distribution. *Permafrost and Periglacial Processes*, **18,** 201-208.

Steele, M., J. Zhang, and W. Ermold, 2010: Mechanisms of summertime upper Arctic Ocean warming and the effect on sea ice melt. *Journal of Geophysical Research: Oceans*, **115**.

Stieglitz, M., S. Déry, V. Romanovsky, and T. Osterkamp, 2003: The role of snow cover in the warming of arctic permafrost. *Geophysical Research Letters*, **30**.

Strey, S. T., W. L. Chapman, and J. E. Walsh, 2010: The 2007 sea ice minimum: Impacts on the Northern Hemisphere atmosphere in late autumn and early winter. *Journal of Geophysical Research: Atmospheres*, **115**.

Stroeve, J. C., V. Kattsov, A. Barrett, M. Serreze, T. Pavlova, M. Holland, and W. N. Meier, 2012: Trends in Arctic sea ice extent from CMIP5, CMIP3 and observations. *Geophysical Research Letters*, **39**.

Taylor, K. E., R. J. Stouffer, and G. A. Meehl, 2012: An overview of CMIP5 and the experiment design. *Bulletin of the American Meteorological Society*, **93,** 485-498.

Uppala, S. M., and Coauthors, 2005: The ERA-40 re-analysis. *Quarterly Journal of the Royal Meteorological Society*, **131,** 2961-3012.

Walsh, J. E., W. L. Chapman, and D. H. Portis, 2009: Arctic cloud fraction and radiative fluxes in atmospheric reanalyses. *Journal of Climate*, **22,** 2316-2334.

Wendler, G., B. Moore, and K. Galloway, 2014: Strong temperature increase and shrinking sea ice in arctic Alaska. *The Open Atmospheric Science Journal*, **8,** 7-15.

Wilson, A. B., D. H. Bromwich, and K. M. Hines, 2011: Evaluation of Polar WRF forecasts on the Arctic System Reanalysis domain: Surface and upper air analysis. *Journal of Geophysical Research*, **116**.

——, 2012: Evaluation of Polar WRF forecasts on the Arctic System Reanalysis Domain: 2. Atmospheric hydrologic cycle. *Journal of Geophysical Research*, **117**.

Zhang, T., T. Osterkamp, and K. Stamnes, 1997: Effects of climate on the active layer and permafrost on the North Slope of Alaska, USA. *Permafrost and Periglacial Processes*, **8,** 45-67.

Appendix B

In the Arctic circle, there are only two stations in Alaska other than Barrow has observation data available in the 1970s stored in NCDC GHCN-D, which are Kotzebue (66°53′50″N, 162°35′8″W) and Barter Island (70°08′02″N, 143°34′55″W).

Kotzebue is actually in a different climate division from the North Slope of Alaska, as it is more affected by the warmer oceanic water in the Bering Strait and warm air from the Northern Pacific (Figure B-1). That is the reason why the temperature and precipitation are higher in all months compared to those at Barrow. The land cover type of Kotzebue in WRF is not tundra, therefore the warm biases in late winter and early spring are smaller than those in Barrow and Barter Island. Modeled by WRF, Kotzebue is modeled not only with high amounts but also high variabilities of monthly precipitation, implying more extreme precipitation events happening in this humid part of Arctic Alaska. The climate comparisons between models and observations are Barter Island is similar to that in Barrow, as they are both on the coastline of Northern Alaska. Warm temperature biases also occur at Barter Island, just like in Barrow. Compared to Kotzebue, Barter Island has lower temperatures and precipitation all year round.

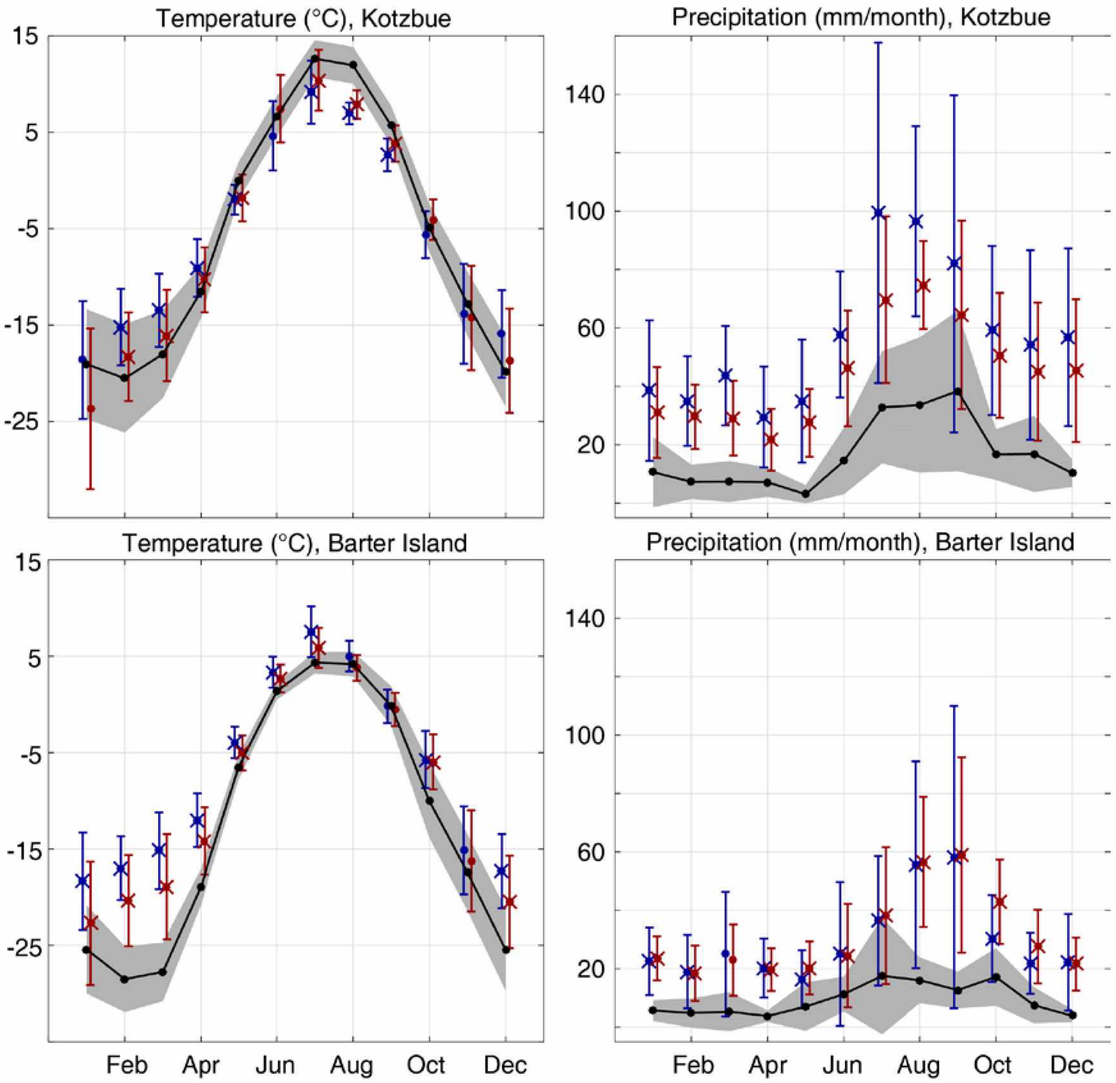

Figure B-1. The monthly climatology of temperature and precipitation at Kotzebue and Barter Island in observation (black lines with black dots and gray shades), the CESM historical product (red X mark with error bar), and the WRF simulation (blue X mark with error bar).

Chapter 4 Earlier lake ice-off contributes to warming of near-surface atmosphere and permafrost in Arctic Alaska[3]

Abstract

Arctic lakes are an important land cover type in arctic lowland regions. The timing of the disappearance of ice on lakes is an important event having an impact on lake and tundra ecosystems, and a trend towards earlier ice-off has been observed since the 1970s. We designed a set of sensitivity experiments to study the impacts of earlier lake ice-off on the near-surface atmosphere and permafrost. Results from atmospheric and permafrost models show that earlier lake ice-off warms both the near-surface atmosphere and upper layers of permafrost. Strongest atmospheric warming is generated on the downwind side of lakes as a result of earlier lake ice melt. A weaker surface-air temperature gradient over land inhibits the upward sensible heat flux, thus forcing the extra heat to penetrate down to the subsurface. In response to the shift in the surface energy budget permafrost warms, with most of the warming occurring deeper than 1 meter during winter and spring when snow cover insulates ground heat from being emitted to the atmosphere. With more snow expected in climate projections this lake ice-off warming effect in the permafrost is speculated to become stronger. The projected lake ice regime shift from bedfast to floating ice observed on the Northern coast of Alaska is likely to restrain the ice-off date from moving earlier in the year. The described lake ice-off effect is substantially weaker compared to the similar ocean-ice effect and even more so to overall global warming.

4.1 Introduction

Arctic lakes are an important land cover type in arctic lowland regions (Grosse et al., 2013). However, their surface is ice-covered for 60%-80% of the year, providing a barrier for direct heat and moisture exchange between water bodies and the atmosphere (Duguay et al., 2003; Smith et al., 2007; Brown and Duguay, 2011; Prowse et al., 2011). During the past decade, lake ice cover has been found thawing earlier (Duguay et al., 2006; Arp et al., 2015; Šmejkalová et al., 2016). The Arctic sea ice decline also contributes to an earlier lake ice thawing that the enhanced snowfall from sea ice decline inhibits lake ice from growing thicker in winter (Alexeev et al. 2016).

---

[3] Cai, L., V. A. Alexeev, C. D. Arp, B. M. Jones, 2018: Earlier lake ice-off contributes to warming of near-surface atmosphere and permafrost in Arctic Alaska, *Environmental Research Letters,* in preparation for submission.

It therefore raises the question of how the earlier opening of Arctic lakes in summer influences the surface energy balance and regional climate, the interaction between which has been addressed through observational analysis or radiation balance models (Zhang et al., 2000; Morris et al., 2005; Rouse et al., 2005; Surdu et al., 2014).

Routine observations of climatic variables have always been challenging in Arctic Alaska with the harsh environment, low population density, and poor road infrastructure (Shulski and Wendler, 2007). Alternatively, Regional Climate Models (RCM), such as the Weather Research & Forecast (WRF) model, can retrieve the atmospheric dynamics and physical processes in the regional scale and fine resolution (Hines et al., 2009; DuVivier and Cassano, 2013; Förster et al., 2014; Glisan et al., 2014). WRF's modeling framework is also suitable for designing and conducting sensitivity experiments by prescribing surface boundary conditions while fixing atmospheric boundary conditions. Such a sensitivity test approach has been applied in Arctic on exploring the Arctic sea ice decline impacts (Strey et al., 2010; Porter et al., 2012; Alexeev et al., 2015). However, all previous RCM-based studies with an Arctic focus skip exploring the impacts of Arctic lake surface thawing/refreezing. It is because resolving Arctic lakes not only requires an extra fine grid spacing but also a detailed geographical background, both of which are very expensive computationally.

In this study, we focus on the impacts of the earlier lake ice-off to the near-surface atmosphere and permafrost temperature regimes for a lake-rich landscape in Arctic Alaska by conducting sensitivity experiments employing both atmospheric and permafrost models. We designed WRF sensitivity experiments by prescribing the lake ice-off date and the lake surface temperature. The Geophysical Institute Permafrost Laboratory (GIPL) model forced by WRF-modeled air temperature quantifies the impact of the earlier lake ice-off to the permafrost temperature regime. These model experiments were validated using local weather and ground temperature station observations. Our findings highlight the role of the lake ice-off on the local scale heat and moisture transfer within the near-surface atmosphere and the subsurface.

4.2 Observations and Model initialization

4.2.1 Observations of earlier lake ice-off

Šmejkalová et al. (2016) have discovered through observations that the lake ice-off in Arctic Alaska has been advancing at the rate of 1 day earlier per year since 2000. Extending this analysis back to 1975 using additional satellite image observations (Landsat, AVHRR, SPOT, Radarsat) retrieves a 0.8 days/year trend for Teshekpuk Lake towards earlier ice-off (Figure 4.1a). Teshekpuk Lake, the largest lake in Arctic Alaska, has an area of 430 km^2 and the depth less than 7 meters. Its disproportionately large size and shallow depth manifest the potential of influencing the temperature and moisture regimes in the near-surface atmosphere and permafrost layers nearby (Arp et al., 2010). Five stations (Drew Point, Inigok, Fish Creek, South Meade, and Piksiksak) operated by the U.S. Geological Survey as a part of Global Terrestrial Network for Permafrost (DOI/GTN-P) has been observing surface air and multi-depth permafrost temperatures (Clow 2014; Urban and Clow, 2014). The 70 cm permafrost temperature anomalies in July are found significantly correlated (95% confidence level) with the ice-off date anomalies of Teshekpuk Lake in 1998-2015 (Figure 4.1b).

We could not find any significant correlation between Teshekpuk Lake ice-off date and the surface air temperature in field observation data by means of simple statistical analysis. We speculate that the earlier lake ice-off does not result in any significant widespread extra warming of the near-surface atmosphere because it is of too small a magnitude to be distinguished from the observed synoptical background variability. However, we may be able to capture such impacts of the land cover change by conducting WRF sensitivity experiments, which constitutes the main goal of the article: to quantify the impacts of the earlier lake ice-off by comparing WRF simulations under different land cover characteristics (earlier lake ice melt) while keeping the atmospheric background unchanged.

4.2.2 Model framework

The two summers of 2005 and 2015 have a one-month difference (Aug 1st vs. June 30th) on the ice-off date of Teshekpuk Lake in observation (Figure 4.1a), which dictates the simulation period to be set to June 1st – August 1st in 2005 and 2015. The month of June will be discarded as a spin-up period, two control simulation for 2005 and 2015 will be forced with "observed" lake ice and two sensitivity experiments will be conducted with prescribed lake ice conditions and lake ice temperatures.

We design and conduct a set of WRF (version 3.7.1) sensitivity experiments forced by the ERA-interim reanalysis dataset (Skamarock et al., 2008; Dee et al., 2011). The simulation domain centers in the lake-rich region of Arctic Alaska. More details on the simulation domain, and the parameterization schemes combination are in the supplemental material. WRF model in this study outputs variables on 31 atmospheric layers up to 50 hPa, and on 4 subsurface soil layers (10 cm, 30cm, 70cm, and 100 cm in depth), in an hourly time interval. Each layer is gridded into 1000×800 points with a 500 meters horizontal grid spacing. Such high-resolution domain is accompanied by the 9-second static geographic data by National Land Cover Database 2006 for a correspondingly fine land cover data containing a substantial amount of resolved Arctic lakes (Fry et al., 2011). This high-resolution framework refines the size of resolvable lakes to as small as 25 ha.

We single out Arctic lakes by searching grid points with both the land cover type of "water body" and the altitude higher than 0 meters (sea level). This approach may also treat some bays and lagoons off the Northern Coast of Alaska as lakes as these regions are with altitudes higher than 0 meters in the static geographic data, which may slightly contaminate the results. Two control cases (2005_late and 2015_late) are simulated without any prescribing of surface boundary condition. WRF Preprocessing System (WPS) interpolates ERA-interim sea ice field onto the lake surface in the WRF domain when building the surface boundary condition for simulation. Therefore the lake ice-off date actually depends on when the sea ice is melt off the Northern Coast of Alaska in WRF. Such technical imperfection makes the lake ice-off date in WRF far from in observation in the 2015 control case (July 23rd, Table 4.1). To prescribe a substantial ice-free period, two sensitivity cases (2005_early and 2015_early) have to be designed by removing all lake ice covers in the simulation domain on June 30th, making the 31-day (in 2005) and 23-day (in 2015) earlier ice-off than that in the corresponding control cases.

The lake surface temperatures were modified after ice-off for a more realistic relationship between the lake surface temperature and the surface air temperature. Derived from the observations by Arp et al. (2015), we designed a lake surface temperature adjustment algorithm. After the ice-off, the lake surface temperature is firstly warmed linearly, matching the daily maximum air temperature four days later. The lake surface temperature after the matching is calculated from a 7-day moving average of the daily maximum air temperature. This algorithm is applied in order to imitate the behavior of the lake surface temperature change following the surface air temperature because WRF does not have a module to simulate such interaction. The lake surface temperatures are kept approximately at the freezing point due to the presence of lake ice cover in the control cases, while it is prescribed to be warmed by the air temperature after the ice-off in the sensitivity cases (Figure 4.2). Prescribed in such a way, lake surface temperature compares reasonably well with the observed change of lake surface temperature after ice-off (Figure C-2). After all four cases are done simulating, responses were calculated by subtracting variables in the late melt cases (control cases) from ones in the corresponding early melt cases (sensitivity cases).

WRF's subsurface is parameterized too shallow (Noah land surface model parameterizes only 1-meter thick soil layer) to properly represent the permafrost temperature regime on the Northern coast of Alaska. The GIPL model (version 2.0) is alternatively utilized in order to numerically examine the impact of the earlier lake ice-off to permafrost (Marchenko et al., 2008). The surface air temperature data used as this one-dimensional GIPL model forcing is from ERA-interim reanalysis data. To construct a 60-year long forcing of daily temperature, we duplicate and concatenate the daily temperature in 2005 at Ikpikpuk for 60 times. Ikpikpuk surface air temperature in ERA-interim is obtained by a bi-linear interpolation. The sensitivity forcing was derived by adding the WRF modeled 2005 temperature response at Ikpikpuk to the control forcing in every July of the 60-year period. This artificially constructed control climate filters out the warming trend, thus isolating the permafrost warming component that is solely due to the earlier lake ice-off. Permafrost temperature response is calculated by subtracting permafrost temperature in the control case from that in the sensitivity case.

4.3 Results

This section deals with the analysis of responses in the near-surface atmosphere and the permafrost to the earlier lake ice-off. Atmospheric responses are calculated in July only. Permafrost temperature is analyzed for its response throughout the year and this response is put in perspective regarding its importance in comparison with other factors, e.g. declining sea ice and overall global warming.

4.3.1 Spatial distributions of responses

Figure 4.2 shows that the control cases reasonably well reproduce the daily surface air temperatures over Teshekpuk Lake, and the lake surface temperature adjustment successfully recaptures the relationship between the lake surface temperature and air temperature. The temperature biases in WRF are below 2 °C compared to observations during most of the simulation period. 2015 is warmer than 2005 that the averaged surface air temperature during this 61-day simulation period is 3.1 °C higher in 2015 than in 2005. The hourly wind speed/direction averaged on the Northern coast of Alaska show that the dominant wind direction in July is ENE (Figure 4.2c and 4.2d). Hours with a wind direction of ENE in 2015 is about 30% less frequent than in 2005. Wind speed in 2015 is also lower on average in July that fewer hours are with high wind speed (>6 m/s) in 2015 than in 2005.

The surface air temperature and humidity responses to the earlier lake ice-off are found propagating that at least 0.2 °C temperature response and 0.1 g/kg humidity response spread all over the North coast of Alaska (Figure 4.3). Some obvious slight 'contamination' from the ocean coastal areas also exists, which we estimate to be comparable with the minimum changes. The most pronounced temperature and humidity responses occur on the southwest side of lakes, that is, the downwind side of the dominant wind direction in July on the Northern Coast of Alaska. More than 1 °C temperature increase and 0.4 g/kg humidity increase on average is modeled in these regions. Teshekpuk Lake, the biggest lake in the study area, is associated with the greatest responses on its downwind side. Strong temperature (> 1 °C) and humidity (> 0.4 g/kg) anomalies propagate > 30 km to the southwest.

Maximal temperature and humidity responses to the southwest of Teshekpuk Lake are close in 2005 and 2015 in magnitude, but responses in 2015 are more widespread than in 2005 over the Northern coastal Alaska. The spatial averaged responses in 2015 are 0.12 °C (0.66 °C vs. 0.54 °C) higher in temperature while 0.04 g/kg (0.22 g/kg vs. 0.18 g/kg) higher in humidity, than those in 2005. Some shallow oceanic water bodies or lagoons, like the Admiralty Bay, also generate responses on their downwind side. As mentioned above, these regions are treated as lakes mistakenly by our algorithm, as the static geographic data in WRF assigns a higher-than-zero altitude. To keep off these areas, we specifically focus on Teshekpuk Lake and its downwind regions for further analyses.

Hourly temperature and humidity responses at Ikpikpuk station and East Teshekpuk Lake station (blue X marks in Figure 4.3a) illustrate that the substantial temperature and humidity responses emerge only when the surface wind blows from Teshekpuk Lake to stations. At Ikpikpuk, the favorable wind direction for temperature/humidity impacts is ENE (Figure 4.4a), while at East Ikpikpuk is W (Figure 4.4b). There are not as many hours with prominent responses happening at East Teshekpuk Lake as those at Ikpikpuk as the west wind is not dominant on the Northern coastal Alaska in summer. With the preconditioning of the favorable wind direction at Ikpikpuk (ENE), more than half of the hourly temperature response varies in magnitude between 2 °C and 3 °C (Figure 4.4c). We did not find any significant relationship between the wind speed and the strength of temperature response, but the temperature response has the tendency of converging to its most common magnitude (2-3 °C) as the wind speed goes up. The humidity response behaves similarly to the wind speed as the temperature response does (Figure is not shown here). In summary, a higher wind speed does not lead to significant changes in the strength of downwind impacts.

4.3.2 Vertical structures of responses

We set a 150 km long cross-section through Teshekpuk Lake and three smaller lakes to its southwest (blue solid line in Figure 4.3a). The vertical structure of response reveals that the temperature and moisture anomalies originate from lakes, and propagating both to the low atmosphere and to the subsurface (Figure 4.5). More than 1 °C temperature response and 3 g/kg humidity response propagate up to 100 m vertically, and 30 km horizontally (Figure 4.5a and 4.5b). The subsurface warming response is restricted in the 0-70 cm soil layer, and the soil moisture does not respond consistently in shallow layers as it depends primarily on precipitation (10 cm depth). In 2015, a soil moisture decrease of 0.02 m^3/m^3 at the 70 cm level, and an increase of similar magnitude at 100 cm level are found 20 km downwind to Teshekpuk Lake.

4.3.3 Rebalance of surface energy budget

The warmed near-surface atmosphere and shallow permafrost due to the earlier lake ice-off interfere the heat transfer between the atmosphere and surface, and between the surface and subsurface. The surface energy budgets are compared in July within a sub-domain (154-155° W; 70.3-70.7° N), which covers most of the downwind area of Teshekpuk Lake (Figure 4.6a). As a result, the net radiation flux at surface drops 1.82 W/m^2 in 2005 and 1.59 W/m^2 in 2015. The net radiation flux decreases primarily due to the radiation extinction by extra moisture from lakes. The weakened land-air temperature difference decreases sensible heat flux by 3.20 W/m^2 and 3.14 W/m^2 in 2005 and 2015, respectively, while no substantial latent heat flux change is found in both years. For the subsurface, the downward ground heat flux increases by 0.83 W/m^2 in 2005 and 0.88 W/m^2 in 2015, implying more heat is transferred down to the subsurface. The errors stand for the variability (one standard deviation) of energy fluxes at surface for each grid point in the sub-domain. The variabilities are diminished for the sensible heat flux while enhanced for the latent heat flux in the early melt cases. It implies that the extra atmospheric warming results in more spatial consistency on the land-air temperature gradient while less on the surface evaporation.

Net radiation flux at surface in 2015 decreases for 18 W/m^2 from that in 2005, though it does not result in substantial differences in responses in sensible, latent, and ground heat fluxes. Near-surface air temperature response at Ikpikpuk reveals that the mean temperature responses in 2005 and 2015 are very similar to each other on average (1.4 °C in 2005 and 1.48 °C in 2015), while they change differently over time (Figure 4.6c and 4.6d). In 2005, the temperature response enhances rapidly after July 15th (Figure 4.6c). In 2015, the temperature response maximizes (3.2 °C) as early as on July 5th, and weakening gradually after (Figure 4.6d). The lake ice-off warming is well-corresponding to the surface air temperature change over time. In 2005, the daily surface air temperature at Ikpikpuk maximizes (13.6 °C) on July 15th, the lake ice-off warming is enhanced after that as the surface air temperature starts to drop. In 2015, the maximum daily temperature in July occurs on July 2nd (14.9 °C), and the temperature response is peaked on July 5th after the lake surface temperature adjustment completes.

4.3.4 GIPL-modeled permafrost warming

There are two periods of substantial GIPL-modeled permafrost temperature response in a year for the shallow permafrost (depth < 1m, Figure 4.7a). The first period is in July when the warmed near-surface atmosphere heats up the permafrost as the only source of energy for the lake ice-off induced permafrost warming, for which the magnitude is higher than 0.4 °C. The summer warming is strong in magnitude but fails to penetrate deeper as there is no snow cover insulating the extra heat within the permafrost layer. The second period begins in October when the snow starts to fall. The snow cover inhibits the surface heat transmitting to the atmosphere. Such insulation makes the snow cover an important contributing factor to the permafrost warming. Deeper layers (depth >

1 m) of permafrost are warmed less in magnitude due to the lake ice-off and with a slower rate than the shallow layers (depth < 1 m). The warming in October takes roughly a month to influence the deeper permafrost (5 meters). The extra warming is retained until the snow cover melts in the following spring when the extra heat dissipates gradually back into the air.

A new equilibrium of permafrost temperature regime is generally met after 10 years (Figure 4.7b). The permafrost is around 0.18 °C warmer for the active layer (0-0.4 m), and around 0.08 °C warmer underneath which, than that of the control case. The extra soil heat content accumulation is stabilized to the rate of 0.25 MJ/m^2 per decade.

4.4 Discussion

This study employs both an atmospheric (WRF) and permafrost (GIPL) models to explore impacts of the earlier lake ice-off to the Northern Coast of Alaska. When the ice cover melts earlier, the Arctic lakes result in extra temperature and humidity increases in the near-surface atmosphere to the downwind side of lakes. The wind direction drives the propagation of heat and moisture from the opened lake surface, while the wind speed influences the variability of the warming impact. We speculate the reduced variability of lake ice-off warming in high wind dues to the inhibited vertical mixing from surface wind in the atmospheric boundary layer.

Roughly 70% of Arctic lakes along the North coast of Alaska, most of which are small in size and shallow in depth, are still not resolvable in the 9-seconds static geographic data. Smejkalov et al. (2016) indicate that small arctic lakes (< 2.5 km^2) are more responsive to the air temperature change, therefore have earlier ice-off dates than bigger lakes. On the Northern coastal Alaska, smaller Arctic lakes have been observed to open earlier than Teshekpuk Lake does (Arp et al., 2010; Arp et al., 2015). Given that the ice-off dates of all lakes are synchronized with that of Teshekpuk Lake, we consequently speculate that the lake ice-off impacts would propagate more broadly if all the lakes on the Northern coast of Alaska are taken into account and given the independent ice-off dates.

We infer that WRF simulates a drier 70 cm soil layer in 2015 due to the permafrost thawing in WRF as 2015 is more than 3 °C higher in air temperature than 2005 during the simulation period. Free water after thawing subsides down by gravity, decreasing the soil moisture in the corresponding layer of permafrost. This speculation is verified by the increased soil moisture at the 100 cm depth. It is worth noting that WRF simulates more than 0.2 °C of warming near the

Ikpikpuk station at 70 cm depth (Figure 4.4), which is more than 200% as much as what GIPL models (Figure 4.6). The reason of such overestimation is probably because WRF's land surface scheme overlooks the different heat conductivities from the active layer to the permafrost. This overly warmed soil leads to unrealistic permafrost thawing and active layer depth (at least 70 cm in WRF), while the observed active layer depth in most of the Arctic Alaska is less than 50 cm (Nelson et al., 1998). The deficiency in WRF-modeled soil thermal dynamics validates our use of GIPL permafrost model for the impacts of earlier lake ice-off to permafrost temperature.

The comparison between surface energy budgets unveils the energy source of permafrost warming due to the earlier lake ice-off. The surface-air temperature gradient is diminished since the near-surface atmosphere is warmed by the opened lake surface. The upwelling sensible heat flux at the surface is therefore inhibited, forcing more heat down to the subsurface. The magnitude of temperature response depends on the lake-air temperature gradient. The nature of water's high heat capacity makes the lake surface temperature change with higher inertia than the air temperature. The lake-air temperature gradient and the temperature response, therefore, rely on a substantial surface air temperature decrease. Climatologically, the daily air temperature starts to drop after passing its annual maximum in summer, which is usually between July 5th and July 15th in Arctic Alaska (Myers and Pitelka, 1979; Shulski and Wendler, 2007). We consequently infer a restricted strengthening of the lake ice-off warming impact in the future, even if the earlier trend of lake ice-off date remains or accelerates (e.g. in late June). The lake ice-off warming stays minor before the warmest day of the year, verified by the WRF-modeled temperature response before July 13th in 2005.

The ice regime shift is another factor that confines the lake ice-off warming from being stronger. Observations have found that Arctic lakes with bedfast ice regime on the northern coast of Alaska are shifting to floating ice regime because of the decreasing trend of lake ice maximum freezing depth (Arp et al., 2012; Surdu et al., 2014). Lakes with the floating ice regime melt up to one-month later than those with bedfast ice regime (Sellmann et al., 1975; Arp et al., 2011). Such lake ice regime shift acts as a negative feedback, restraining the ice-off dates of some Arctic lakes from being earlier. As mentioned above, the strength of impacts is affected minimally by the delayed ice-off, but the enlarged difference of ice-off dates among lakes may limit the propagation of lake ice warming all over the Northern coastal Alaska.

Multiple global climate projections have projected more precipitation (snowfall) in fall and winter to the Arctic Alaska (Screen et al., 2013; Alexeev et al., 2016). The enhanced snowfall results jointly from the atmospheric circulation changes, and the heat/moisture release from the opened oceanic region off the coast (Francis et al., 2009; Higgins and Cassano, 2009; Stroeve et al., 2012). The higher amount of snowfall makes a deeper insulation layer restricts retaining more heat in the subsurface in winter. Therefore we speculate the permafrost warming due to the lake ice-off to be stronger in the future while the summer atmospheric warming is speculated to pause from being more substantial.

Chapter 3 explored the Arctic sea ice decline impacts to the Arctic Alaska with a similar modeling approach, speculating that sea ice decline impacts both the near-surface atmosphere and permafrost are enhanced in late spring and early summer in the 21st century. The projected magnitude of sea ice decline warmings in late spring and early summer are comparable in magnitude to those from the lake ice-off that is found in this study (0.5-0.7 °C). Such summer sea ice decline impacts emerge in May and June, making a three-month extra warming period if combining with the lake ice-off impacts in July. Even so, the lake ice-off impacts to the Arctic Alaska are much weaker than the sea ice decline impacts. The sea ice decline impacts are the largest in late fall and early winter, which is about 6 times stronger (3-4 °C) than the lake ice-off impacts in this study.

4.5 Conclusion

In order to explore the impacts of earlier lake ice-off on the Northern coastal Alaska, WRF sensitivity experiments are conducted, motivated by the observed correlation between Teshekpuk lake ice-off dates and the permafrost temperature nearby. By removing lake ice cover and adjusting lake surface temperature, both the air and permafrost temperatures, as well as the atmospheric humidity, are found to increase on the downwind side of lakes. The wind direction plays an important role in determining the regions of impact. The upwelling sensible heat flux is inhibited by the reduced surface-air temperature gradient, forcing more heat down to the subsurface for the permafrost warming. Substantial lake-air temperature gradient and the lake ice-off impacts require the air temperature drop after the hottest day of a year, usually in early- or mid-July. Therefore the strengthening of the lake ice-off impacts to the atmosphere is speculated to be restricted, even if the earlier trend of the lake ice-off date remains or accelerates in the future. The permafrost warming effect, however, is speculated to enhance as the projected more snowfall during winter on the Northern coastal Alaska. The lake ice-off impacts are comparable in magnitudes to the sea ice decline impacts in late spring and early summer that is projected to be evident in the future, while they are still much weaker in strength compared to the overall sea ice decline impacts.

Acknowledgements

This research is funded by National Science Foundation ARC-1107481 and ARC-1417300. We thank Frank E. Urban for his help in obtaining ground temperature observation data. We thank Uma Bhatt and Anna Liljedahl for their valuable comments and suggestions as Lei Cai's graduate committee members. Any use of trade, product, or firm names is for descriptive purposes only and does not imply endorsement by the U.S. Government. In terms of authors' contribution, Lei Cai sets the scope of work, conducts the numerical computation, does data analysis, and drafts the manuscript. Vladimir Alexeev, Christopher Arp, and Benjamin Jones set the design of the work, give critical ideas and revision comments on data analysis and manuscript writing.

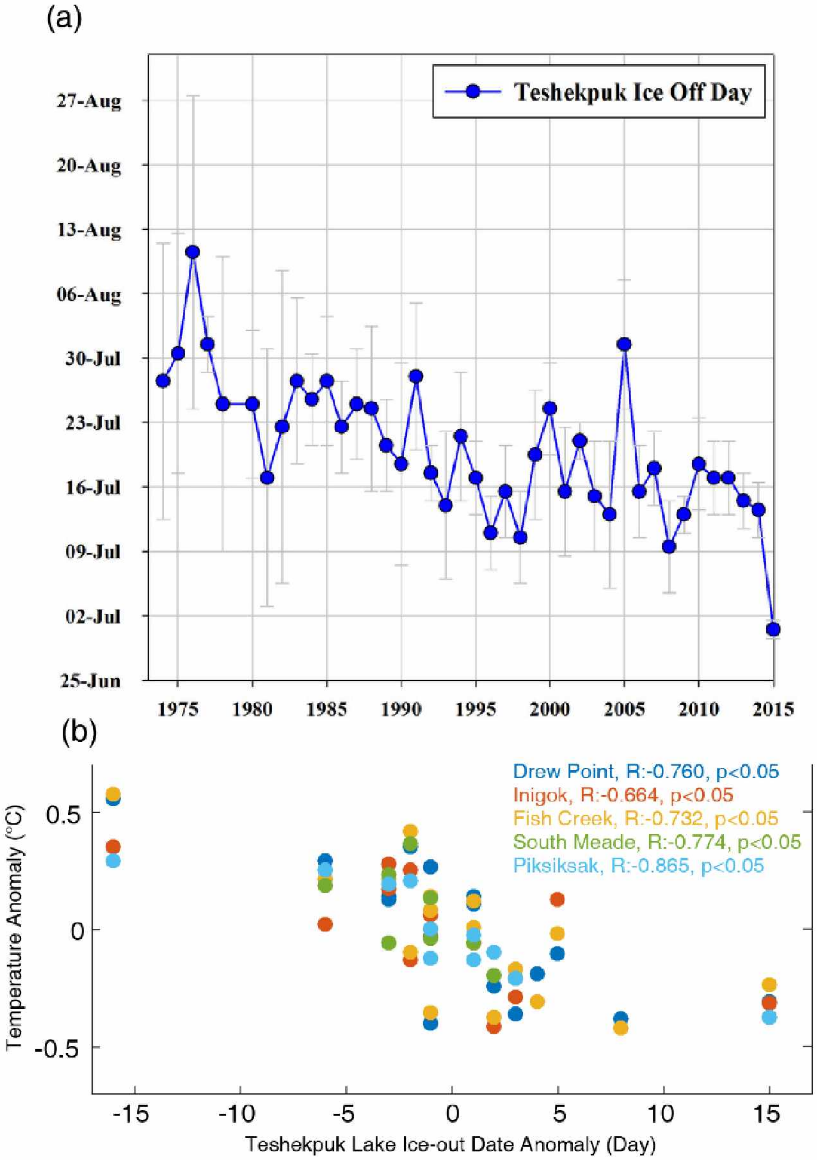

Figure 4.1. (a) Teshekpuk Lake ice-off dates interpreted from satellite observations. (b) The relationships between 70 cm soil temperature anomalies (°C) at the stations of Drew Point, Inigok, Fish Creek, South Meade, and Piksiksak and the Teshekpuk Lake ice-off date anomalies (day). The soil temperature anomalies and Teshekpuk ice-off date anomalies are significantly (> 95 % confidence level) correlated.

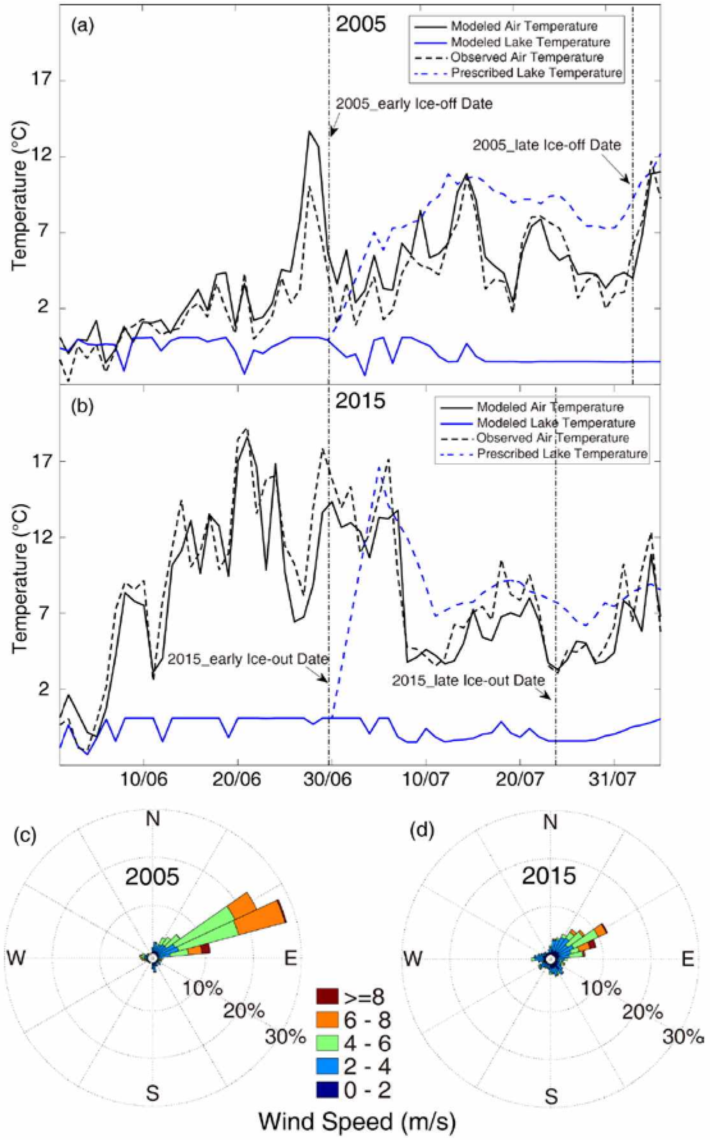

Figure 4.2. Lake temperature adjustment on Teshekpuk Lake for (a) 2005 and (b) 2015 cases. Solid black lines and blue lines are air temperature and lake surface temperature in late melt (original) cases. Black dashed lines are air temperature by observation. Blue dashed lines are time series of prescribed lake surface temperature in early melt cases. The wind rose maps averaged over Teshekpuk Lake in the simulation period in (a) 2005 and (b) 2015.

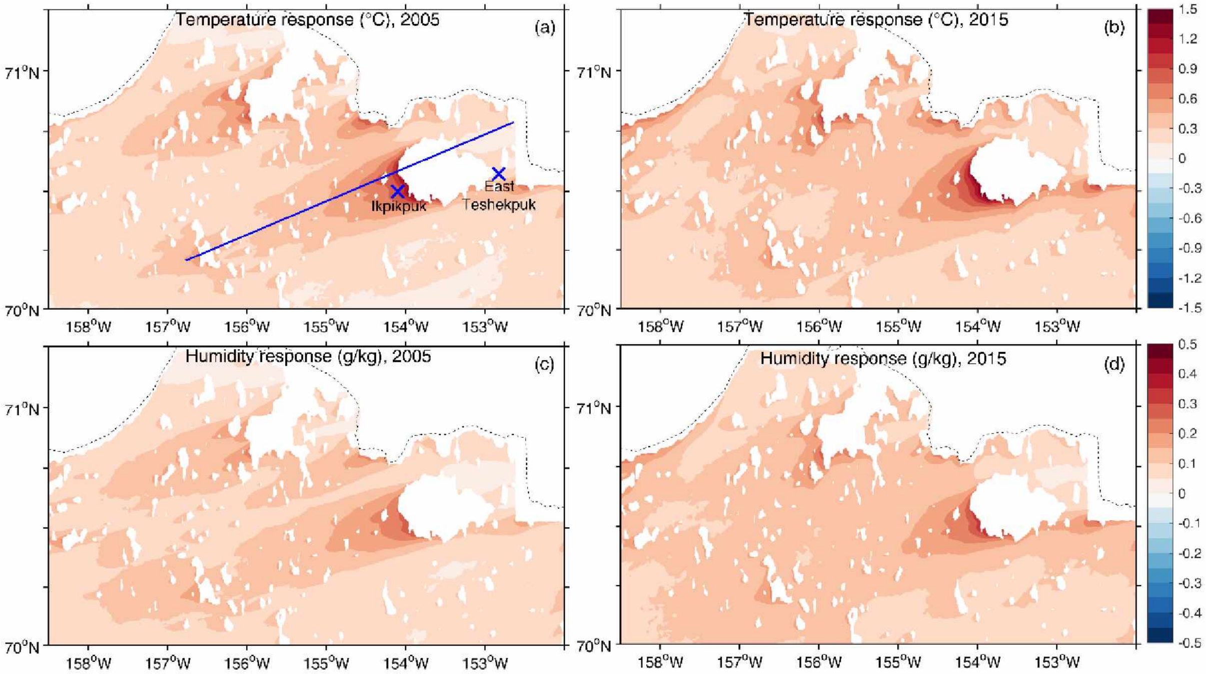

Figure 4.3. The spatial distributions of early lake ice-off responses (early melt case – late melt case) in July on (a) 2-meter temperature (°C) in 2005, (b) 2-meter temperature (°C) in 2015, (c) 2-meter humidity (g/kg) in 2005, and (d) 2-meter humidity (g/kg) in 2015. The black dotted line is the isoheight of 0 m altitude, which is used in model initialization to mask out lakes from the Arctic Ocean. Blue X marks (a) are Ikpikpuk and East Teshekpuk Stations, and the blue line is where the cross section is set for vertical profile analysis.

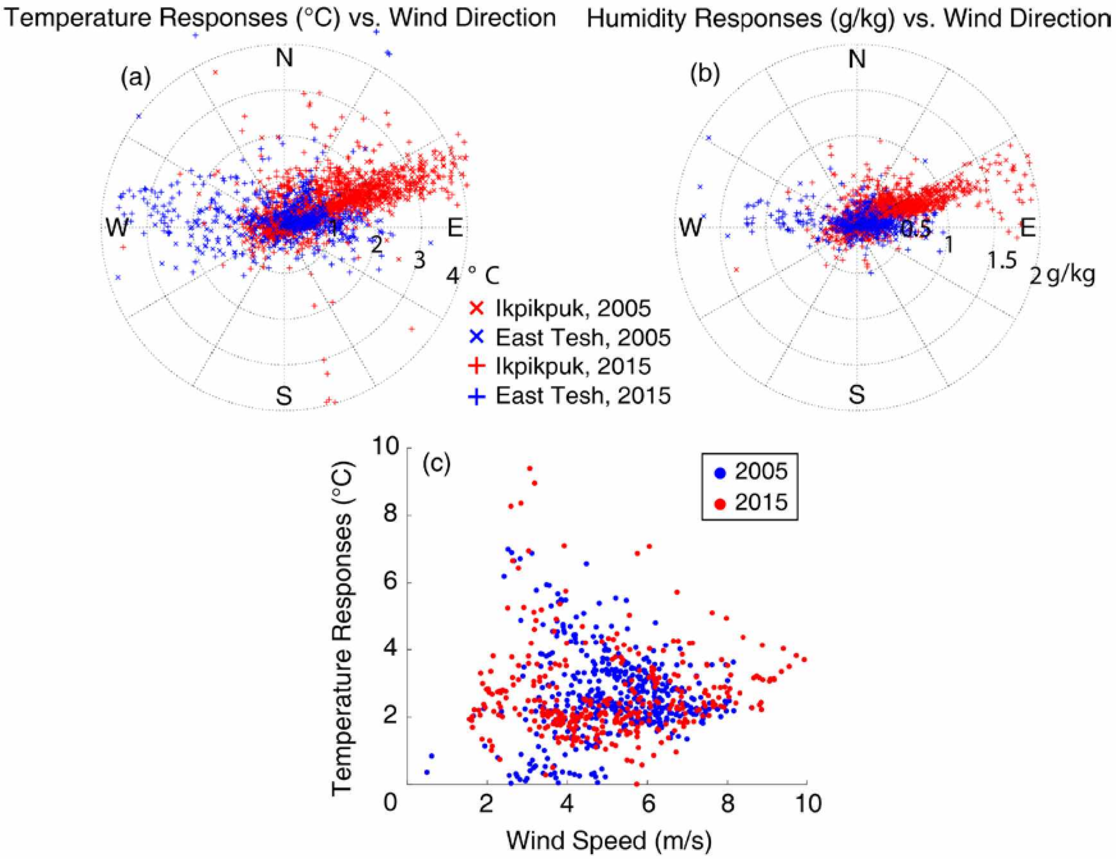

Figure 4.4. Temperature (a) and humidity responses (b) at Ikpikpuk and East Teshekpuk Lake. The locations of Ikpikpuk and East Teshekpuk are indicated as the blue X marks in Figure 3a. The most responses are when the wind blows from Teshekpuk Lake to the stations. (c) The relationship between the temperature response at Ikpikpuk to the wind speed with the favorable wind direction (ENE) in the July of 2005 and 2015.

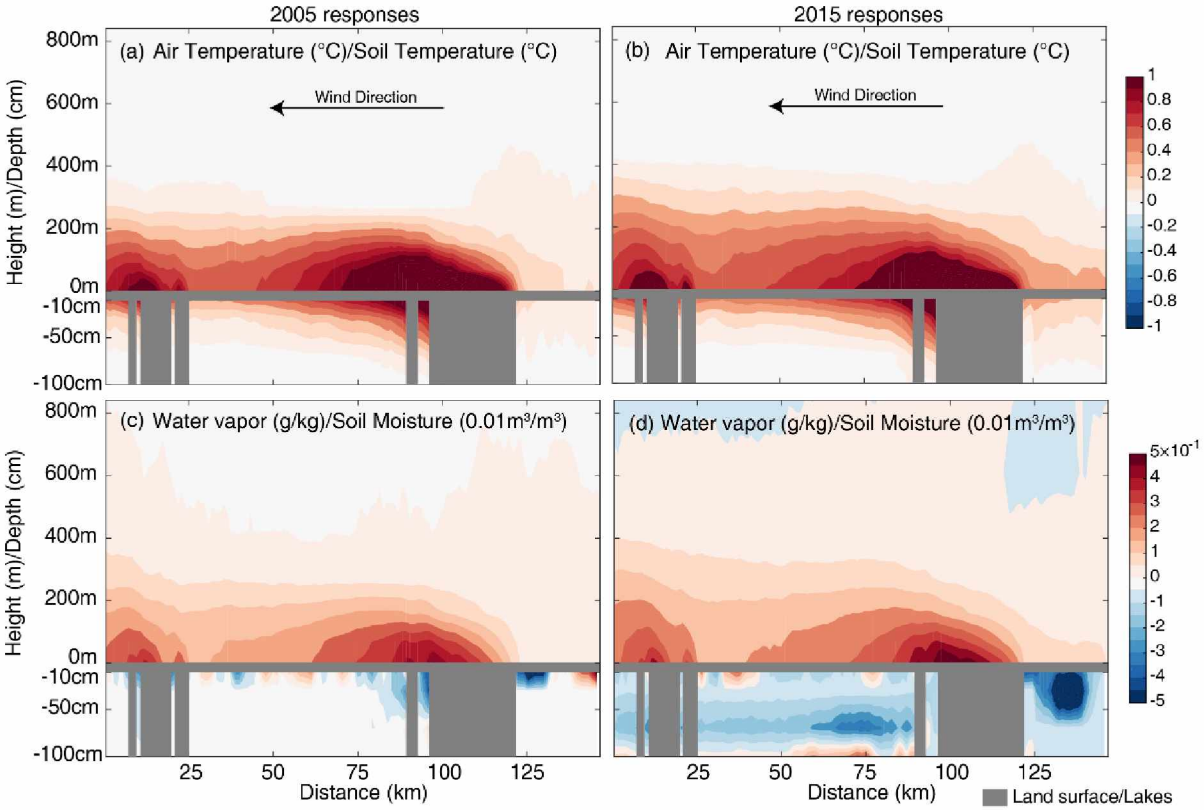

Figure 4.5. The vertical profiles on the cross-section of the earlier lake ice-off response (late melt case – early melt case) on (a) Air/soil temperature (°C) in 2005, (b) Air/soil temperature (°C) in 2015, (c) water vapor (g/kg)/soil moisture (0.01 m^3/m^3) in 2005, and (d) water vapor (g/kg) /soil moisture (0.01 m^3/m^3) in 2015. The grey blocks are where the land surface and lakes are located in the cross-section. The warming and wetting by the lake ice-off also expand in the vertical directions.

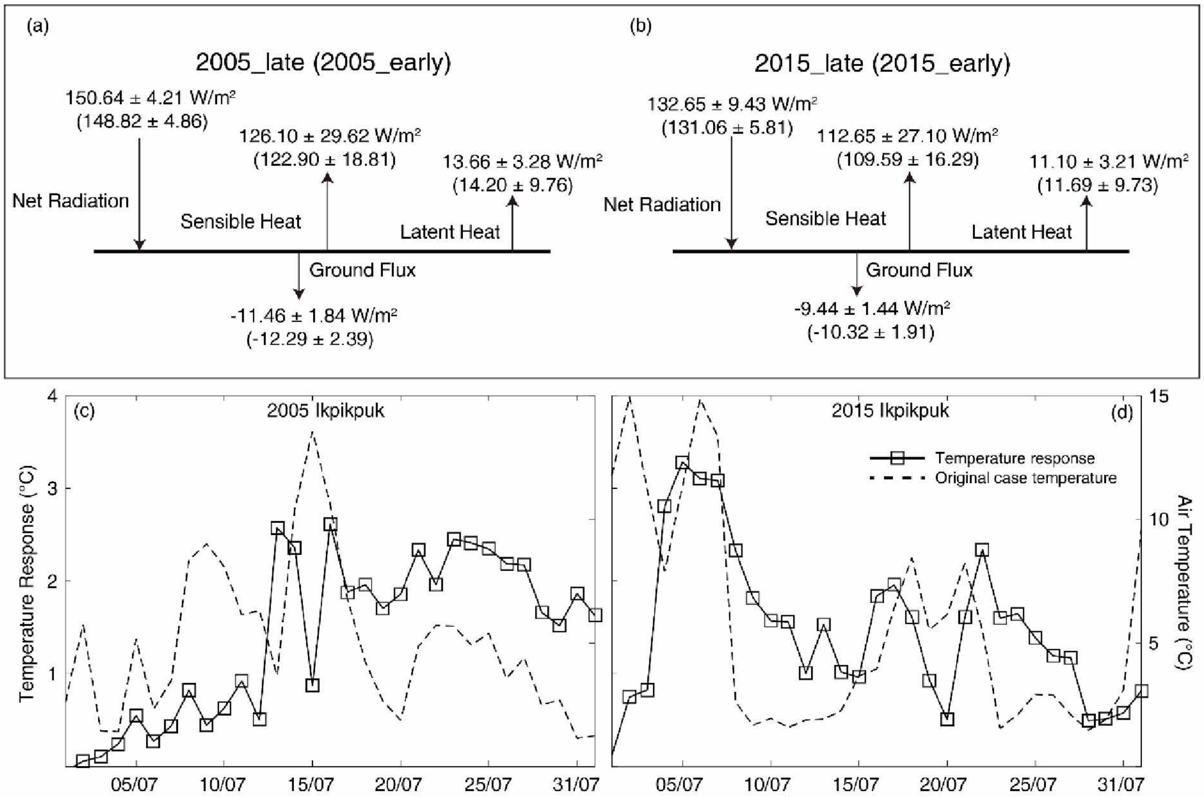

Figure 4.6. (a) The surface energy budget comparisons (W/m^2) on land within the sub-domain. (b) The time series of 2005 temperature response (°C; black solid line with squared marker) and air temperature at Ikpikpuk (°C; black dashed line). (c) The time series of 2005 temperature response (°C; black solid line with squared marker) and air temperature in original case (°C; black dashed line) at Ikpikpuk. (d) The time series of 2015 temperature response (°C; black solid line with squared marker) and air temperature in original case (°C; black dashed line) at Ikpikpuk.

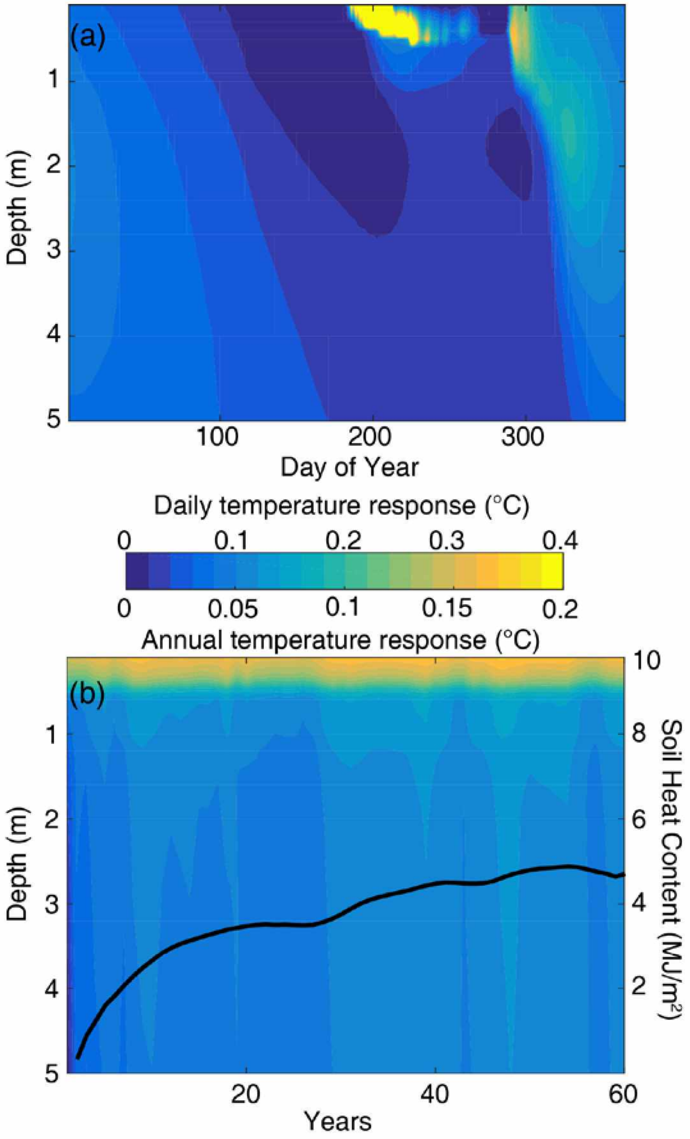

Figure 4.7 (a) The daily mean permafrost temperature response (°C) in 0-5 m. (b) The annual mean temperature response in 0-5 m from the first to the 60th year. Black curve in (b) is the accumulation of extra soil heat content absorbed by the whole column of permafrost under the corresponding snow depth scenario.

Table 4.1. WRF model cases simulated in this study.

Case Name	**Observed Ice-off Date**	**Mean Air Temperature**	**Ice-off Date in WRF boundary condition**	**Prescribed Ice-out Date**
2005_early (sensitivity)	August 1st	4.6° C	August 3rd	June 30th
2005_late (control)				August 1st
2015_early (sensitivity)	June 30th	7.7° C	July 23rd	June 30th
2015_late (control)				July 23rd

References

Alexeev, V. A., E. S. Euskirchen, J. E. Cherry, and R. C. Busey, 2015: Tundra burning in 2007–Did sea ice retreat matter? *Polar Science*, **9,** 185-195.

Alexeev, V. A., C. D. Arp, B. M. Jones, and L. Cai, 2016: Arctic sea ice decline contributes to thinning lake ice trend in northern Alaska. *Environmental Research Letters*, **11,** 074022.

Arp, C. D., B. M. Jones, F. E. Urban, and G. Grosse, 2011: Hydrogeomorphic processes of thermokarst lakes with grounded-ice and floating-ice regimes on the Arctic coastal plain, Alaska. *Hydrological Processes*, **25,** 2422-2438.

Arp, C. D., B. M. Jones, Z. Lu, and M. S. Whitman, 2012: Shifting balance of thermokarst lake ice regimes across the Arctic Coastal Plain of northern Alaska. *Geophysical Research Letters*, **39**.

Arp, C. D., B. M. Jones, J. A. Schmutz, F. E. Urban, and M. T. Jorgenson, 2010: Two mechanisms of aquatic and terrestrial habitat change along an Alaskan Arctic coastline. *Polar Biology*, **33,** 1629-1640.

Arp, C. D., B. M. Jones, A. K. Liljedahl, K. M. Hinkel, and J. A. Welker, 2015: Depth, ice thickness, and ice-out timing cause divergent hydrologic responses among Arctic lakes. *Water Resources Research*, **51,** 9379-9401.

Brown, L., and C. Duguay, 2011: The fate of lake ice in the North American Arctic. *Cryosphere*, **5,** 869-892.

Clow, G. D., 2014: Temperature data acquired from the DOI/GTN-P Deep Borehole Array on the Arctic Slope of Alaska, 1973-2013. *Earth System Science Data*, **6,** 201.

Dee, D. P., and Coauthors, 2011: The ERA-Interim reanalysis: configuration and performance of the data assimilation system. *Quarterly Journal of the Royal Meteorological Society*, **137,** 553-597.

Duguay, C. R., G. M. Flato, M. O. Jeffries, P. Ménard, K. Morris, and W. R. Rouse, 2003: Ice-cover variability on shallow lakes at high latitudes: model simulations and observations. *Hydrological Processes*, **17,** 3465-3483.

Duguay, C. R., T. D. Prowse, B. R. Bonsal, R. D. Brown, M. P. Lacroix, and P. Ménard, 2006: Recent trends in Canadian lake ice cover. *Hydrological Processes*, **20,** 781-801.

DuVivier, A. K., and J. J. Cassano, 2013: Evaluation of WRF Model Resolution on Simulated Mesoscale Winds and Surface Fluxes near Greenland. *Monthly Weather Review*, **141,** 941-963.

Förster, K., G. Meon, and U. Strasser, 2014: Modelling of snow processes in catchment hydrology by means of downscaled WRF meteorological data fields. *Hydrology and Earth System Sciences Discussions*, **11,** 4063-4102.

Francis, J. A., W. Chan, D. J. Leathers, J. R. Miller, and D. E. Veron, 2009: Winter Northern Hemisphere weather patterns remember summer Arctic sea-ice extent. *Geophysical Research Letters*, **36**.

Fry, J. A., and Coauthors, 2011: Completion of the 2006 national land cover database for the conterminous United States. *Photogrammetric engineering and remote sensing*, **77,** 858-864.

Glisan, J. M., and W. J. Gutowski, 2014: WRF summer extreme daily precipitation over the CORDEX Arctic. *Journal of Geophysical Research: Atmospheres*, **119,** 1720-1732.

Grosse, G., B. Jones, and C. Arp, 2013: Thermokarst lakes, drainage, and drained basins.

Higgins, M. E., and J. J. Cassano, 2009: Impacts of reduced sea ice on winter Arctic atmospheric circulation, precipitation, and temperature. *Journal of Geophysical Research: Atmospheres*, **114**.

Hines, K. M., D. H. Bromwich, M. Barlage, and A. G. Slater, 2009: Arctic land simulations with Polar WRF. *Preprints, 10th Conf Polar Meteorology and Oceanography*, 17-21.

Iacono, M. J., E. J. Mlawer, S. A. Clough, and J.-J. Morcrette, 2000: Impact of an improved longwave radiation model, RRTM, on the energy budget and thermodynamic properties of the NCAR community climate model, CCM3. Journal of geophysical research, **105**, 14873-14890.

Marchenko, S., V. Romanovsky, and G. Tipenko, 2008: Numerical modeling of spatial permafrost dynamics in Alaska. *Proceedings of the ninth international conference on permafrost*, Institute of Northern Engineering, University of Alaska Fairbanks, 1125-1130.

Morris, K., M. Jeffries, and C. Duguay, 2005: Model simulation of the effects of climate variability and change on lake ice in central Alaska, USA. *Annals of Glaciology*, **40,** 113-118.

Morrison, H., J. Curry, and V. Khvorostyanov, 2005: A new double-moment microphysics parameterization for application in cloud and climate models. Part I: Description. Journal of the Atmospheric Sciences, **62**, 1665-1677.

Myers, J., and F. Pitelka, 1979: Variations in summer temperature patterns near Barrow, Alaska: Analysis and ecological interpretation. *Arctic and Alpine Research*, 131-144.

Nakanishi, M., and H. Niino, 2004: An improved Mellor–Yamada level-3 model with condensation physics: Its design and verification. Boundary-layer meteorology, **112**, 1-31.

Nelson, F., K. Hinkel, N. Shiklomanov, G. Mueller, L. Miller, and D. Walker, 1998: Active-layer thickness in north central Alaska: Systematic sampling, scale, and spatial autocorrelation. *Journal of Geophysical Research: Atmospheres*, **103,** 28963-28973.

Porter, D. F., J. J. Cassano, and M. C. Serreze, 2012: Local and large-scale atmospheric responses to reduced Arctic sea ice and ocean warming in the WRF model. *Journal of Geophysical Research*, **117**.

Prowse, T., and Coauthors, 2011: Effects of changes in arctic lake and river ice. *AMBIO: A Journal of the Human Environment*, 63-74.

Rouse, W. R., and Coauthors, 2005: The role of northern lakes in a regional energy balance. *Journal of Hydrometeorology*, **6,** 291-305.

Screen, J. A., I. Simmonds, C. Deser, and R. Tomas, 2013: The Atmospheric Response to Three Decades of Observed Arctic Sea Ice Loss. *Journal of Climate*, **26,** 1230-1248.

Sellmann, P., J. Brown, R. I. Lewellen, H. McKim, and C. Merry, 1975: The classification and geomorphic implications of thaw lakes on the Arctic Coastal Plain, Alaska.

Shulski, M., and G. Wendler, 2007: *The climate of Alaska.* University of Alaska Press.

Skamarock, W. C., and Coauthors, 2008: A description of the advanced research WRF version 3.

Šmejkalová, T., M. E. Edwards, and J. Dash, 2016: Arctic lakes show strong decadal trend in earlier spring ice-out. *Scientific Reports*, **6**.

Smith, L. C., Y. Sheng, and G. M. MacDonald, 2007: A first pan-Arctic assessment of the influence of glaciation, permafrost, topography and peatlands on northern hemisphere lake distribution. *Permafrost and Periglacial Processes*, **18,** 201-208.

Strey, S. T., W. L. Chapman, and J. E. Walsh, 2010: The 2007 sea ice minimum: Impacts on the Northern Hemisphere atmosphere in late autumn and early winter. *Journal of Geophysical Research: Atmospheres*, **115**.

Surdu, C. M., C. R. Duguay, L. C. Brown, and D. Fernández Prieto, 2014: Response of ice cover on shallow lakes of the North Slope of Alaska to contemporary climate conditions (1950-2011): radar remote-sensing and numerical modeling data analysis. *The Cryosphere*, **8,** 167-180.

Urban, F. E., and G. D. Clow, 2014: DOI/GTN-P climate and active-layer data acquired in the National Petroleum Reserve–Alaska and the Arctic National Wildlife Refuge, 1998–2011. *US Geological Survey Data Series*, **812**.

Zhang, T., and M. Jeffries, 2000: Modeling interdecadal variations of lake-ice thickness and sensitivity to climatic change in northernmost Alaska. *Annals of Glaciology*, **31,** 339-347.

Appendix C

The simulation domain (red box in Figure C-1) covers most of the Arctic coastal plain of Alaska. Its north boundary is in the Arctic Ocean, and the south boundary goes across the Brooks Range. Parameterization schemes of this WRF simulation were carefully assembled together to favor this extremely high-resolution simulation. Morrison double-moment scheme parameterized microphysics processes (Morrison et al., 2005). An upgraded Rapid Radiative Transfer Model (RRTM) with new settings on random cloud overlap and trace gas concentrations called RRTMG was used on parameterizations of both longwave and shortwave radiations (Iacono et al., 2000). Both surface and planetary boundary layer (PBL) physics were parameterized based on Mellor-Yamada Nakanishi and Niino (MYNN) PBL model (Nakanishi and Niino, 2004).

The observed results for the relationship between the lake surface temperature and surface air temperature after ice-off are documented in Figure C-2, based on which the lake surface temperature adjustment algorithm is developed. Substantial lake-air temperature gradient happens when the air temperature drops.

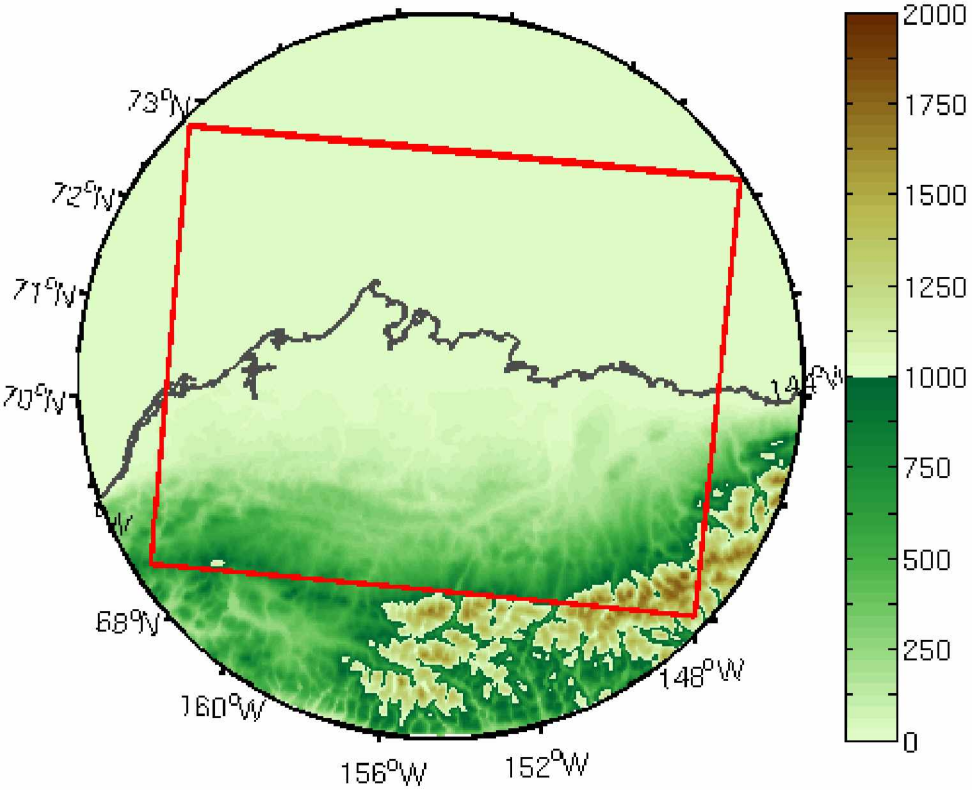

Figure C-1.The WRF simulation domain with topography (m).

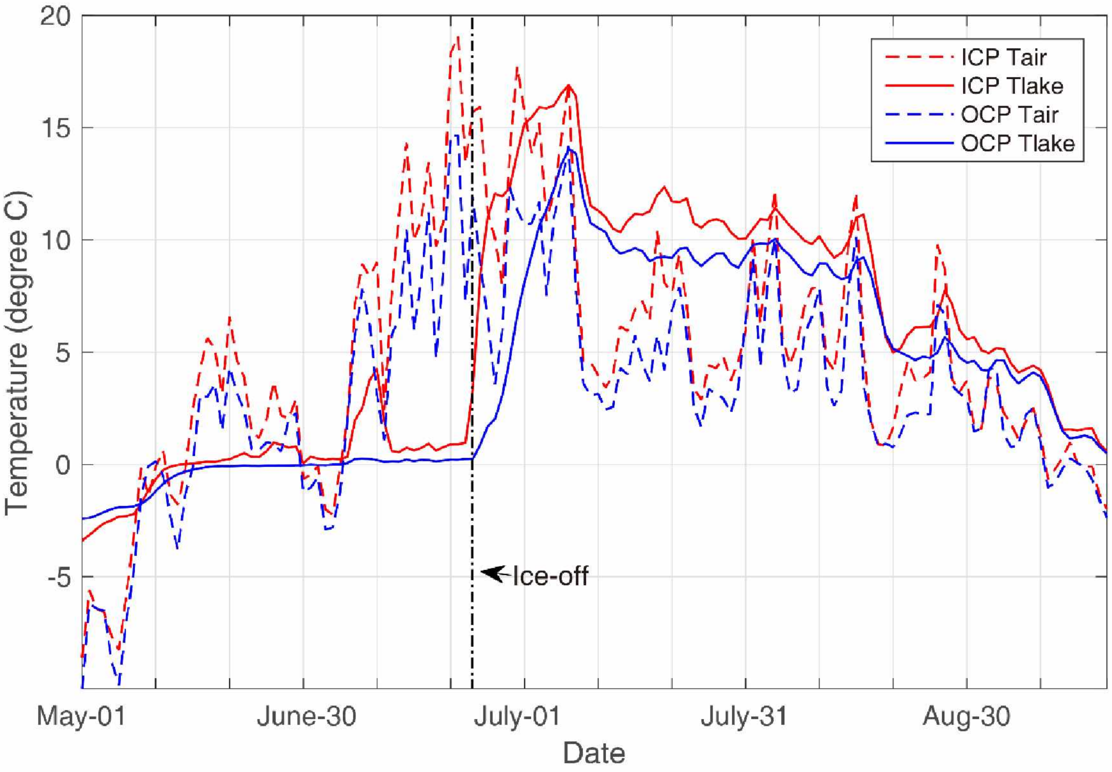

Figure C-2. The observed lake surface temperature and surface air temperature in the summer of 2015 over two lakes located in the Outer Coastal Plain (OCP) and Inner Coastal Plain (ICP) of Alaska.

Chapter 5 Patterns, Impacts, and Projections of Summer variabilities in the Arctic from CMIP5 Models[4]

Abstract

A total of 12 global climate models in Coupled Model Intercomparison Project phase 5 (CMIP5) are evaluated for their performances in reproducing two major summertime atmospheric circulation patterns in the Arctic, the Arctic Oscillation (AO) and the Arctic Dipole (AD). The reference AO and AD are extracted from the ERA-Interim reanalysis dataset period spanning 1979-2016. Model evaluation is conducted based on the historical period of 1901-2005, for which each of the 12 models is ranked by a combined metrics approach based on four parameters - two Pattern Correlation Coefficients (PCCs) and two explained variances, for the AO and AD respectively. Models with higher spatial resolutions typically have higher PCCs for the patterns of air temperature and precipitation anomalies regressed onto the summertime AO and AD. In the projected period (2006-2100), most models produce a positive trend for the AO index and a negative trend for the AD index in summer. The higher-ranked models present a greater degree of consistency in the magnitude of trend than lower-ranked ones for both the AO and AD. The best models also present the smallest trend magnitudes for both the AO and AD. The projected trends in the AO and AD jointly result in a slowdown of air temperature increase and an acceleration of precipitation increase in the 21st century over Arctic Alaska and the adjacent Arctic Ocean, and result in opposite trends in the corresponding fields over the Barents and the Kara Seas. Both the AO and AD in summer produce stronger impacts on the spatial asymmetry of the precipitation regression field than that of the air temperature field. The AD plays a bigger role than the AO in the formation of those asymmetries on pan-Arctic scale.

5.1 Introduction

Two leading modes: the Arctic Oscillation (AO) and the Arctic Dipole (AD), contribute the most to the large-scale atmospheric circulation over the Arctic in summer (June-July-August, JJA). Both variability modes are derived from applying the Empirical Orthogonal Function (EOF) analysis to the Sea Level Pressure (SLP) anomaly field. The first EOF mode represents the AO

---

[4] Cai, L., V. A. Alexeev, J. E. Walsh, U. S. Bhatt, 2018: Patterns, Impacts, and Projections of Summer Climatic variabilities over the Arctic in CMIP5 Models. *Journal of Climate,* submitted.

that dominates the atmospheric circulations over the Arctic (Thompson and Wallace, 1998; Wu et al., 2006), while the second EOF mode represents the AD (Wu et al., 2006; Watanabe et al., 2006). Some other names and appearances for AD include the Barents Oscillation (Skeie, 2000; Tremblay, 2001), the Transpolar Drift (Gudkovich, 1961), and the Arctic Rapid change Pattern (ARP; Zhang et al., 2008b).

The AO is interpreted as the modulation in the strength of the polar vortex presented at the surface (Thompson and Wallace, 1998) and drives atmospheric mass exchange between the Arctic and the mid-latitudes by strengthening/weakening the jet stream, resulting in higher anomalies of precipitation and temperature over the mid-latitudes than the Arctic (Thompson and Wallace, 1998; Deser 2000). Compared to the annular-shaped pattern of winter AO, the summer AO has a similar pattern but smaller in size and strength (Wang and Ikeda, 2000). The negative AO in the summer and the corresponding anticyclonic wind anomaly contribute to a reduction in sea ice extent in the following September (Ogi et al., 2016). As more observations of sea ice have become available, it is apparent that the AO alone is unable to fully explain the sea ice motion driven by wind (Rigor et al., 2002; Wu et al., 2006). The circulation anomalies associated with the AD has been proposed to play a significant role in sea ice decline.

The AD is not as strong (in terms of the variance explained) nor as stable (in terms of reproducibility) as the AO. It has been demonstrated that the positive AD in summer is one of the main drivers of the sea ice decline in the Beaufort-Chukchi Seas over the last several decades (Wang et al., 2009). The positive AD in summer drives the meridional anomalous wind across the central Arctic, resulting in sea ice advection from the Pacific Sector to the Atlantic Sector of the Arctic Ocean (Wu et al., 2006; Wu et al., 2012). AD in its positive phase is also likely to result in the drier and warmer summer over the Northern coastal Alaska, and it is one of the causes of the outbreak of tundra fires in 2007 over the North Slope of Alaska (Alexeev et al., 2015). The AD was also argued to be an important driver of the rapid climate changes across the whole pan-Arctic in the first decade of 21st century (Zhang et al., 2008b).

Global Climate Models (GCMs) have become a powerful tool when studying the large-scale atmospheric circulation patterns and their climatic impacts. This study investigates whether GCMs can reasonably reproduce AO and AD pattern and the corresponding climatic impacts, focusing on a suite of models from the Coupled Model Intercomparison Project phase 5 (CMIP5; Taylor et al., 2012). The CESM working group has developed the Climate Variability Diagnoses Package (CVDP; http://www.cesm.ucar.edu/working_groups/CVC/cvdp/), evaluating all CMIP5 models for their performance on reproducing major climatic variabilities, as well as the corresponding precipitation and temperature anomalies, both seasonally and annually (Phillips et al., 2014). Given the importance of the summer atmospheric circulation patterns for Arctic climate change, the evaluation of the summer AO and AD in CMIP5 models can serve as a helpful complement of CVDP's results.

In this paper, we develop a combined metrics approach to rank the models focusing on the historical period (1901-2005) based on a total of 12 CMIP5 models. We also examine the evolution of the summer AO and AD in the projected period (2006-2100), seeking a representative ensemble of the climatic impacts of the summer AO and AD to the Arctic through the end of the 21st century. This study aims to answer the following questions:

- How well can these 12 models represent the patterns of AO and AD in summer, as well as their impacts on the temperature and precipitation fields over the Arctic?
- Do model-produced patterns and climatic impacts of the summertime AO and AD change in the 21st century? If so, do these changes depend on models' performance during the historical period?
- How do the AO and AD in the summer jointly contribute to shaping the Arctic climate change in the 21st century? Which climatic mode plays a more important role?

5.2 Methodology

5.2.1 Reanalysis data and CMIP5 model products selection

Climatologically, the AO and AD are derived from applying EOF analysis to Sea Level Pressure (SLP) anomalies (typically monthly-averaged). The AO is defined as the first EOF mode of the area-weighted (multiplied by square root of the cosine of latitude) SLP anomalies over the region poleward of 20°N (-180°~180°, 20°~90°N) (Thompson and Wallace, 1998). The AD usually appears in the 2nd EOF mode of analysis performed with SLP field and calculated in the same way as AO but over a smaller region (poleward of 60°N) (Watanabe et al., 2006). The corresponding modes (the 1st and 2nd) of the principal components (PCs) represent the time series (indices) of the AO and the AD. Since the AD is defined over a smaller region, it is a more "Arctic-focused" climatic variability than AO.

In this study, we evaluate CMIP5 models with ERA-Interim reanalysis (Dee et al., 2011) taken as a reference, while some previous studies employed datasets with longer temporal coverages, e.g. NCEP/NCAR reanalysis (Deser 2000; Kistler et al., 2001; Stoner et al., 2009; Overland et al., 2012). ERA-Interim has a temporal coverage 30 years shorter than NCEP/NCAR reanalysis has, but they produce nearly identical summertime (from June to August; JJA) AO and AD indices for the period of 1979-2016 (Figure 5.1). Both datasets produce a negative trend for AO index and a positive trend for AD index in general. The AO and AD in ERA-Interim explain 26.5 % and 14.3 % of the total variance in summer SLP anomaly, respectively. The patterns and explained variances of AO and AD in NCEP/NCAR reanalysis product are not shown, as they are also very similar to those in ERA-Interim. The higher spatial resolution (T255, roughly 80 km) and the advanced 4D-Var data assimilation set the foundation for ERA-interim to retrieve accurate precipitation and temperature fields in Arctic (Lindsay et al., 2014), which is essential for this study, in addition to reproducing the patterns of the AO and AD.

Twelve CMIP5 models are evaluated over the historical period from 1901 to 2005 (Table 5.1). These 12 models have the highest scores according to CVDP evaluations based on monthly Pacific Decadal Oscillation (PDO) and Atlantic Multidecadal Oscillation (AMO). CVDP doesn't score AO in summer (June-July-August, JJA), although it is substantially different from AO in winter (Ogi et al., 2016). We only employ the first ensemble member of all 12 models for a consistent comparison. The first ensemble member of Representative Concentration Pathway 8.5 (RCP8.5) projections of the same 12 models are also downloaded for assessing the evolution of the summertime AO and AD in the 21st century. The CMIP5 model data is downloaded from the Earth System Grid Federation (ESGF) node at Lawrence Livermore National Laboratory (https://esgf-node.llnl.gov/projects/esgf-llnl/).

5.2.2 The calculation of AO/AD in CMIP5 models

The AO, the dominant mode of climatic variability in Arctic, consistently appears as the first EOF. However, the AD may not appear until the 3rd or 4th EOF mode for some models, in which case the explained variance is typically low. We therefore retrieve the AO consistently as the first EOF, while searching for a dipole-shaped pattern in the second to fifth modes for the AD. Each of the models produces its own AO and AD (as we will see later in the text) having geographically differing patterns, which makes comparison of the corresponding PCs with reanalysis results, also across models, difficult if not impossible. In order to avoid this problem, time series of model-produced AO/AD indices are obtained by regressing the summer SLP anomalies in CMIP5 models onto the first (for the AO) and second (for the AD) EOF modes of summer SLP anomalies in ERA-Interim reanalysis. Defining the model-produced AO/AD indices this way instead of using the PCs obtained from performing EOF analysis on each of the individual models will allow the comparison of model-generated AO/AD indices with ERA Interim in a consistent manner. This will also allow consistency when comparing the response in other fields (precipitation, temperature) to the same SLP anomaly. The impacts of AO/AD on precipitation and temperature fields are calculated by regressing the AO/AD indices onto the anomalies of precipitation and temperature. Bilinear interpolation is performed in order to project models' SLP fields onto ERA-Interim's grid before applying the procedure described above.

5.2.3 The evaluation method

We rank the models by introducing the Pattern Correlation Coefficient (PCC), along with the explained variance from the EOF analysis. The PCC, which sometimes is also called the Anomaly Correlation Coefficient (ACC), quantifies the similarity of a pair of gridded spatial patterns, and it has been widely applied to evaluate the numerical weather forecast skill. Langland and Maue (2012) employed this approach to compare forecast skills of multiple numerical weather prediction systems in forecasting AO in the winter. In this study, the model-produced pattern is bi-linearly interpolated onto the ERA-Interim grid for calculating the PCC using the following formula

$$PCC = \frac{\sum_{i=1}^{N} F_i \cdot R_i}{[\sum_{i=1}^{N}(F_i)^2 \cdot \sum_{i=1}^{N}(R_i)^2]^{1/2}} \quad (1)$$

in which Fi and Ri are respectively the variable of interest in a CMIP5 model and the corresponding ERA-Interim reanalysis data variable in a grid point, respectively. It is worth noting that calculating the PCC of the AO integrates a higher amount of grid points than that of the AD, as the AO pattern covers a larger region than the AD pattern. The Root-Mean-Square Error (RMSE) calculated from the errors of all grid points quantifies the difference between the model-produced pattern and the reference pattern.

A combined metrics ranking method calculates the combined deviation of the vector of multiple (N) parameters from the reference. The combined metrics score is defined by the following formula,

$$D = \sqrt{\sum_{i=1}^{N} (\Delta P_i)^2} \qquad (2)$$

in which ΔPi is the difference between the ith model parameter and the corresponding reference parameter. Before calculating the combined metric score, we normalize each of the vector components in order to equalize the weight of individual parameters. We rank models by sorting the combined metric scores from smallest to largest. The parameters involved in this combined metric ranking are the PCCs and the explained variances of AO and AD. The PCCs for ERA-Interim produced AO and AD are set to 1.

We do not include RMSE in the combined metrics ranking as RMSE is reversely correlated with the PCC. Including both PCC and RMSE gives too high a weight to the spatial pattern compared to its explained variance. The RMSE serves as a complementary parameter in the ranking that a higher rank is given to the model among the ones with the identical combined metric score but having a lower RMSE. PCCs and RMSEs are also calculated on the regressed temperature and precipitation in each model, but only to compare the similarity of spatial patterns of impacts rather than to rank the models.

5.3 Results

5.3.1 Comparison of summer AO and AD in CMIP5 historical products

The selected CMIP5 models are evaluated regarding their ability to reproduce the summertime AO and AD. PCCs and explained variances quantify the similarity between the model-produced and the reference AO and AD, to which is given a ranking score is given using the combined metrics ranking approach. The lower the combined metrics score, the better the model performs on reproducing the summer climatic variabilities over the Arctic.

5.3.1.1 Spatial pattern comparisons

According to the evaluation by CVDP (http://webext.cgd.ucar.edu/Multi-Case/CVDP_ex/CMIP5-Historical/nam.jja.png), most models are able to generally produce the annular-shaped pattern of the AO in summer with a negative anomaly center over the central Arctic and two positive anomalies over the North Pacific and the North Atlantic. Such spatial distribution is similar to that of AO in winter, only with a weaker amplitude (Ogi et al., 2016). In order to get all the quantitative parameters (PCCs, RMSEs, and explained variances) for the combined metrics ranking, we address the EOF analysis for the summertime AO by ourselves in this research,

For the AD, all 12 models are able to reproduce the dipole-shaped pattern in a certain mode (2nd to 4th mode) of EOF, while with the neutral line oriented in varied directions (Figure 5.2). Four out of twelve models (GISS-E2-R-CC, HadGEM2-AO, HadGEM2-ES, and MPI-ESM-LR), have the neutral line of anomaly oriented along the 0°E to/180°W meridian, closely resembling the EOF pattern in from ERA-Interim. The explained variances in these four models are also among the highest (>13 %). Eight out of twelve models are able to retrieve a dipole-shaped pattern of AD as the 2nd EOF mode. Three models: CESM1 (CAM5), CMCC-CMS, and NorESM1-ME have the dipole pattern in the 3rd EOF mode, with nearly as much (11-12 %) variance explained as the 8 models above. IPSL-CM5A-LR does not show the dipole-shaped pattern until the 4th EOF mode, having the explained variance as low as 4.8 %.

5.3.1.2 Model Ranking

The PCCs and the explained variances of the model-produced AO and AD are calculated and compared to the reference (ERA-Interim). As the result, most models are able to produce highly correlated (PCC > 0.8) AO spatial patterns, while they differ from each other on the explained variance (Figure 5.3a). In contrast, the model-produced AD have larger differences in the PCCs than in the explained variances (Figure 5.3b). While most models cluster together, one outlier emerges in the evaluation of both AO and AD, which is CMCC-CMS and IPSL-CM5A-LR for the AO and AD evaluations, respectively. Their scores diverge from the other models for different reasons. The summer AO pattern in CMCC-CMS has three negative anomalies: over the Aleutian Islands, the Greenland, and the Barents Sea instead of one over the central Arctic. The AD in IPSL-CM5A-LR in the 4th EOF mode has a much lower explained variance than other models.

The combined metrics ranking are conducted using two sets of PCC/explained variance of the AO and AD (Table 5.2). The 12 CMIP5 models generally produce the AO patterns with higher PCCs and smaller RMSEs than the AD patterns. HadGEM2-ES, GISS-E2-R-CC, and MPI-ESM-LR rank the top-3 models according to the combined metrics score. The two respective outliers in the AO and the AD evaluation, CMCC-CMS and IPSL-CM5A-LR, rank as the last two among the 12 models.

5.3.2 Regressed summer temperature and precipitation on historical AO and AD

As we have seen model AO and AD performance differs significantly with some models failing to reproduce the AO. This will likely have implications for the models' ability to reproduce anomalies in other fields (e.g., precipitation, air temperature) corresponding to the positive or negative phase of the oscillation of interest. In order to quantify model performance regarding the impacts of AO and AD, the summertime temperature/precipitation anomalies in models are regressed onto the AO/AD index. The similarities between the patterns of models and that of ERA-Interim are quantified based on the PCCs and RMSEs. For the temperature anomalies regressed on the AO, CMIP5 models agree with ERA-Interim with positive anomalies over the Northern Canada and the Northern Scandinavia, while having negative anomalies over the North Slope of Alaska and the Kara Sea (Figure 5.4). Models with lower PCCs typically fail to reproduce the negative anomalies in the mid-latitudes (e.g., the Eastern Siberia, the Southern Europe, and the Southern United States). ERA-Interim and the 12 models do not show any apparent temperature anomalies over the central Arctic, except for some models with small (<0.5 °C) negative anomalies over the Arctic Ocean.

For precipitation anomalies regressed on the AO, the 12-model composite and ERA-Interim both show positive precipitation anomalies (around 5 mm/month) over the Arctic Ocean (Figure 5.5). All twelve models agree on having a strip-shaped region with negative anomaly crossing the North Atlantic, Scandinavia, and all the way to the Central Siberia, which compares favorably with the ERA-Interim precipitation. Strong precipitation anomalies are visible in all 12 models and ERA-Interim over the Southern Asia and the Northwestern Pacific. Such anomalies disappear in the 12-model composite, implying that the locations of the anomalies are slightly different between models and those anomalies zero out in the mean. Models with lower PCCs typically have a negative precipitation anomaly over the Southern United States and Southern Europe, while ERA-Interim and other models with higher PCCs have a positive precipitation anomalies over the same region.

The model-produced temperature and precipitation anomalies regressed on the AO exhibit a larger signal over the mid-latitudes and sub-Arctic than over the central-Arctic, coinciding with the physical mechanism of AO, which is the modulation of the strength and wavelength of the jet stream. The slightly negative SLP anomaly in the central Arctic corresponds to the slight decrease in temperature and increase in precipitation over the Arctic Ocean. The mid-latitudes is where the most model-to-model and model-to-reanalysis disagreement occurs, such as the Southern United States and the Southern Europe. Some disagreement between models with regard to precipitation also exists over the Northwestern Pacific.

The CMIP5 models produce dipole-shaped distributions of temperature and precipitation anomalies regressed on the AD. The 120°E/60°W meridian, in general, divides the zones into the positive and the negative temperature anomalies (Figures 5.6). Positive temperature anomalies are present over Northern Siberia, Northern Alaska, and Northern Canada, while negative anomalies are located over the coastal regions of the Barents and Kara Seas. The CMIP5 models generally have similar temperature anomaly patterns to ERA-Interim along the pan-Arctic coastal region. For the central Arctic, however, nine out of twelve models disagree with the other three, as well as the ERA-Interim, present a 0.2-0.4 °C positive temperature anomaly over the Pacific sector of the Arctic Ocean.

Precipitation regressed on the AD also results in a dipole-shaped pattern for all models, having a neutral line located roughly on the 0°E/180°W meridian. Positive precipitation anomalies occur on the coasts of the Barents and Kara Seas, while negative anomalies occur over Northern Alaska, Northern Canada, and parts of Greenland. ERA-Interim gives generally a similar distribution, except contains more topographical features because of its higher spatial resolution (e.g., opposite precipitation anomalies over the Northern and the Southern foothills of the Brooks Range in Arctic Alaska). Such detailed topographical features in the ERA-Interim actually pull the PCCs down for some models that successfully capture the large-scale anomaly patterns but fail in reproducing small-scale details.

Temperature anomalies in both ERA-Interim and the models represent the workings of the AD mechanism, which is when the anomalous meridional wind accompanying the corresponding SLP anomaly brings warm air to the central Arctic and cold air to the North Atlantic. The AD pattern results from more high-pressure systems staying over the Beaufort Sea and the Northern Canada, and more low-pressure systems traveling over the Northern Eurasia. Such SLP anomalies inhibit precipitation on the North American side while enhance precipitation on the Eurasian side of the Pan-Arctic.

All 12 CMIP5 models are able to produce reasonable spatial distributions of temperature and precipitation impacts resulted from the AO and the AD in general, while the patterns differ somewhat from each other regionally. High ranking models do not always come up with high PCCs and low RMSEs for impact patterns. For example, GISS-E2-R-CC and MPI-ESM-LR, which rank as the 2nd and 3rd among the 12 models, have lower PCCs than many lower-ranked models. Models with higher spatial resolutions, like CCSM4 and CESM1, tend to produce higher PCCs, especially for precipitation. More detailed discussions are addressing this contradiction in the discussion section.

5.3.3 AO/AD in the 21st century and their impacts on Arctic climate change

After concatenating the historical and projected periods, the AO and the AD index in 12 CMIP5 models exhibit oscillations on multidecadal timescale (Figure 5.8a-b). In the projected period (2006-2100), the most apparent transition of the medians of the summer AO and AD indices in the future occurs around the 2030s. Before the 2030s, the median value of AO index generally have a decreasing trend, while that of AD index generally have an increasing trend. After the 2030s, the median of AO index turns to an increasing trend, while that of AD index to a decreasing trend. As for as each individual model, there are 11 models with overall positive AO trends and 10 models with negative AD trends (Figure 5.8c). Such agreement between models could indicate the robustness of these trends in CMIP5 models in the 21st century. The top-four models (HadGEM2-ES, GISS-E2-R-CC, MPI-ESM-LR, and MRI-ESM1) seem to be more in agreement with each other on the magnitudes of trends than the lower-ranked models. The increasing AO trend is about 0.03/decade on average, while the decreasing AD trend is just below -0.05/decade in these 4 models. The better-performing models also have smaller trend magnitudes of the summer AO and AD indices.

The composite of summer temperature and precipitation from the four top-performing models increases more rapidly across the pan-Arctic coastal region than over the central Arctic (Figure 5.9a-b). Summer temperature over the pan-Arctic coast increases at a rate greater than 0.5° C/decade, while it is about 0.2° C/decade over the Arctic Ocean. The most rapid temperature increase (0.8° C/decade) is over the Barents and the Kara Seas. The monthly precipitation increases at a rate of at least 1 mm/decade for the whole Arctic, while for some regions like the Interior Alaska, coastal Greenland, Scandinavia, and North-Central Siberia, the increasing rate can be up to 4 mm/decade.

Such spatially uneven distributions of temperature and precipitation increase can be partially explained by the impacts of the projected long-term AO and AD trends in the 21st century. Figure 5.9c-f displays the four best-performing models' composites of summer temperature and precipitation anomalies regressed on the 21st-century AO and AD. The patterns of the regressed temperature and precipitation in RCP8.5 projections generally resembles those from the historical period (Figure 5.4-5.7). We defined two regions of interest (The black-line delimited regions in Figure 5.9c-f): Arctic Alaska (130°-170° W, 66°-75° N) and the Barents Sea (30°-75° E, 63°-80° N), which have the fastest summer precipitation and temperature increases, respectively (Figure 5.9a-b), and are significantly influenced by the AO and AD (Figure 5.4-5.7). The impact of the long-term change of the AO/AD index to temperature/precipitation is calculated by multiplying the trend of AO/AD and the regressed temperature/precipitation anomaly. The comparison between such impacts and the overall changes of temperature and precipitation (Figure 5.9a-b) gives the relative contributions by the AO and AD within the regions of interest (Percentages in Figure 5.9c-f).

As a result, AO's contribution to both the temperature and precipitation increases in both regions can be considered as minor. Only less than 1% (0.6±0.2% and 0.4±0.1%) of summer temperature increase results from the AO for both regions. It is worth noting that the AO trend actually affects the temperature change oppositely over terrestrial and oceanic regions in the sub-domain of Arctic Alaska. The trend of AO leads to a temperature decrease (negative percentage) over the land (Northern Alaska), while a temperature increase (positive percentage) over the ocean. The AO contributes to the precipitation increase at a higher rate than to the temperature increase. The trend of AO contributes to the precipitation increase over the Barents Sea slightly and with high uncertainty (1.3±3.6 %), while it's quite certain that the trend of AO is responsible for around 6 % (6.1±0.6 %) of precipitation increase over the Arctic Alaska.

The trend of the AD impacts the temperature and precipitation oppositely in the two regions of interest. The AD results in -3.1±1.7% of the summer temperature change over the Arctic Alaska, meaning the trend of the AD favors a decrease of temperature in this area. Over the Barents Sea, the AD trend facilitates the temperature increase in summer contributing 5.1±0.2% of the total warming. The summer AD decreases precipitation for 34.4±5.2% of the overall rate of precipitation change over the Barents Sea, while it is responsible for 8.7±4.2% of precipitation increase over the Arctic Alaska

5.4 Discussion

Climate variations are characterized in terms of the repeated patterns and cycles, which represent the internal variability in the coupled GCMs (Phillips et al., 2014). These patterns and cycles have implications for the future changes of climate condition, which is why the ability to reproduce climatic variabilities has become an important factor in GCM evaluation (Stoner et al., 2009). Specifically for the AO and AD, they represent the mass and heat exchange between the Arctic and the mid-latitudes, playing an important role in the linkage of the Arctic and global climate changes (Deser 2000; Wu et al., 2008). CVDP only quantifies PCCs/RMSEs of the wintertime AO, which is why other than evaluating the summer AD, we also explore whether a certain CMIP5 model performs consistently in reproducing the AO in the summer and winter. Both the AO and AD represent major modes of variability in the Arctic. Besides, AD was not analyzed to a great extent in CMIP5 models. Our quantitative evaluation of the AO and AD in the summer thus complements the analysis done by CVDP. According to CVDP, all 12 models we selected are able to reproduce the winter AO patterns with PCC > 0.87, and 8 of which with PCC > 0.9. The CMCC-CMS fails to reproduce a reasonable AO pattern in summer (PCC = 0.225) and is one of the best models in terms of the AO pattern in winter (PCC = 0.97). This comparison illustrates the fact that a model's performance for the same climatic mode of variability can vary by the season of extraction, and it is typically more difficult to reproduce weaker climatic variations, (e.g., the summer AO and the summer AD). A threshold of PCC = 0.6 is interpreted as the lower limit of a practical forecast when PCC was firstly introduced to evaluate the forecast skill (Hollingsworth et al., 1980). Eight of twelve models, in this case, meet such standard, retrieving a reasonable summer AD pattern, which as mentioned above was overlooked in previous CMIP5 model evaluations. We skip the evaluation of the variability of the summertime AO and AD indices and excluded them from ranking, as we have hardly found any agreement between models' power spectra of the summer AO and AD. Stoner et al., (2009) have found it much harder for CMIP3 models to reproduce the temporal spectra of indices than to reproduce the corresponding spatial patterns of climatic variability. Analysis done in this study indicates that a similar problem remains in the CMIP5 models, in our case for the two less active variabilities of the summertime AO and AD.

We include the explained variances in the model evaluation, while CVDP focuses only on PCCs/RMSEs. The reason is probably that CVDP needs a universal approach that is also applicable for other variabilities irrelevant to the EOF analysis, such as the ENSO (El-Niño Southern Oscillation) and the AMO. A more focused scope of this study enables us to emphasize the importance of the explained variance, which mathematically describes the relative contribution of each individual EOF mode to the anomaly field. A reasonable percentage of explained variance is as important as the spatial pattern, which is especially true for AD that may not appear in the 2nd EOF mode. It is also why we set the same weight to the PCC and the explained variance in the combined metric ranking, even though such equal weights may overly exaggerate the importance of explained variance.

Some top-ranked models fail to produce the regressed temperature/precipitation patterns corresponding to anomalous AO and AD situations compared to those in the ERA-Interim. We speculate it arises to a large extent from the coarser grid spacing of CMIP5 models compared to the spatial resolution of ERA-Interim. The atmospheric grids in these models range from 2.5×2.0 to 1.25×0.9 degrees (Table 5.1), while ERA-Interim provides the reference at a higher resolution (0.75×0.75 degrees) than all the CMIP5 models (Dee et al., 2011). CMIP5 models with higher spatial resolution tend to resolve more detailed spatial distributions of temperature and precipitation regressed on AO and AD, which are also typically more closely correlated to them by ERA-Interim. Likewise, models with lower spatial resolutions are disadvantageous in the comparison of the temperature and precipitation impacts. We, therefore, exclude temperature and precipitation impacts from the criteria to rank models.

The two-century-long composite of the model-produced summer AD index exhibits multidecadal scale oscillations (Figure 5.8b). The crest and trough of the longest oscillation occur in the 1940s and 2030s, respectively, over-imposed with oscillations with shorter cycles (20-40 years). The temporal coverages of both ERA-Interim and NCEP/NCAR reanalysis are too short to retrieve the longest oscillation, showing only monotonically increasing trends. The 20th-century reanalysis data (20CR, version 2; Compo et al., 2011), however, unveils such oscillation that the minimum of the summer AD is around the late 1930s, before which a decreasing trend back to 1871 (Figure 5.10). The 142-year length of data shows the evidence of AD's multidecadal variability in the reanalysis data, although it still fails to capture a full cycle of the longest oscillation of the summer AD index. Note that little-to-no SLP observation data is assimilated in 20CR prior to the 1930s, making the 20CR-produced AD index less trustable (Compo et al., 2011). Nevertheless, this comparison proves that a multidecadal scale oscillation of AD is produced by a variety of globally-covered modeling systems, attracting more attention on studying the dynamics and physical mechanisms of AD.

Applying EOF analysis over the extended region 20°~90°N, a dipole-shaped pattern representing the AD remains in the central Arctic as the third or fourth mode (depending on the product and period chosen). Two extra SLP anomaly centers are over the South of the Bering Strait and the Fram Strait, respectively. The AMO and PDO are the two major climatic variabilities with decadal to multidecadal scales of oscillation over these two target regions. Given the fact that the AD pattern presents anomalous wind connecting the Bering Strait and Fram Strait, AMO and PDO may have the potential of driving the phase and strength of the AD, about which very few studies have been taken place. As we have verified that a large number of the CMIP5 models are able to reproduce a reasonable dynamics of the AD, conducting sensitivity experiments using global climate models is potentially one way to address this hypothesis.

The AO and AD, as well as their climatic impacts, are mathematically independent from each other due to the nature of EOF analysis that decomposes the anomaly field into orthogonal modes of eigenvector/eigenvalue. The relative contributions of the AO and AD to the projected Arctic climate change are, therefore, able to be compared. The long-term trends of the summertime AO and AD indices jointly generate stronger impacts on precipitation than on temperature in the 21st century. Among the two modes of variability, the AD plays a bigger role than AO in imposing contrasting trends in temperature and precipitation. In terms of overall climate change over the pan-Arctic in summer, the temperature increases faster over the Barents Sea than over the Arctic Alaska, while the precipitation increases more rapidly over the Arctic Alaska than over the Barents Sea (Figure 5.9a and 5.9b). Even so, the global warming signal remains a dominant contributing factor of climate change in summer over the pan-Arctic.

In the summer of 2007, the rapid sea ice loss was associated with a strong positive AD, opening a large oceanic water body over the Chukchi and the Beaufort Seas. Several studies have found that the trans-polar anomalous wind by the positive AD drives sea ice export from Chukchi-Eastern Siberia regions (Zhang et al., 2008a; Wang et al., 2009; Overland et al., 2012). A model-based study by Zhang et al. (2008a), however, brought up that only 30 % of the sea ice retreat is attributed to the sea ice advection, while 70% of that is resulted from the amplified melting of sea ice, which is due to the preconditioning of thin sea ice and the sea surface heating. Steele et al. (2010) further indicated that the solar radiation is the main contributor (80%) to such amplified sea ice melting in the Beaufort-Chukchi Seas. In agreement, anomalously low cloudiness was observed by both ground and satellite observations over the Pacific Sector of the Arctic Ocean in the summer of 2007 (Kay et al., 2008 and 2009).

The total cloud fraction and the sea ice concentration in summer from 1979 to 2016 in both ERA-Interim and NCEP/NCAR reanalysis data are regressed onto their corresponding reanalysis dataset. It shows that the positive AD is linked to the reduction of total cloud fraction and sea ice concentration over the Pacific Sector of the Arctic Ocean (Figure 5.11a to 5.11d). The same association is generally presented in the best 4 CMIP5 models ranked by us in the RCP8.5 projection from 2006 to 2050 (Figure 5.11e to 5.11f). We skip the second half of the 21st century, as some models in RCP8.5 scenario project close-to-zero summer sea ice cover after 2050, making the AD-induced sea ice advection meaningless (Collins et al., 2013). Regions with the significant agreement between the 4 models are very limited, especially for the total cloud cover, implying a plenty of potential for earth system models to improve in the sea-air coupled processes.

5.5 Conclusions

This study evaluates the performance of 12 CMIP5 models to reproduce the AO and AD in summer. Eleven out of twelve models reproduce reasonable AO patterns in summer, although their pattern correlation coefficients to the reference are not as high as their AO patterns in winter. All 12 models are able to retrieve dipole-shaped patterns of the AD in summer, and eight models identify the AD in the 2nd EOF as in the reference. The combined metrics ranking approach involves both the PCC and the explained variance of both the AO and AD, ranking GISS-E2-R-CC, HadGEM2-ES, and MPI-ESM1-LR as the best three models. CMCC-CMS and IPSL-CM5A-LR are ranked as the last two, as their performances diverge from the other models' respectively on reproducing the AO and AD. Highly-ranked models are able to retrieve the large-scale temperature and precipitation impacts from the AO and AD, while more detailed distributions of impacts are limited by the coarse spatial resolution for some models (e.g. GISS-E2-R-CC). Generally, the positive summer AO brings more temperature and precipitation anomalies to the mid-high latitudes than to the central Arctic, while the positive summer AD results in dipole-shaped patterns of temperature and precipitation impacts. After concatenating the historical period and the RCP8.5 projection, the two-century-long time series of the model-produced AO and AD index show multidecadal scale oscillations. The monotonically increasing AO and decreasing AD appear after the 2030s in the 12-model composites. The highly-ranked models show more consistency on such positive trend of AO and negative trend of AD.

In the 21st century, the top-four CMIP5 models project increases of both summertime air temperature and precipitation over the pan-Arctic (poleward of 60° N) under the RCP8.5 scenario. For Arctic Alaska, the air temperature increases more slowly while the precipitation increases faster, than the surrounding Beringia regions in summer. On the other hand, the Barents Sea is the region with the fastest air temperature increase and the slowest precipitation increase around the pan-Arctic in summer. Such spatial unevenness of climate change in Arctic is partially attributed to the changes of the AO and AD indices in the 21st century. Compared to the AO, the AD variability displays larger spatial variability of temperature and precipitation in summer within the pan-Arctic regions, playing a more important role in influencing the climate change in pan-Arctic regions.

Acknowledgements

This study is funded by Cooperative Institute for Alaska Research through the University of Alaska Fairbanks Global Change Student Research Grant. In terms of authors' contribution, Lei Cai sets the scope of work, conducts the numerical computation, does data analysis, and drafts the manuscript. Vladimir Alexeev, John Walsh, and Uma Bhatt set the design of the work, give critical ideas and revision comments on data analysis and manuscript writing.

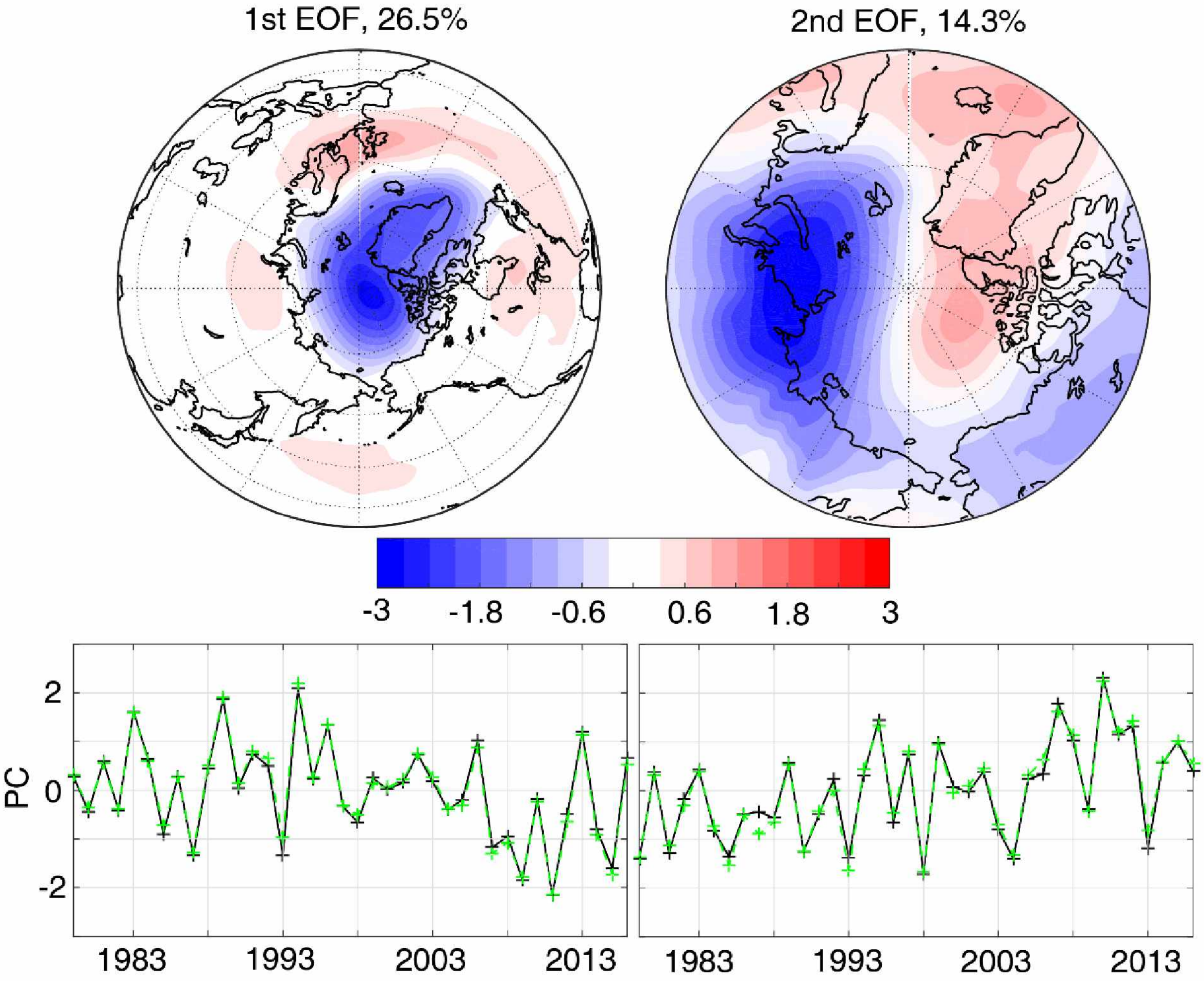

Figure 5.1. The spatial patterns of JJA AO (a) and AD (b) in ERA-interim. The Normalized JJA AO (c) and AD (d) index from both ERA-interim (black lines) and NCEP/NCAR reanalysis data (green lines) in 1979-2016.

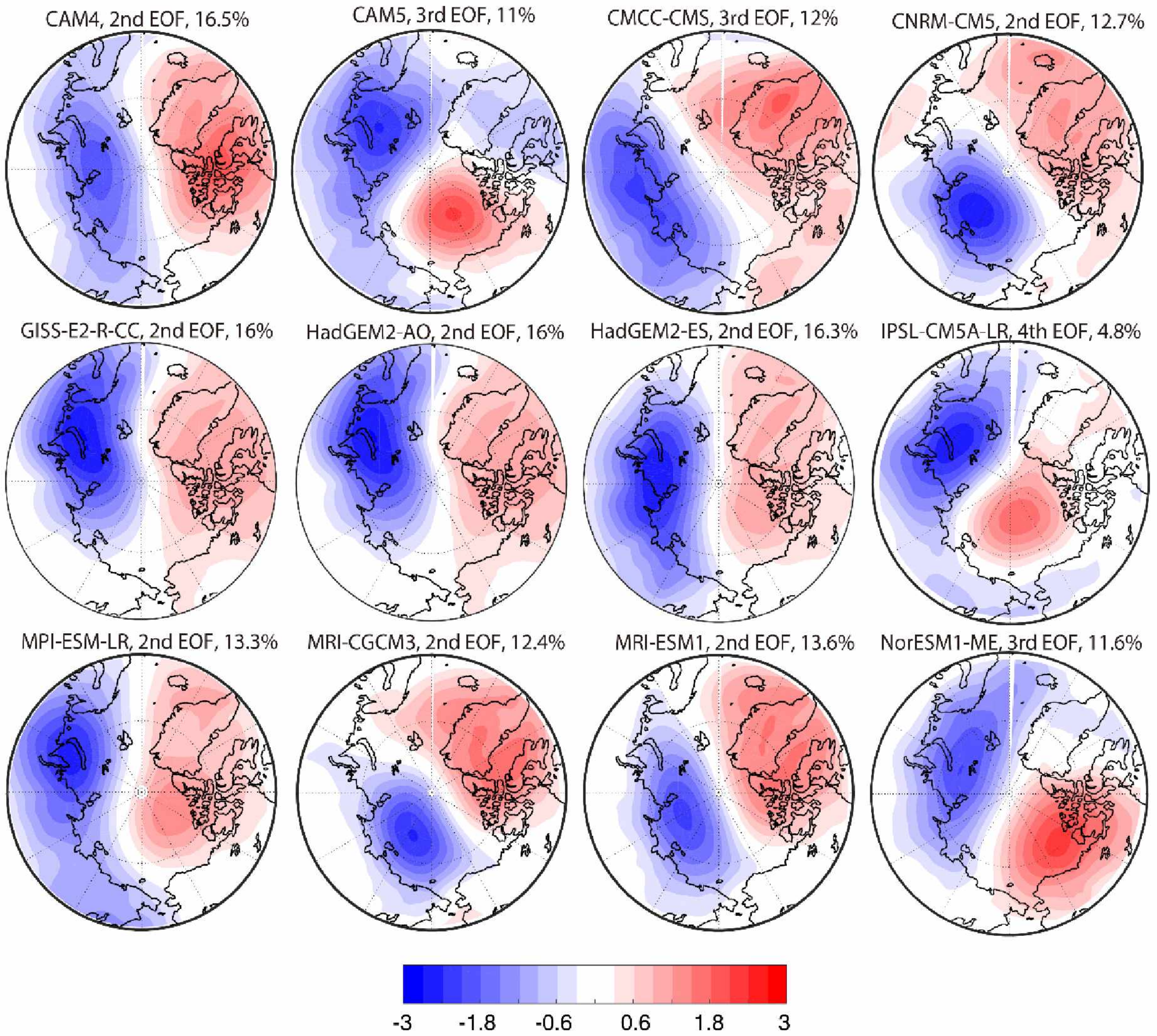

Figure 5.2. The summer AD spatial patterns in the 12 CMIP5 models. All models are somewhat able to reproduce the dipole-shaped distribution of AD, while corresponding modes of EOF and explained variances (list besides the model names above each sub-figure) differ from each other.

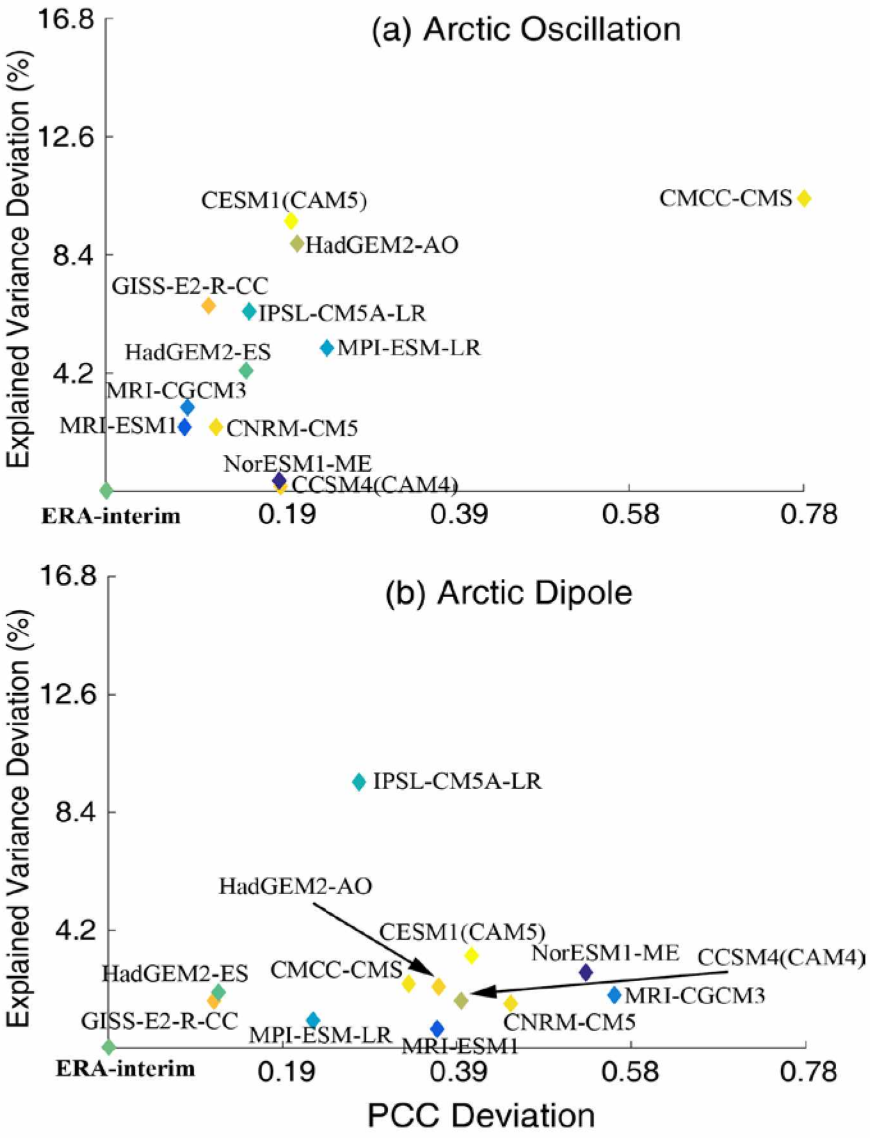

Figure 5.3. The deviations of PCC and explained variance of model-produced summer AO (a) and AD (b) patterns from the reference (ERA-interim). The relative distances from model points to origin points (ERA-interim) represents the performance evaluated by the combined matrix approach.

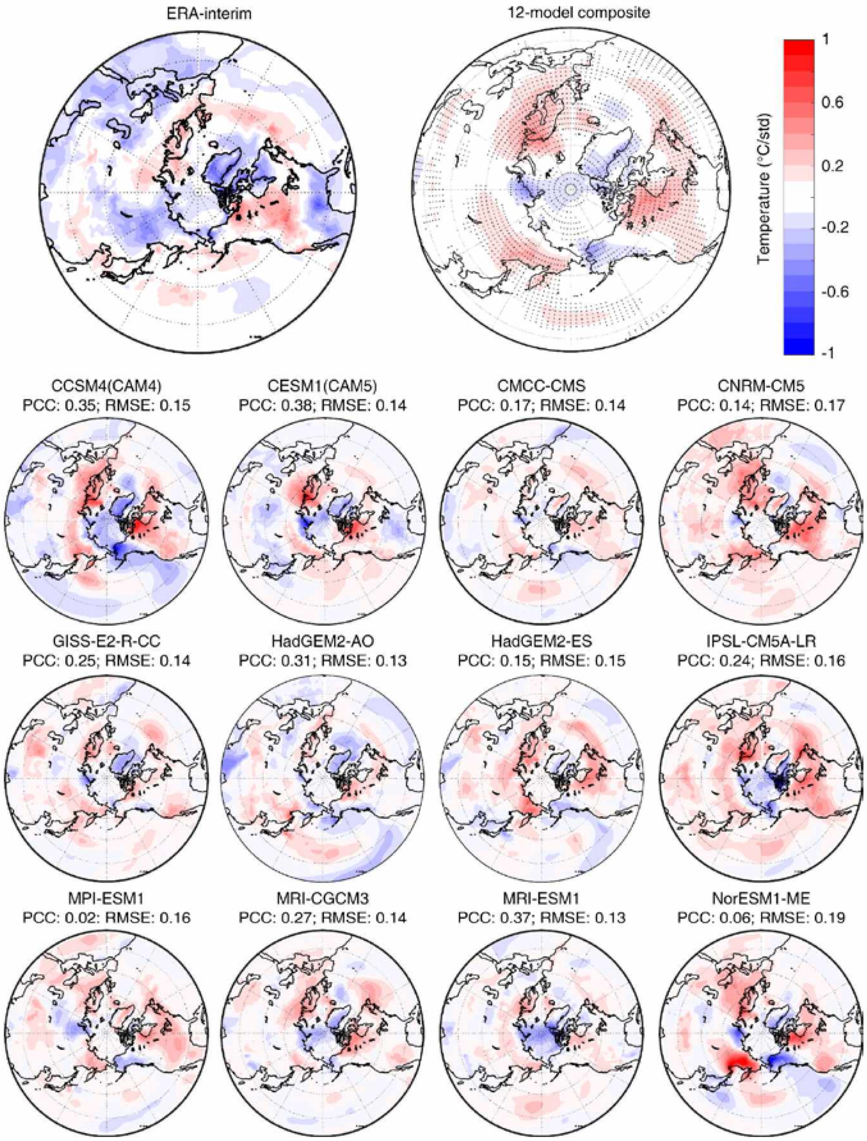

Figure 5.4. The JJA temperature anomalies regressed on AO index (° C) from ERA-interim and 12 CMIP models, as well as the 12-model composite pattern. The PCC and RMSE for each model pattern are listed above each sub-figure. Black dots in the composite pattern indicate the region passes 95% significance level of agreement between models.

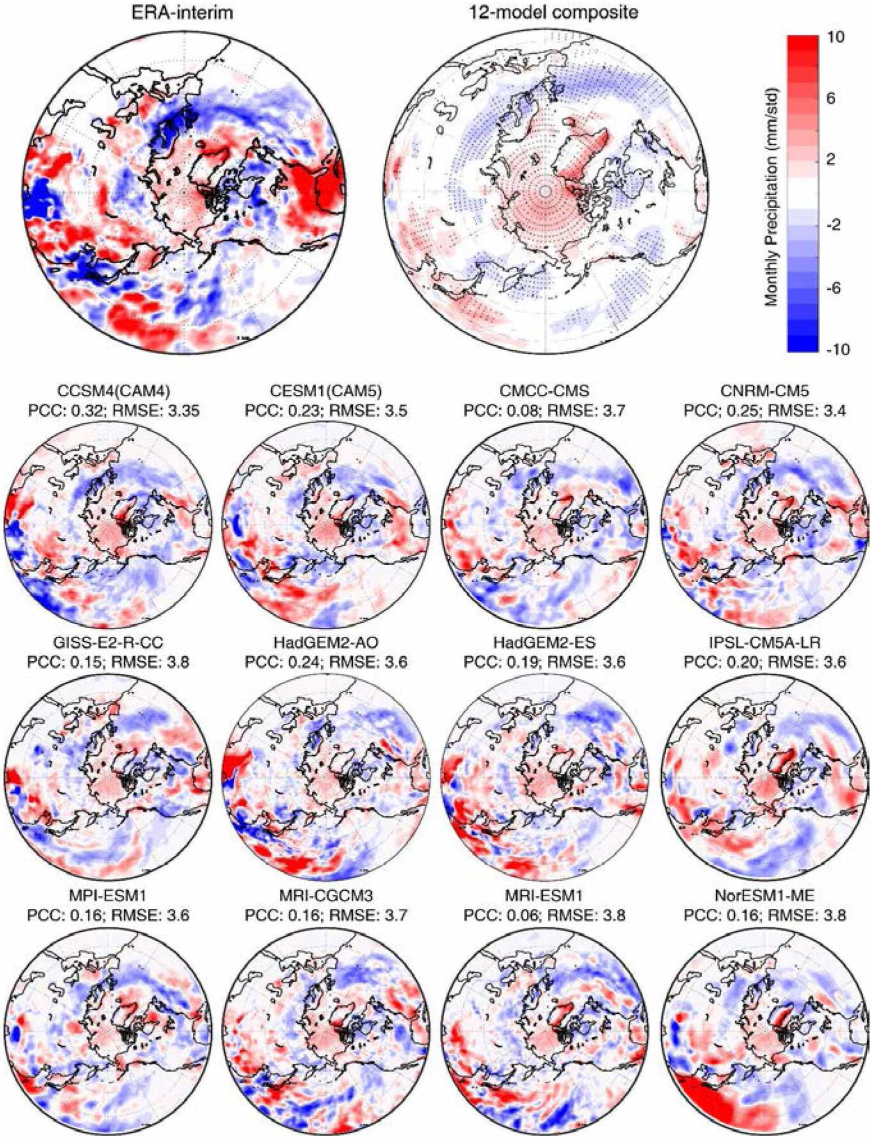

Figure 5.5. Same as Figure 5.4, but for JJA monthly precipitation (mm).

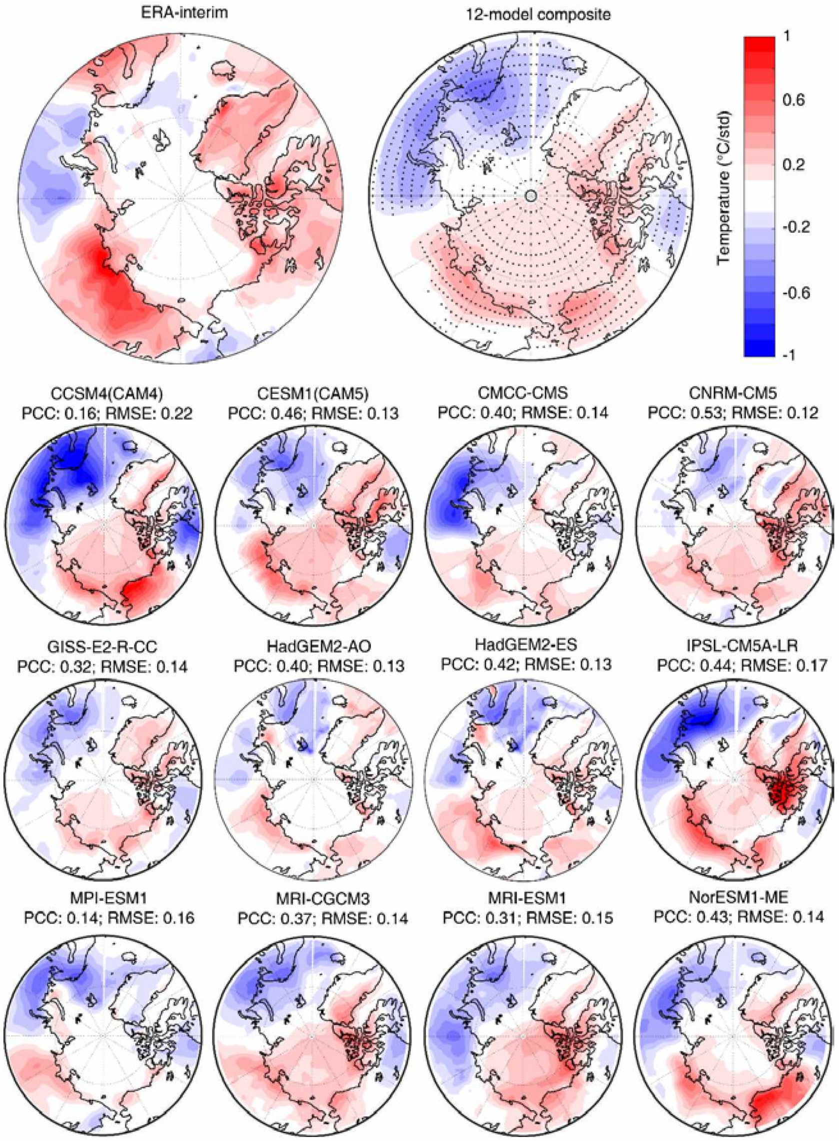

Figure 5.6. The JJA temperature anomalies regressed on AD index (° C) from ERA-interim and 12 CMIP models, as well as the 12-model composite pattern. The PCC and RMSE for each model pattern are listed above each sub-figure. Black dots in the composite pattern indicate the region passes 95% significance level of agreement between models.

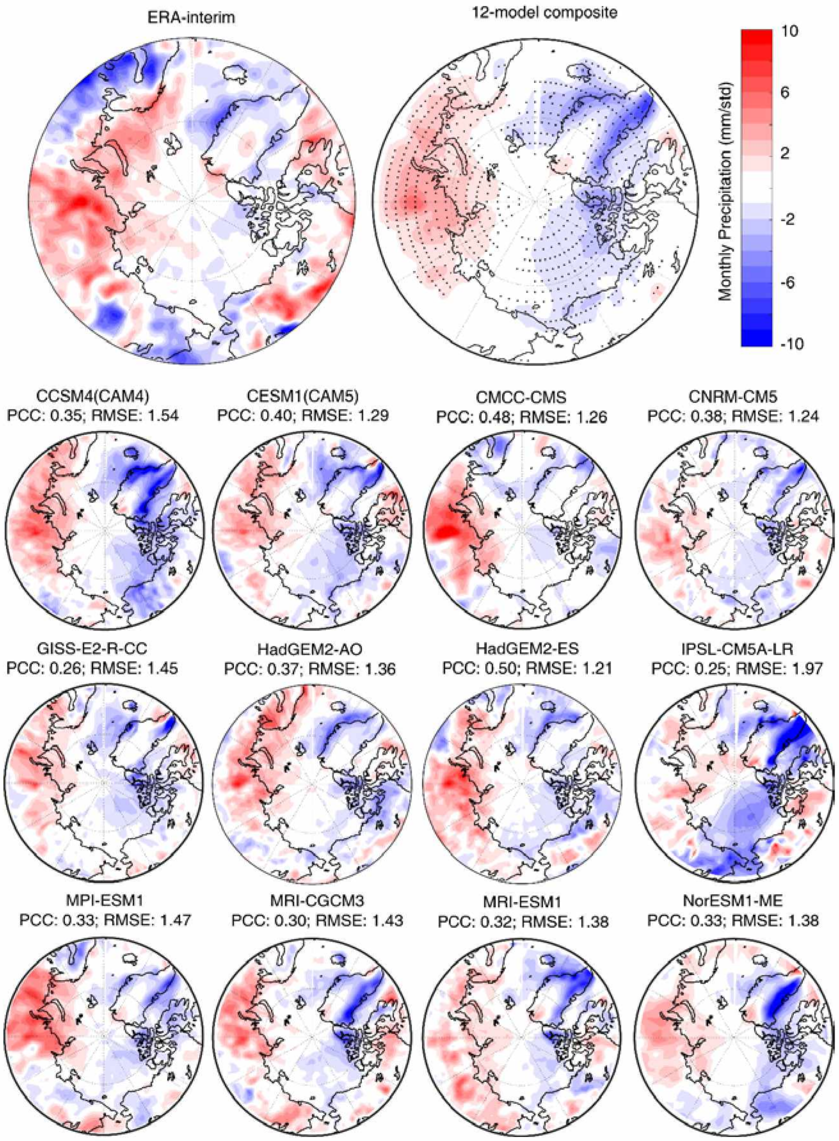

Figure 5.7. Same as Figure 5.6, but for JJA monthly precipitation (mm).

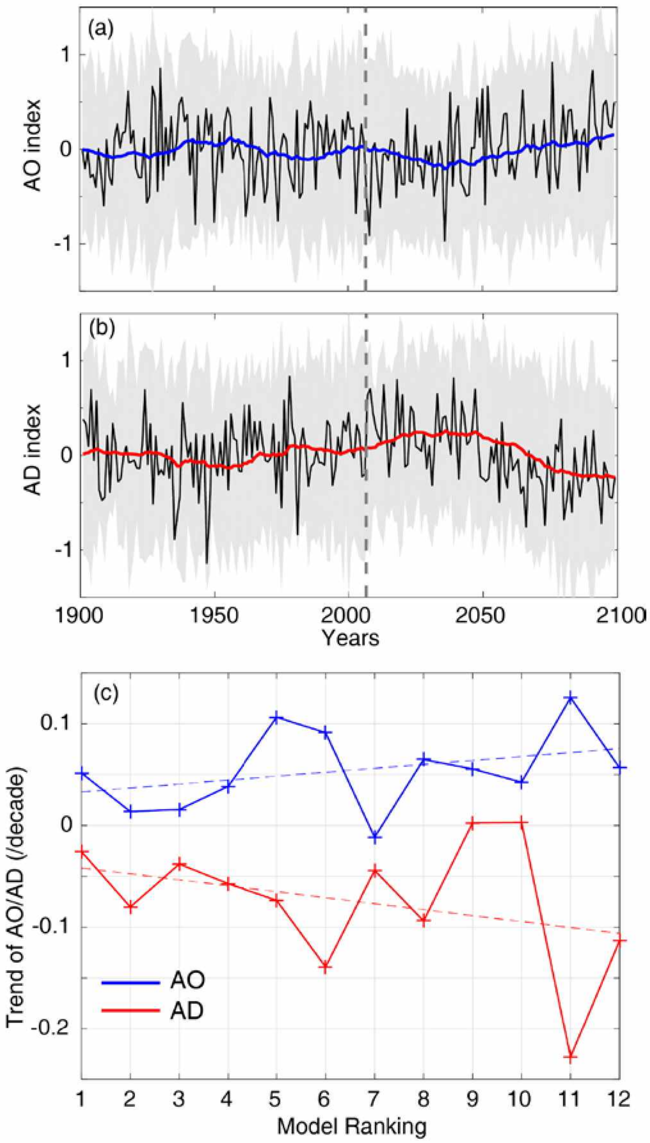

Figure 5.8. The median of AO (a) and AD (b) index from 12 models connecting historical and projected (RCP8.5) period from 1901 to 2099. The grey shaded area delimits one standard deviation of AO/AD index in the 12 models, and the blue/red lines are the 20-year moving average of the median time series. (c) The trend of RCP8.5 AO (blue) and AD (red) as the function of the model ranking by performance in the historical product.

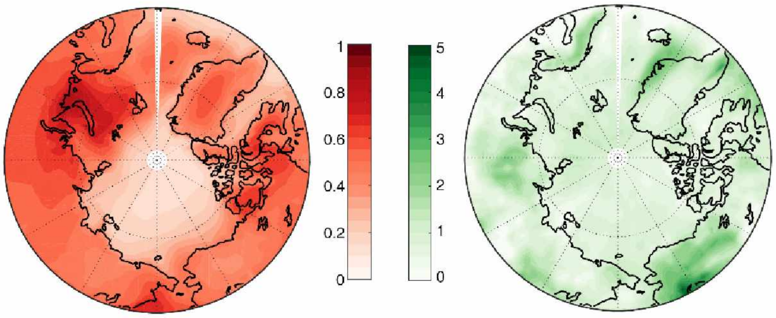
(a) Temperature Trend (°C/decade)

(b) Monthly Precipitation Trend (mm/decade)

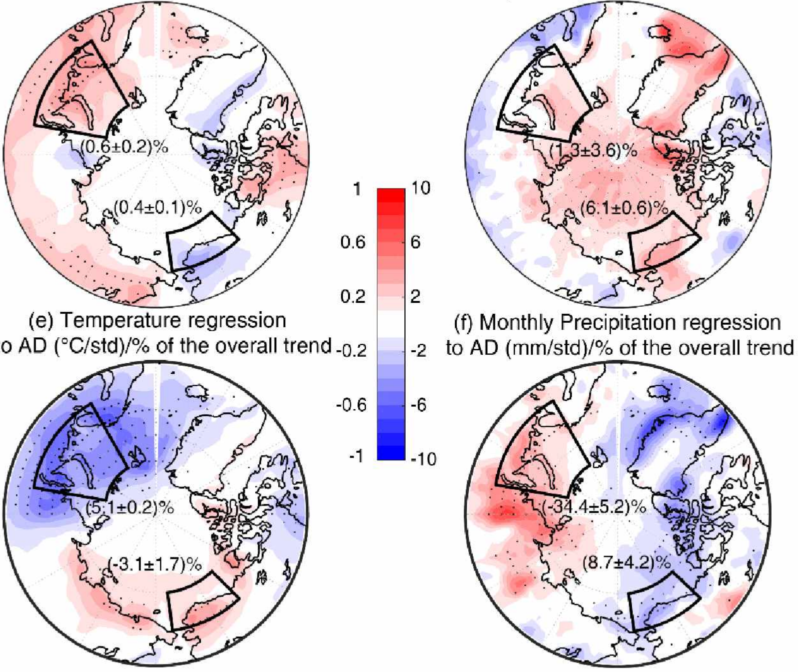
(c) Temperature regression to AO (°C/std)/% of the overall trend

(d) Monthly Precipitation regression to AO (mm/std)/% of the overall trend

(e) Temperature regression to AD (°C/std)/% of the overall trend

(f) Monthly Precipitation regression to AD (mm/std)/% of the overall trend

Figure 5.9. The composite trend of temperature (a) and precipitation (b) in the top 4 models (HadGEM2-ES, GISS_E2-R-CC, MPI-ESM-LR, and MRI-ESM1). The composite of these four models on regressed temperature and precipitation respectively on AO and AD are shown in (c)-(f). Black lines bounded sub-regions to examine the contributions independently from AO and AD on temperature and precipitation trends in the top 4 models.

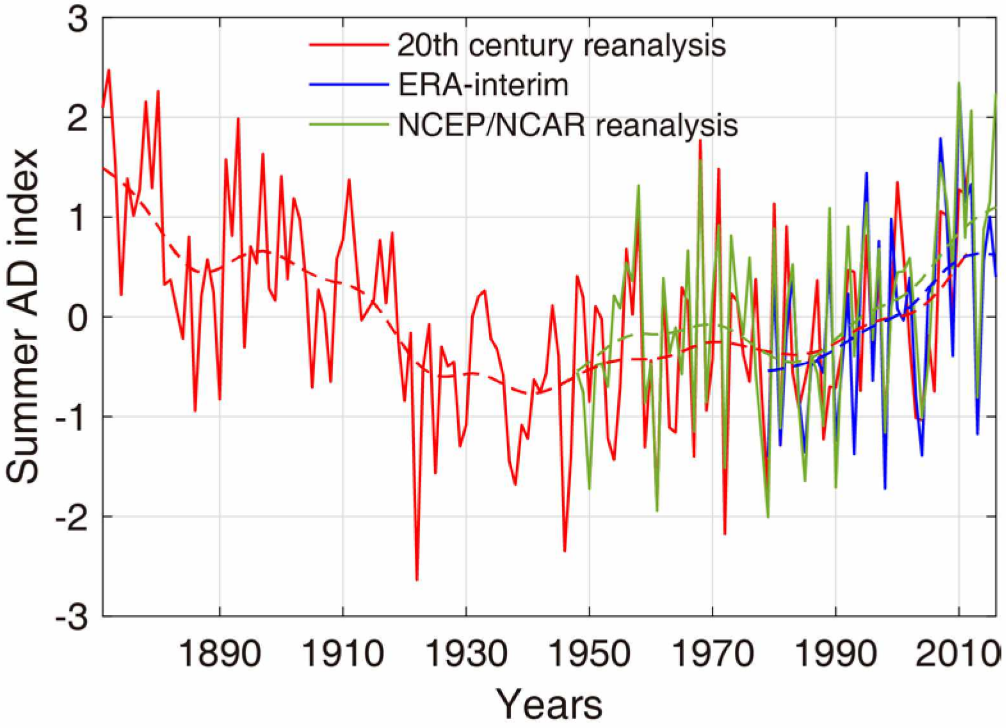

Figure 5.10. The JJA AD index derived from ERA-interim (blue line), NCEP/NCAR reanalysis (green), and 20th-century reanalysis (version2, red line) across their available time periods, which are 1870-2012 for 20th-century reanalysis, 1948-2016 for NCEP/NCAR reanalysis, and 1979-2016 for ERA-interim. 142-year-long data of 20th-century reanalysis data enables it to show the multidecadal variability of summer AD.

(a) ERA-interim cloud fraction (b) ERA-interim sea ice concentration

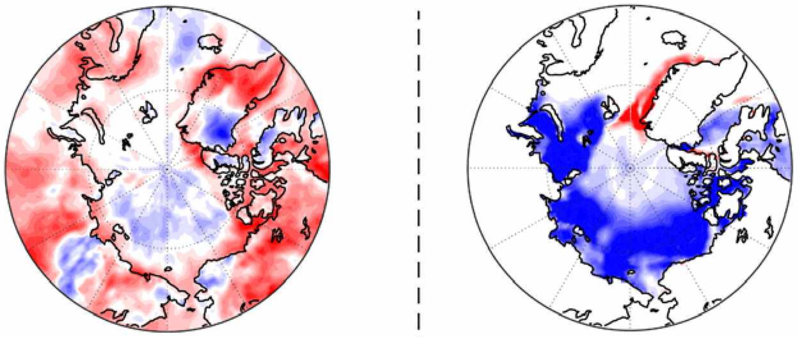

(c) NCEP/NCAR cloud fraction (b) NCEP/NCAR sea ice concentration

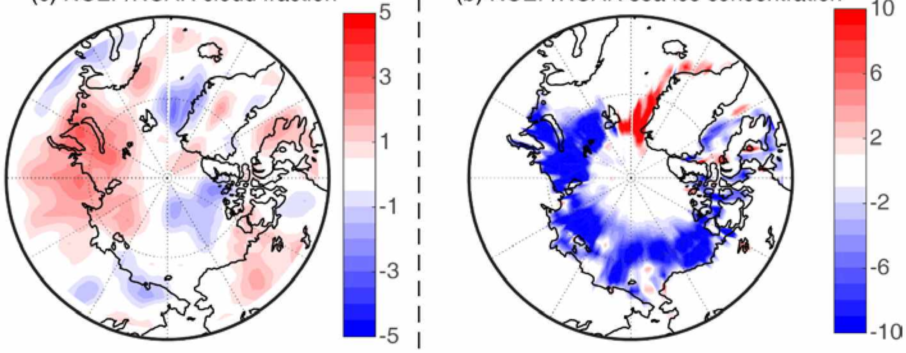

(e) Top 4 CMIP5 cloud fraction (f) Top 4 CMIP5 sea ice concentration

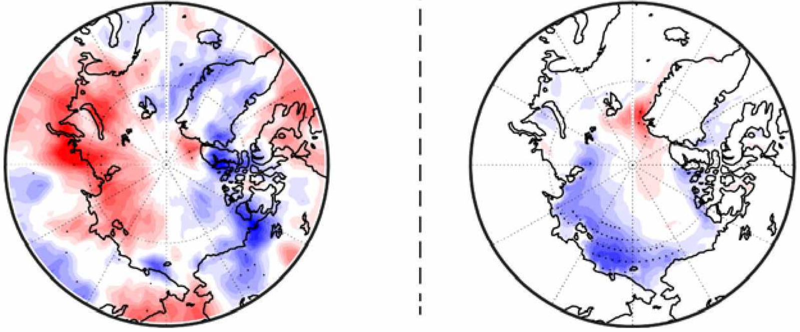

Figure 5.11. The regression maps of total cloud fraction (%) and sea ice concentration (%) respectively from ERA-interim (1979-2016, a and b), NCEP/NCAR reanalysis data (1979-2016, c and d), and the top 4 CMIP5 model composite (2006-2050, e and f).

Table 5.1. The list of chosen CMIP5 models in this study.

	Model	Atmospheric grid (degree×degree)	Institution
1	CCSM4 (CAM4)	1.25×0.9	National Center for Atmospheric Research
2	CESM1 (CAM5)	1.25×0.9	National Science Foundation, Department of Energy, National Center for Atmospheric Research
3	CMCC-CMS	1.875×1.86	Centro Euro-Mediterraneo per I Cambiamenti Climatici
4	CNRM-CM5	1.41×1.40	Centre National de Recherches Meteorologiques, Centre Europeen de Recherche et Formation Avancees en Calcul Scientifique
5	GISS-E2-R-CC	2.5×2.0	NASA Goddard Institute for Space Studies
6 7	HadGM2-AO HadGM2-ES	1.875×1.25	Met Office Hadley Centre
8	IPSL-CM5A-LR	2.5×1.25	Institut Pierre-Simon Laplace
9	MPI-ESM1-LR	1.875×1.86	Max Planck Institute for Meteorology (MPI-M)
10 11	MRI-CGCM3 MRI-ESM1	1.125×1.125	Meteorological Research Institute
12	NorESM1-ME	2.5×1.9	Norwegian Climate Centre

Table 5.2. The list of the explained Variances, PCCs, and the RMSEs of the 12 models on AO and AD, as well as their median values. The overall rank considering both AO and AD performance is listed in the rightmost column.

	AO spatial pattern			AD Spatial Pattern			Rank
	Explained variance	Pattern Correlation	RMSE	Explained variance	Pattern Correlation	RMSE	
CCSM4 (CAM4)	0.267	0.806	0.270	0.165	0.632	0.451	**5**
CESM1 (CAM5)	0.169	0.794	0.276	0.11	0.596	0.476	**8**
CMCC-CMS	0.161	0.225	0.832	0.12	0.666	0.449	**12**
CNRM-CM5	0.242	0.878	0.242	0.127	0.553	0.492	**6**
GISS-E2-R-CC	0.199	0.885	0.215	0.16	0.882	0.265	**2**
HadGEM2-AO	0.177	0.787	0.331	0.16	0.608	0.473	**7**
HadGEM2-ES	0.222	0.844	0.268	0.163	0.877	0.264	**1**
IPSL-CM5A-LR	0.329	0.840	0.285	0.048	0.721	0.386	**11**
MPI-ESM-LR	0.214	0.754	0.356	0.133	0.773	0.364	**3**
MRI-CGCM3	0.295	0.910	0.175	0.124	0.438	0.544	**10**
MRI-ESM1	0.288	0.912	0.174	0.136	0.635	0.445	**4**
NorESM1-ME	0.261	0.807	0.267	0.116	0.469	0.538	**9**
Median	0.232	0.823	0.269	0.130	0.634	0.450	

References

Alexeev, V. A., E. S. Euskirchen, J. E. Cherry, and R. C. Busey, 2015: Tundra burning in 2007–Did sea ice retreat matter? *Polar Science*, **9,** 185-195.

Collins, M., and Coauthors, 2013: Climate change 2013: the physical science basis. Contribution of Working Group I to the Fifth Assessment Report of the Intergovernmental Panel on Climate Change. *Long-term Clim. Chang. Proj. Commitments Irreversibility, Cambridge Univ. Press. Cambridge, UK, New York.*

Compo, G. P., and Coauthors, 2011: The twentieth century reanalysis project. *Quarterly Journal of the Royal Meteorological Society*, **137,** 1-28.

Dee, D. P., and Coauthors, 2011: The ERA-Interim reanalysis: configuration and performance of the data assimilation system. *Quarterly Journal of the Royal Meteorological Society*, **137,** 553-597.

Deser, C., 2000: On the teleconnectivity of the "Arctic Oscillation". *Geophysical Research Letters*, **27,** 779-782.

Gudkovich, Z., 1961: Relation of the ice drift in the Arctic Basin to ice conditions in the Soviet Arctic seas. *Tr. Okeanogr. Kom. Akad. Nauk SSSR*, **11,** 14-21.

Hollingsworth, A., K. Arpe, M. Tiedtke, M. Capaldo, and H. Savijärvi, 1980: The performance of a medium-range forecast model in winter–impact of physical parameterizations. *Monthly Weather Review*, **108,** 1736-1773.

Kay, J. E., and A. Gettelman, 2009: Cloud influence on and response to seasonal Arctic sea ice loss. *Journal of Geophysical Research: Atmospheres*, **114**.

Kay, J. E., T. L'Ecuyer, A. Gettelman, G. Stephens, and C. O'Dell, 2008: The contribution of cloud and radiation anomalies to the 2007 Arctic sea ice extent minimum. *Geophysical Research Letters*, **35**.

Kistler, R., and Coauthors, 2001: The NCEP–NCAR 50–year reanalysis: Monthly means CD–ROM and documentation. *Bulletin of the American Meteorological society*, **82,** 247-267.

Langland, R. H., and R. N. Maue, 2012: Recent Northern Hemisphere mid-latitude medium-range deterministic forecast skill. *Tellus A: Dynamic Meteorology and Oceanography*, **64,** 17531.

Lindsay, R., M. Wensnahan, A. Schweiger, and J. Zhang, 2014: Evaluation of seven different atmospheric reanalysis products in the Arctic. *Journal of Climate*, **27,** 2588-2606.

Ogi, M., S. Rysgaard, and D. G. Barber, 2016: Importance of combined winter and summer Arctic Oscillation (AO) on September sea ice extent. *Environmental Research Letters*, **11,** 034019.

Overland, J. E., J. A. Francis, E. Hanna, and M. Wang, 2012: The recent shift in early summer Arctic atmospheric circulation. *Geophysical Research Letters*, **39**.

Phillips, A. S., C. Deser, and J. Fasullo, 2014: A new tool for evaluating modes of variability in climate models. *Eos*, **95,** 453-455.

Rigor, I. G., J. M. Wallace, and R. L. Colony, 2002: Response of sea ice to the Arctic Oscillation. *Journal of Climate*, **15,** 2648-2663.

Skeie, P., 2000: Meridional flow variability over the Nordic seas in the Arctic Oscillation framework. *Geophysical research letters*, **27,** 2569-2572.

Steele, M., J. Zhang, and W. Ermold, 2010: Mechanisms of summertime upper Arctic Ocean warming and the effect on sea ice melt. *Journal of Geophysical Research: Oceans*, **115**.

Stoner, A. M. K., K. Hayhoe, and D. J. Wuebbles, 2009: Assessing general circulation model simulations of atmospheric teleconnection patterns. *Journal of Climate*, **22,** 4348-4372.

Taylor, K. E., R. J. Stouffer, and G. A. Meehl, 2012: An overview of CMIP5 and the experiment design. *Bulletin of the American Meteorological Society*, **93,** 485-498.

Thompson, D. W., and J. M. Wallace, 1998: The Arctic Oscillation signature in the wintertime geopotential height and temperature fields. *Geophysical research letters*, **25,** 1297-1300.

Tremblay, L., 2001: Can we consider the Arctic Oscillation independently from the Barents Oscillation? *Geophysical research letters*, **28,** 4227-4230.

Wang, J., and Coauthors, 2009: Is the Dipole Anomaly a major driver to record lows in Arctic summer sea ice extent? *Geophysical Research Letters*, **36**.

Watanabe, E., J. Wang, A. Sumi, and H. Hasumi, 2006: Arctic dipole anomaly and its contribution to sea ice export from the Arctic Ocean in the 20th century. *Geophysical research letters*, **33**.

Wu, B., J. Wang, and J. E. Walsh, 2006: Dipole anomaly in the winter Arctic atmosphere and its association with sea ice motion. *Journal of Climate*, **19,** 210-225.

Wu, B., R. Zhang, and D. A. Rosanne, 2008: Arctic dipole anomaly and summer rainfall in Northeast China. *Chinese Science Bulletin*, **53,** 2222.

Wu, B., J. E. Overland, and R. D'Arrigo, 2012: Anomalous Arctic surface wind patterns and their impacts on September sea ice minima and trend. *Tellus A*, **64**.

Zhang, J., R. Lindsay, M. Steele, and A. Schweiger, 2008a: What drove the dramatic retreat of arctic sea ice during summer 2007? *Geophysical Research Letters*, **35**.

Zhang, X., A. Sorteberg, J. Zhang, R. Gerdes, and J. C. Comiso, 2008b: Recent radical shifts of atmospheric circulations and rapid changes in Arctic climate system. *Geophysical Research Letters*, **35**.

Chapter 6 Conclusions

6.1 General Discussions

This thesis consists of four studies in terms of the regional climate change on the North Slope of Alaska. These four studies focus on the contributing factors of global warming (radiative forcing), sea ice decline, earlier lake ice-off, and atmospheric circulation changes respectively. All four studies are based on numerical simulations or on model-based datasets. The data sources include in situ observations, reanalysis datasets, global climate model outputs, and dynamical downscaling products.

The dynamical downscaling products project the overall regional climate change on the North Slope of Alaska in the high spatial (10 km) and temporal (3-hourly) resolutions. The regional climate change projected in the downscaling products is the combined result of global radiative forcing, atmospheric circulation changes, and impacts of sea ice decline. The impacts of earlier lake ice-off are not capturable by this downscaling framework, as resolving a substantial amount of Arctic lakes on the North Slope of Alaska require at least one order of magnitude finer grid spacing (e.g. 1 km). Likewise, the projected sea ice decline is imported from CESM as boundary conditions rather than computed by WRF itself. The impacts of sea ice decline in the downscaling products are therefore totally externally-dependent to the CESM sea ice cover.

Chapter 3 and 4 document the studies focused on the impacts of the sea ice decline and the earlier lake ice-off to the North Slope of Alaska. Chapter 3 speculates that sea ice decline impacts both the near-surface atmosphere and permafrost are enhanced in late spring and early summer in the 21st century. The projected magnitude of sea ice decline warmings in late spring and early summer are comparable in magnitude to those from the lake ice-off that is found in this study (0.5-0.7 °C). Such summer sea ice decline impacts emerge in May and June, making a three-month extra warming period if combining with the lake ice-off impacts in July explored in Chapter 4. Even so, the lake ice-off impacts to the Arctic Alaska are much weaker than the sea ice decline impacts. The sea ice decline impacts are the largest in late fall and early winter, which is about 6 times stronger (3-4 °C) than the lake ice-off impacts in this study.

The impacts of the sea ice decline and lake ice-off originate from the same physical mechanism that the warmer water surface releases heat and moisture into the colder atmosphere when the ice cover is removed. The water-air temperature gradients, however, emerge differently between the sea ice decline and lake ice-off. The Sea Surface Temperature (SST) is relatively insensitive to the atmospheric background. The lake surface temperature, on the other hand, has a much smaller inertia to change from the air temperature than the SST has because of the small size and depth of Arctic lakes. Such relationships between the air temperature and the lake surface temperature sets the base of the lake surface temperature adjustment algorithm employed in Chapter 4. Such a difference in generating the water-air temperature gradient results in the different evolutions of the impacts over time in a warmer 21st-century climate. The sea ice decline warming is projected to be weaker during the late fall and early winter while stronger during the late spring and early summer (Figure 3.5). On the other hand, the temperature gradient between the lake surface and the atmosphere will not change substantially in the future even if the lake ice cover keeps to melt earlier (Figure 4.6). The reason being that it is the daily change of air temperature, rather than the value of it, that determines the strength of lake ice-off warming.

All studies agree on the conclusion that the global warming (radiative forcing) is responsible for the majority (>50%) of the regional climate change on the North Slope of Alaska, while the other three factors contributes primarily on modulating the spatial and temporal variabilities of it. Sea ice decline contributes the most among the other three contributing factors on warming the near surface atmosphere. In late fall and early winter, sea ice decline accounts for up to 45% (in December) of the total atmospheric warming, while the percentage drops to less than 10% in summer. The lake ice-off impacts the regional climate on small spatial and temporal scales. The pronounced impacts occur only in late summer, the strength of which is similar to that of the sea ice decline in summer (less than 10% of total warming). The AO and AD result in the spatial unevenness of the regional climate change across the pan-Arctic coast. Their long-term trends in the 21st century jointly lead to a slight cooling (-3%) and wetting (15%) in summer on the North Slope of Alaska. Comparatively, the sea ice decline in late spring and early summer results in a negligible amount of precipitation impact on the North Slope of Alaska. Although the heavy-loaded computation makes it impossible to examine the lake ice-off impact to local precipitation, we imply that the strength of the impact cannot surpass that of sea ice decline considering the area of opened water and the amount of heat and moisture released.

The warming of the near-surface atmosphere and permafrost on the North Slope of Alaska can result in a series of ecological impacts. The Normalized Difference Vegetation Index (NDVI) that represents the vegetation productivity, for example, has been observed to rise in Arctic Alaska since the 1970s (Jia et al., 2003). The temperature increase is getting slower while the precipitation increase is getting faster in summer over the North Slope of Alaska (discussed in Chapter 5) for a favorable environment for vegetation growth, and the stronger warming in winter than in summer (discussed in Chapter 1) extends the growing season (Pearson et al., 2013; Snyder, 2013). Changes of vegetation types are also expected according to the assessment by Pearson et al. (2013). Although the decline of NDVI is observed in the first decade of 21st century accompanied by a decline in warming over the pan-Arctic (Bhatt et al., 2013; Bhatt et al., 2017), we still speculate the increase of vegetation productivity over the North Slope of Alaska in the long term throughout the end of 21st century.

The potential ecological impacts are also brought by the permafrost warming and its consequences. The release of carbon in the form of carbon dioxide (CO_2) and methane (CH_4) from the warmed permafrost can become the source of greenhouse gases in the atmosphere that makes the radiative forcing and global warming stronger (Schuur et al., 2009; Natali et al., 2014). The stronger warming globally then warm the permafrost even more, forming a positive feedback mechanism (Schaefer et al., 2014; Schuur et al., 2015). Such positive feedback may accelerate global warming effect, although a small portion of it may be mediated by the increase of vegetation productivity (Schuur and Abbott, 2011; Jorgenson et al., 2013). Although the carbon release from permafrost is out of the scope of this thesis, the estimation of permafrost warming on the North Slope of Alaska resulted from multiple contributing factors can provide important climatic background to such ecological effect studies of permafrost warming.

6.2 Conclusions

The dynamical downscaling products developed for the North Slope of Alaska offer a high-resolution climatic background for both the historical and the projected periods spanning 1950-2100. Compared to the reanalysis dataset and the GCM output, the dynamical downscaling successfully resolves an enhanced topographical effect of the Brooks Range. The higher amount of precipitation with higher variabilities show the improvement from the under-catchment of precipitation in observation and from the underestimation of seasonal variability in ERA-interim.

The downscaling data products illustrate a warming North Slope of Alaska with more precipitation in the 21st century. Between the radiative forcing scenarios, the RCP4.5 presents the smaller precipitation and temperature increasing trends, while the RCP8.5 presents the larger increasing trends, compared to those in the historical product. The RCP8.5 scenario projects fall (SON) and winter (DJF) precipitation and temperature with higher positive trends than in other two seasons, implying the presence of sea ice decline impacts.

The isolated impacts of sea ice decline on the low atmosphere and the permafrost are explored by conducting the polar WRF sensitivity experiments. The sea ice decline impacts include increased surface air temperature and specific humidity, as well as the enhanced low-level cloud cover and precipitation, which are maximized in late fall and early winter. The permafrost temperature is correspondingly increased by the enhanced downwelling ground heat flux. In terms of the relative contributions to the overall climate change, the sea ice decline is responsible for 45% of the atmospheric warming and 22% of the permafrost warming at most in December. In the 21st century, sea ice decline warming effect is projected to be stronger in late spring and early summer, as the offshore sea ice cover melts so early in late spring that the colder-than-SST air temperature drives substantial turbulent heat fluxes upwelling from the ocean.

Likewise, the earlier ice-off of the Arctic lakes over the North Slope of Alaska also contributes to the surface air temperature and moisture increase over the North Slope of Alaska. But such increases are not substantial except in July in the downwind regions of Arctic lakes. The lake ice-off impacts are strengthened when the air temperature drops. The lake surface temperature decreases with higher inertia than air temperature due to water's highest heat capacity. The substantial lake impacts, therefore, arise from the enlarged water-air temperature gradient. Such a mechanism also restricts the lake ice-off impacts from being stronger in the 21st century, even though the earlier trend of the lake ice-off remains, as a warmer climate does not help to enlarge the water-air temperature gradient.

The projected changes in atmospheric circulation patterns also contribute to the regional climate change over the North Slope of Alaska. Most of the 12 selected models agree on having a positive trend of the AO and a negative trend of the AD in summer in their 21st-century projections (RCP8.5). The top four models according to a combined metric ranking approach to the historical simulation products show more consistency on the magnitudes of both trends compared to the other 8 models do. Such trends of the AO and AD influence the summer regional climate of the North Slope of Alaska by reducing the temperature increase while favoring the precipitation increase in the 21st century. Among these two climatic variabilities, the AD plays a more important role than the AO does in bringing such climatic anomalies, while the global warming continues to be the dominant contributing factor on the regional climate change on the North Slope of Alaska.

In summary, the regional climate on the North Slope of Alaska is changing towards a warmer and wetter state by the end of the 21^{st} century. The global warming (radiative forcing) continues to be the dominant contributing factor in both summer and winter. The other three contributing factors play minor nonetheless important roles in resulting in the spatial and temporal asymmetries of climate change not only over the North Slope of Alaska but also the whole pan-Arctic coastal region. In summer, the atmospheric circulation has the opposite impact (cooling) to the impact of sea ice decline and lake ice-off, and also with smaller absolute value of relative contribution (around -2% for atmospheric circulation change while around 10% for sea ice decline and lake ice-off combined). In winter, the lake ice-off effect disappears, while sea ice decline effect maximizes (up to 45% of relative contribution in December). The relative contribution of atmospheric circulation change in winter is not discussed in this thesis.

6.3 Future work

This thesis discovers that both the positive AD anomaly and the sea ice decline can lead to the reduced cloudiness in summer over the North Slope of Alaska, but for different reasons. The summer AD in its positive phase results in cloudiness reduction by the anticyclonic SLP anomaly over the North Slope of Alaska and the Beaufort Sea region. On the other hand, the sea ice decline in summer reduces the cloudiness by locally destabilizing the low atmosphere and destroying the inversion layer. Given the fact that the positive AD exports sea ice away from the Pacific sector of the Arctic Ocean, leaving larger open water area. It would be interesting to compare the relative contribution of these two factors to the cloudiness reduction. A possible approach to address this research question is conducting regional climate modeling forced by the atmospheric background in the summer of 2007. The summer of 2007 is known to be with both the highly positive AD and a dramatic sea ice retreat (Stroeve et al., 2008; Wang et al., 2009). Observations have also found the abnormal cloudiness reduction offshore the Northern Coast of Alaska (Kay et al., 2008; Schweiger et al., 2008). Sensitivity tests in terms of the sea ice cover and atmospheric circulation background would help to unveil the physical mechanism and the relative contribution to such cloudiness reduction.

The study of the AD impacts and projections focuses only on summer when the AD affect the sea ice export most evidently, while the winter AD impacts are overlooked. By analyzing the reanalysis data, Alexeev et al. (2017) suggested that the winter AD in its negative phase (anti-dipole) also impacts the Arctic sea ice, but with a different mechanism. The anomalous meridional wind by the negative winter AD helps to bring warm air and extra moisture from the North Atlantic to the central Arctic. Implied from a thermodynamic sea ice thickness formula, Alexeev et al. (2017) put forward a mechanism that the correspondingly enhanced downwelling longwave radiation may inhibit the refreezing of sea ice cover and reduces the sea ice thickness, preconditioning the sea ice melt in the following summer. As there has not been any routinely observed sea ice thickness data available for the Arctic Ocean, one alternative verification approach is to explore if the similar mechanism exists in global climate models.

There is a great need to communicate with other scientists on the major findings of this thesis. There have been several studies focused on the North Slope of Alaska using the dynamical downscaling data introduced in Chapter 2. They have also provided many valuable feedbacks and suggestions. The climatic research in this thesis can also serve as the background information to hydrologists, ecologists, and other environmental scientists studying the North Slope of Alaska. More communications are also needed with stakeholders and public communities. The findings of the projected regional climate change will help stakeholders in decision making and the public on a better understanding of the Arctic as a system. Their concerns and interests are also informative for climate scientists conducting studies further.

References

Alexeev, V. A., J. E. Walsh, V. V. Ivanov, V. A. Semenov, and A. V. Smirnov, 2017: Warming in the Nordic Seas, North Atlantic storms and thinning Arctic sea ice. *Environmental Research Letters*, **12**.

Bhatt, U. S., and Coauthors, 2013: Recent declines in warming and vegetation greening trends over pan-Arctic tundra. *Remote Sensing*, **5,** 4229-4254.

Bhatt, U. S., and Coauthors, 2017: Changing seasonality of panarctic tundra vegetation in relationship to climatic variables. *Environmental Research Letters*, **12,** 055003.

Jia, G. J., H. E. Epstein, and D. A. Walker, 2003: Greening of arctic Alaska, 1981–2001. *Geophysical Research Letters*, **30**.

Jorgenson, M. T., and Coauthors, 2013: Reorganization of vegetation, hydrology and soil carbon after permafrost degradation across heterogeneous boreal landscapes. Environmental Research Letters, **8**, 035017.

Kay, J. E., T. L'Ecuyer, A. Gettelman, G. Stephens, and C. O'Dell, 2008: The contribution of cloud and radiation anomalies to the 2007 Arctic sea ice extent minimum. *Geophysical Research Letters*, **35**.

Natali, S. M., E. A. Schuur, E. E. Webb, C. E. H. Pries, and K. G. Crummer, 2014: Permafrost degradation stimulates carbon loss from experimentally warmed tundra. *Ecology*, **95,** 602-608.

Pearson, R. G., S. J. Phillips, M. M. Loranty, P. S. Beck, T. Damoulas, S. J. Knight, and S. J. Goetz, 2013: Shifts in Arctic vegetation and associated feedbacks under climate change. *Nature* Schaefer, K., H. Lantuit, V. Romanovsky, E. , E. Schuur, A. G. , and R. Witt, 2014: The impact of the permafrost carbon feedback on global climate. *Environmental Research Letters*, **9,** 085003.

Schaefer, K., H. Lantuit, V. Romanovsky, E. , E. Schuur, A. G. , and R. Witt, 2014: The impact of the permafrost carbon feedback on global climate. *Environmental Research Letters*, **9,** 085003.

Schuur, E. A., J. G. Vogel, K. G. Crummer, H. Lee, J. O. Sickman, and T. Osterkamp, 2009: The effect of permafrost thaw on old carbon release and net carbon exchange from tundra. *Nature*, **459,** 556.

Schuur, E. A. G., and B. Abbott, 2011: High risk of permafrost thaw. *Nature*, **480,** 32.

Schuur, E. A. G., and Coauthors, 2015: Climate change and the permafrost carbon feedback. *Nature*, **520,** 171.*Climate Change*, **3,** 673.

Schweiger, A., J. Zhang, R. Lindsay, and M. Steele, 2008: Did unusually sunny skies help drive the record sea ice minimum of 2007? *Geophysical Research Letters*, **35**.

Snyder, P. K., 2013: Arctic greening: Concerns over Arctic warming grow. *Nature Climate Change*, **3,** 539.

Stroeve, J., and Coauthors, 2008: Arctic sea ice extent plummets in 2007. *Eos*, **89,** 13.

Wang, J., and Coauthors, 2009: Is the Dipole Anomaly a major driver to record lows in Arctic summer sea ice extent? *Geophysical Research Letters*, **36**.